## Title

Demonstration and Up-scaling of a Calcination-Free Calcium Hydroxide Production Route from Steel Slag by Aqueous Precipitation

**Author**

Vallejo Castano, Sara

**Publication Date**

2021

UNIVERSITY OF CALIFORNIA

Los Angeles

# Demonstration and Up-scaling of a Calcination-Free Calcium Hydroxide Production Route from Steel Slag by Aqueous Precipitation.

A dissertation submitted in partial satisfaction
of the requirements for the degree
Doctor of Philosophy in Mechanical Engineering

by

Sara Vallejo Castaño

2021

# ABSTRACT OF THE DISSERTATION

# Demonstration and Up-scaling of a Calcination-Free Calcium Hydroxide Production Route from Steel Slag by Aqueous Precipitation.

by

Sara Vallejo Castaño

Doctor of Philosophy in Mechanical Engineering

University of California, Los Angeles, 2021

Professor Laurent G. Pilon, Co-Chair

Professor Gaurav N. Sant, Co-Chair

Calcium hydroxide ($Ca(OH)_2$) is a commodity chemical that finds use in diverse industries ranging from food to environmental remediation and construction. The commercial production of $Ca(OH)_2$ by limestone calcination is an energy intensive and $CO_2$ emitting process. Nevertheless, on account of its high specific $CO_2$ uptake (0.59 g per g of $Ca(OH)_2$), $Ca(OH)_2$ could be a "$CO_2$-negative" material if produced in a manner that obviates the need for the thermal decomposition of limestone. This dissertation aims to demonstrate and evaluate the feasibility of upscaling a novel aqueous-phase calcination-free process to recover $Ca(OH)_2$ from industrial alkaline waste based on a three-step process comprised of: (i) calcium leaching from steel slag, (ii) leachate concentration by reverse osmosis (RO), and (iii) $Ca(OH)_2$ precipitation from the concentrated solution through heating. The proof-of-concept was demonstrated on the laboratory scale by individually testing each step. Slag leaching, and reverse osmosis (RO) concentration were evaluated with bench-scale batch experiments. The results demonstrated that alkaline, Ca-containing solutions can be derived from leaching slag with DI water, and that RO could concentrate these solutions by a factor of 2 or higher. However, membrane scaling was evidenced when operating close to the saturation point of $Ca(OH)_2$. Following concentration, $Ca(OH)_2$ was precipitated by forcing a temperature excursion in excess of 65°C while harnessing the retrograde solubility of $Ca(OH)_2$.

Thereafter, a continuous, low-temperature (< 95°C), aqueous-phase pilot-process to produce $Ca(OH)_2$ was designed and assembled. The quantification of the mass and energy balances revealed that increasing the calcium concentration of the feed solution and the precipitation temperature, decrease the energy demands of the RO step. The pilot system operated continuously for 24 hours and achieved a production rate of nearly 1 kg per day of $Ca(OH)_2$ with a purity greater than 95 wt.%. The particle size of the precipitates depended on the residence time in the precipitation reactor, suggesting an ability to produce size-controlled particulates. Importantly, the process achieved full water recirculation, indicative of a low consumable water demand.

Finally, the up-scale feasibility of the process was evaluated by means of an economic, $CO_2$ footprint and geospatial distribution analysis considering the location and availability of slag, electricity, and waste heat sources. The study revealed that the Mid-West, Mid-Atlantic, and South-East regions of the U.S are potential areas to upscale the technology due to the proximity between feedstocks and waste heat sources. The economic analysis showed that RO's electricity and membrane replacement requirements were the largest drivers of the operating cost. Finally, the $CO_2$ footprint of the process could be 40% to 80% lower than the benchmark product if the electricity was sourced from natural gas and wind power, respectively. This is significant as $Ca(OH)_2$ produced in this manner can uptake more $CO_2$ than it associated with its own production, *i.e.*, a $CO_2$-negative material.

The dissertation of Sara Vallejo Castano is approved.

Eric M.V. Hoek

Panagiotis D. Christofides

Gaurav N. Sant, Committee Co-Chair

Laurent G. Pilon, Committee Co-Chair.

TABLE OF CONTENTS

# LIST OF SYMBOLS

| | |
|---|---|
| $A_m$ | Membrane area ($m^2$) |
| $[Ca]$ | Calcium concentration ($mol/m^3$) |
| $c_p$ | Heat capacity of water (J/(kg·K)) |
| $d$ | Slag particle size (μm) |
| $D_I$ | Impeller diameter (m) |
| $GSA$ | Geometric surface area ($cm^2/g$) |
| $L_p$ | Membrane permeability ($m^3/(s\cdot m^2\cdot Pa)$) |
| $\dot{m}$ | mass flow rate (kg/s) |
| $m$ | Mass (kg) |
| $n$ | Moles (mol) |
| $\dot{n}_{Ca}$ | Calcium leaching rate from slag (mmoles Ca/h) |
| $M$ | Molar mass (g/mol) |
| $N_p$ | Mixing power number |
| $P$ | Pressure (Pa) |
| $\Delta P_{mem}$ | Transmembrane pressure difference (Pa) |
| $q$ | specific thermal energy (kWh/kg $Ca(OH)_2$) |
| $\dot{Q}$ | Thermal power (kW) |
| $Q_{fuel}$ | Thermal power plant's fuel heat input |
| $Q_{waste}$ | Thermal power plant's waste heat generation |
| $[OH^-]$ | Hydroxyl ion concentration ($mol/m^3$) |
| $R$ | Rejection coefficient |
| $R_U$ | Universal gas constant (J/(mol·K)) |
| $SA_i$ | Particle surface area ($cm^2$) |
| $t$ | Time (s) |
| $T$ | Temperature (K or °C) |
| $V_i$ | Particle volume ($cm^3$) |

| | |
|---|---|
| $\dot{V}$ | Volumetric flow rate (L/h or $m^3$/s) |
| $V$ | Solution volume |
| $w$ | Specific energy consumption (kWh/kg) |
| $W$ | Energy consumption (kWh) |
| $\dot{W}$ | Power consumption (kW) |
| $W_b$ | Bond work index |
| $W_{elec}$ | Thermal power plant's annual electricity generation |
| $X_{Ca}$ | Calcium extraction from slag |
| $Y$ | RO water reocvery |

**Greek Symbols**

| | |
|---|---|
| $\varphi_i$ | differential volume fraction |
| $\eta_p$ | Pump hydraulic efficiency |
| $\eta_{turbine}$ | Turbine efficiency |
| $\eta_{conv}$ | Thermal to electrical conversion efficiency |
| $\Delta\pi$ | Osmotic pressure difference (Pa) |
| $\Delta\lambda$ | Longitude difference |
| $\Delta\varphi$ | Latitude difference |
| $\rho$ | Density of water (kg/$m^3$) |
| $\omega$ | Rotation frequency ($s^{-1}$) |

**Subscription**

| | |
|---|---|
| *Cool* | Cooling |
| $C_{in}$ | Inlet cooling stream |
| $C_{out}$ | Outlet cooling stream |
| *Ca* | Calcium |
| $Ca(OH)_2$ | Calcium hydroxide |
| *CR* | Cold retentate stream |
| *CS* | Cold saturate stream |

| | |
|---|---|
| *e* | Experimental |
| *F* | Feed stream |
| *g* | Grinding |
| *heat* | heating |
| *HR* | Hot retentate |
| *HS* | Hot saturate |
| *L* | Leachate stream |
| *m* | Mixing |
| *M* | Mix stream |
| *P* | Precipitation, Permeate stream |
| *R* | Retentate stream |
| *S* | Saturate stream |
| *sln* | solution |
| *slag* | Slag |

# LIST OF FIGURES

## LIST OF TABLES

# ACKNOWLEDGEMENTS

I would like to thank my advisors, Professor Laurent Pilon, and Professor Gaurav Sant, for their guidance and commitment to my professional development throughout the duration of my doctoral work. Their honesty and wisdom sparked in me a profound growth experience. Moreover, I would like to thank Professor Eric Hoek and Professor Panagiotis Christofides for serving on my dissertation committee. Furthermore, I would like to express my appreciation to my mentor Dr. Erika Callagon La Plante for the hours of fruitful discussions that always strived to improve the quality of my work, and to Dr. Zongsu Wei for his crucial support with my experimental work.

I would like to express my gratitude to all the former and current members of the Morrin-Martinelli-Gier Memorial Heat Transfer Laboratory and of the Laboratory for the Chemistry of Construction Materials for their camaraderie and support with experimental work. I would also like to acknowledge my classmates for their support during the preparation of the written qualifying examinations. I want to thank all the administrative and staff personnel at UCLA whose work was essential to carry out my research activities. Finally, I would like to thank my parents Alvaro Vallejo and Adriana Castaño, my brothers David Vallejo and Santiago Vallejo, and my partner Sebastian Sanchez who were there unconditionally during the most difficult times and never hesitated to support and encourage me.

This dissertation contains modified versions of manuscripts that have been published in journal articles, have been submitted to journals, or are currently in preparation for publication. All research was conducted in the Morrin-Martinelli-Gier Memorial Heat Transfer Laboratory, the Laboratory for Chemistry of Construction Materials, the Molecular Instrumentation Center, and the Molecular and Nano Archaeology Laboratory at UCLA. As such, I gratefully acknowledge the support that has made these laboratories and their operations possible. The financial support for this research came from the Department of Energy via: (a) The Office of Fossil Energy's National Energy Technology Laboratory (NETL: DE- FE0029825), (b) The Advanced Research Projects Agency-Energy (ARPA-e: DE-AR-0001147), (c) TRANSCEND: a UCLA-NIST Consortium that is supported by its Industry and Agency partners, and (d) The National Science Foundation NRT-INFEWS: Integrated Urban Solutions for Food, Energy, and Water Management (Grant No. DGE-1735325). The contents of this dissertation reflect the views and opinions of the author, who is responsible for the accuracy of the datasets presented herein, and do not reflect the views and/or polices of the agency, nor do the contents constitute a specification, standard or regulation.

Chapter two is a version of [S. Vallejo Castaño, E. Callagon La Plante, S. Shimoda, B. Wang, N. Neithalath, G. Sant, L. Pilon, Calcination-free production of calcium hydroxide at sub-boiling temperatures, RSC Advances., 2021, 11, 1762–1772. https://doi.org/10.1039/D0RA08449B]. S. Vallejo Castaño performed experiments, analysis, and prepared the manuscript. S. Shimoda performed precipitation experiments. E. Callagon La Plante advised the leaching experimental methodology. B. Wang, N. Neithalath, G. Sant, and L. Pilon provided insightful analysis and assisted in revising the manuscript.

Chapter three is a version of a manuscript in preparation for publication [S. Vallejo Castaño, E. Callagon La Plante, M. Collin, G. Sant, L. Pilon, A pilot-process for calcium hydroxide production from iron slag by low-temperature precipitation. Chemical Engineering Journal. 2022, In preparation for publication]. S. Vallejo Castaño performed developed the model and performed the experiments, analyzed the data, and wrote the manuscript. M. Collin performed XRD analysis of slag samples. All authors contributed to data analysis and manuscript revisions.

Chapter 4 is a version of a manuscript in preparation for publication [S. Vallejo Castaño, E. Callagon La Plante, L. Pilon, G. Sant, Upscale potential analysis of calcium hydroxide production from iron slag and waste heat. Journal of Cleaner Production. 2022. In preparation for publication] S. Vallejo Castaño developed the model and performed the simulations. All authors contributed to data analysis and manuscript revisions.

# VITA

| | |
|---|---|
| 2008 – 2013 | B.Sc. Chemical Engineering, Universidad Nacional de Colombia, Medellin |
| 2014 – 2017 | M.Sc. Chemical Engineering, Universidad Nacional de Colombia, Medellin |
| 2017 – 2021 | Graduate student researcher, University of California, Los Angeles |

# PUBLICATIONS

**S. Vallejo Castaño**, E. Callagon La Plante, S. Shimoda, B. Wang, N. Neithalath, G. Sant and L. Pilon, Calcination-free production of calcium hydroxide at sub-boiling temperatures, *RSC Advances*, 11, 1762–1772 (2021)

M. Roldan-Carvajal, **S. Vallejo-Castaño**, O. Álvarez-Silva, S. Bernal-García, S. Arango-Aramburo, C. I. Sánchez-Sáenz and A. F. Osorio, Salinity gradient power by reverse electrodialysis: A multidisciplinary assessment in the Colombian context, *Desalination*, 503, 114933 (2021)

**S. Vallejo-Castaño** and C. I. Sánchez-Sáenz, Design and optimization of a reverse electrodialysis stack for energy generation through salinity gradients, *DYNA*, 84, 84–91 (2017)

# PATENTS

Sant, G. N., Pilon, L. G., Callagon La Plante, E. B., Wang, B., Wei, Z., & **Vallejo Castaño**, **S.** Facile, low-energy routes for the production of hydrated calcium and magnesium salts from alkaline industrial wastes. United States Patent No. US20210024364A1 (2021).

Sant, G., Chen, X., Arnold, R. A., Simonetti, D. A., **Vallejo Castaño, S.**, Prentice, D. P., Jassby, D., Ma, Shengcun. Electrochemical $Ca(OH)_2$ and/or $Mg(OH)_2$ production from industrial wastes and Ca/Mg-containing rocks. U.S. Provisional Application No.: 63/271,059 (2021)

## CONFERENCE PRESENTATIONS

**S. Vallejo Castaño**, E. Callagon La Plante, S. Shimoda, G. Sant and L. Pilon, Calcination-free production of calcium hydroxide at sub-boiling temperature. Presentation delivered at the virtual AIChE Annual meeting, November 2020.

**S. Vallejo Castaño**, C.I. Sanchez Saenz, A. Osorio, Energy generation from salinity gradients between river and sea water through reverse electrodialysis and capacitive reverse electrodialysis. Presentation delivered at the XVI Latin American congress of ocean sciences – COLACMAR, Colombia, October 2015.

**S. Vallejo Castaño**, C.I. Sanchez Saenz, Approximation to the design of a salinity gradient energy generator through reverse electrodialysis. Conference paper and presentation delivered at PROCESA, Colombia, April 2015.

# CHAPTER 1

# Introduction

## 1.1. Calcium natural occurrence and cycling

Calcium (Ca) – the elemental quintessence of $Ca(OH)_2$ – is the fifth most abundant element on earth. It features a relative abundance of 4.15% on the lithosphere and of 0.04% on the sea.[1] Calcium is a critical biological nutrient, and the dominant mineral sink for carbon in the ocean (as $CaCO_3$). Figure 1.1 illustrates the global calcium cycle. The main calcium reservoirs are carbonate and silicate rocks, soils, and terrestrial and aquatic creatures.[2,3] Whereas the major calcium exchange processes are biological uptake, release, and degradation; soil/rock weathering and leaching, and precipitation/sedimentation.[4]

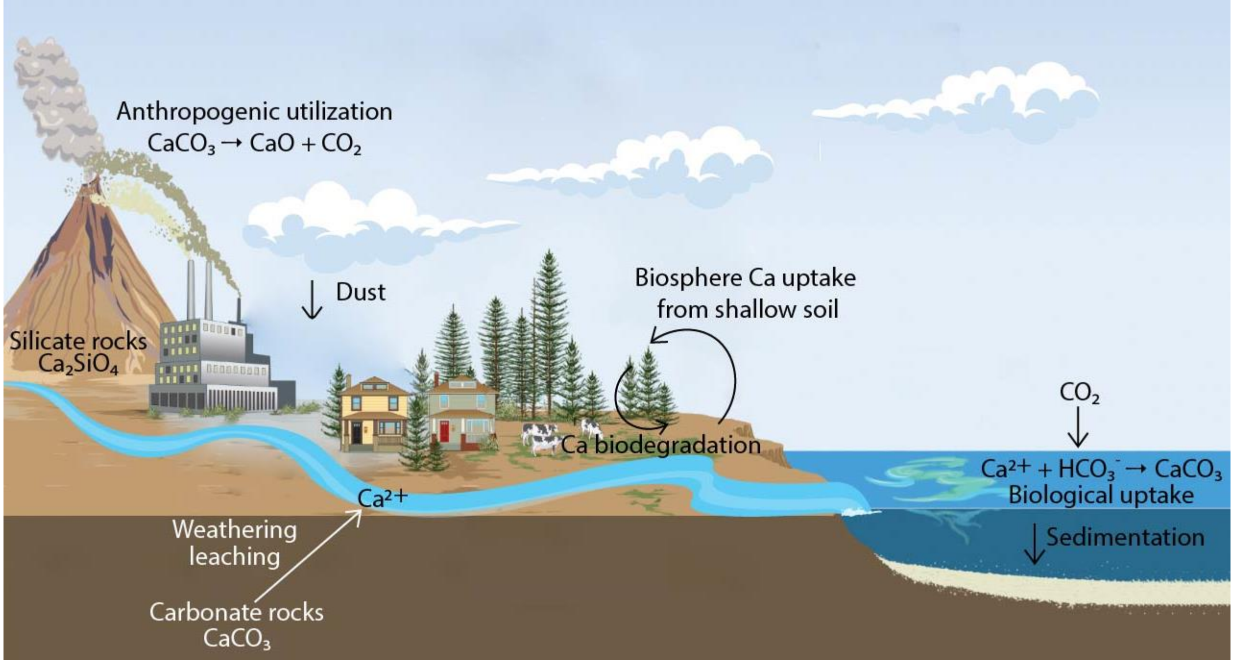

Figure 1.1. Calcium biogeochemical cycle. Taken and modified from 5

Calcium is an essential constituent of rock-forming minerals and it occurs abundantly associated with carbonates (limestone), silicates (wollastonite, feldspars), sulphates (gypsum), among others.[5,6] Igneous or magmatic rocks – comprising 95% of earth's crust – contain on average 4.8% of calcium, whereas sedimentary rocks – comprising the remaining 5% of earth's crust – display calcium oxide contents ranging from 3 to 11% (shale), 5 to 50 % (sandstone), and 42 to 57 % (limestone).[6] The majority of these sedimentary rocks are an important $CO_2$ sink since they have formed throughout most of geological history by the sedimentation of marine organisms such as corals, oysters, and other sea creatures that used the calcium and bicarbonate ions present in seawater to make their underlaying structures and protective shells.

### 1.2. Limestone utilization and environmental concerns

In 2020, the US produced ~ 1 billion ton of crushed limestone (70% of the total crushed stone production).[7] Typical concerns about limestone mining include dust, noise, blasting vibration, and traffic associated with quarry operations. Additionally, limestone quarries may disrupt ecosystems, and cause biodiversity destruction.[8–10] Some limestones act as rock units that can yield water to wells, i.e., aquifers. Where limestone is an aquifer, contaminants from the quarrying operations can escape to the groundwater.[11]

Most of the limestone is used as aggregate in the construction industry, but a portion of it is used as a raw material for a large variety of applications. Two of the most important products made from limestone are "ordinary Portland cement" (OPC) and lime [$CaO$ and $Ca(OH)_2$]. According to the U.S. Geological Survey (USGS), 4.1 billion tons of cement and 420 million tons of lime were produced in the world in 2020. On that year, the U.S. was the third largest producer of cement (86 million tons) and the second largest producer of lime (16 million tons).[12,13]

The production of lime ($CaO$) and OPC, based around the age-old process of limestone calcination, is energy intensive and a major emitter of $CO_2$.[14,15] The thermal decomposition of limestone

($CaCO_3 \rightarrow CaO + CO_2$) at ~ 900 °C generates 0.77 tons of $CO_2$ per ton of CaO.[16] Adding the emissions from fossil fuels required to operate kilns, the total emissions to produce 1 ton of CaO or OPC range from 0.8 to 1.1 tons of $CO_2$.[16–18] The main difference between CaO and OPC production is that lime kilns can operate at 900 °C, whereas cement kilns must operate at 1400 °C to drive further phase change transformations between the CaO and other clay minerals.[19] The widespread utilization of OPC is responsible for 7% of the total anthropogenic $CO_2$ emissions, a major contribution to climate change.[20]

### 1.3. Hydrated lime utilization and opportunities

Calcium hydroxide ($Ca(OH)_2$), also known as portlandite, slaked- or hydrated-lime is produced from the combination of quick lime with water ($CaO + H_2O \rightarrow Ca(OH)_2$). Hence, similar to CaO, its production entails ~ 0.86 ton $CO_2$/ton of $Ca(OH)_2$ from limestone calcination and fossil fuel utilization.[16]

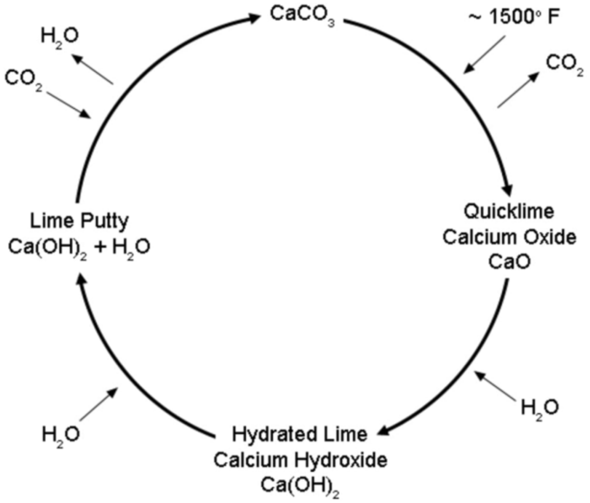

Figure 1.2. The lime cycle

Figure 1.2 shows the traditional conversion cycle from $CaCO_3$ to $Ca(OH)_2$. Figure 1.2 also indicates that $Ca(OH)_2$ tends to carbonate naturally from atmospheric $CO_2$ in the presence of water.[21] Hence, $Ca(OH)_2$ is of great importance in the current climate change context because 1 ton of this material can uptake 0.59 tons of $CO_2$ to form calcium carbonate ($CaCO_3$), a stable carbonate molecule which can permanently store carbon dioxide.[22–25] Any process that emits less than 0.59 t of $CO_2$ over the course of $Ca(OH)_2$ production has the potential to achieve a "carbon-negative" outcome. This is significant as the ability to utilize $Ca(OH)_2$ as a cementation agent,[26] or indeed as a feedstock for CaO could greatly diminish the $CO_2$ emissions associated with traditional cement OPC production.

The use of hydrated lime as a construction material dates back to 6,000 years when it was used by the Egyptians for plastering the pyramids,[27] and it is generally considered a greener construction material compared to OPC due to the lower operating temperature requirements of lime kilns.[16,19,28] Recently, hydrated lime has been an essential component of alternative concrete formulations that can capture and store $CO_2$ using diluted waste streams such as flue gas from thermal power plants.[24,26,29]

Besides construction applications, hydrated lime is used extensively across industries. Figure 1.3. shows that lime is employed in paper, sugar, and glass production;[30] water treatment,[31,32] soil pH regulation,[14,33] among others.[15] Besides, lime has been studied as a regenerative agent for $CO_2$ capture,[34] and more recent studies have suggested the reversible reaction between CaO and $Ca(OH)_2$ as promising thermochemical energy storage alternative in solar thermal power applications.[35,36]

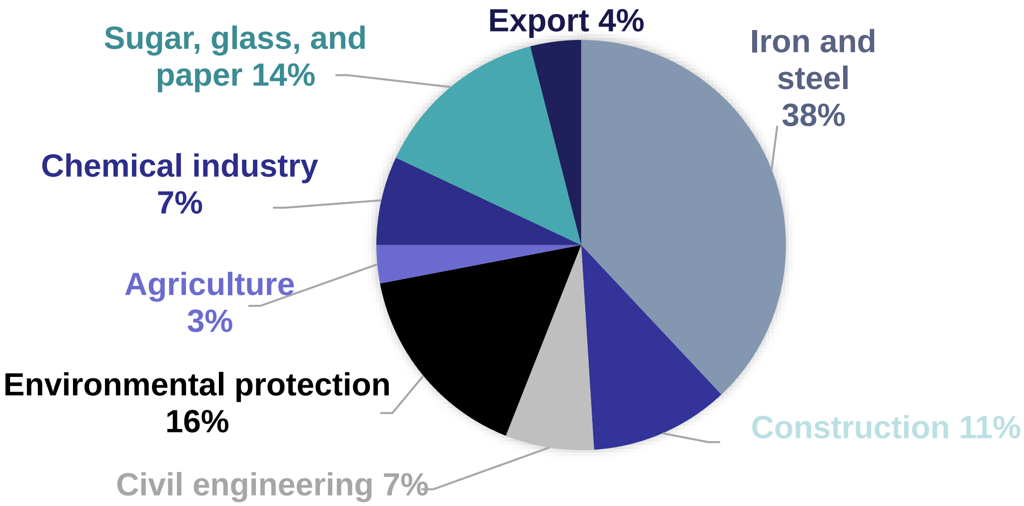

Figure 1.3. Overview of customer market and functionality of lime products. Taken from [37]

## 1.4. Lime and steelmaking

Figure 1.3 shows that 38% of total lime production is used in the steel industry to remove impurities from iron ores.[37] The utilization of lime in electric arc and basic oxygen steelmaking furnaces results in an alkaline byproduct called slag.[38–41] Although some types of slag find use as supplementary cementitious material,[29] other types – such as basic oxygen furnace (BOF) slag – are landfilled because they do not comply with construction industry standards due to their high free lime content, which results in expansive properties and produces volumetric instability of the concrete.[38,42–44]

The U.S. produces greater than 17 million tons of slag,[45,46] and the worldwide generation of iron and steel slag byproducts – with a CaO content ranging between 20% to 50 % by mass[39,47] – was estimated to be 180 to 270 million tons in 2020 according to the U.S geological survey (USGS).[48] These materials are not only produced in large amounts on an ongoing basis, but historical reservoirs in the U.S. and across the world host well over a billion tons of slag.[49–51] Moreover, disposing underutilized quantities of alkaline wastes in landfills implies a waste disposal cost ("tipping fees", N.B.: the average tipping fee in the U.S. is on the order of \$50 per t[52]) and can result in environmental damage.[47,53–55]

## 1.5. Motivation of the study

Notwithstanding the environmental applications of $Ca(OH)_2$ and the promise that it can drive a greener construction industry when used in alternative cement formulations to replace OPC, its production process is still emitting too much $CO_2$ from the calcination of limestone. Thus, the production of this material should be radically transformed to bypass the use of carbonate rocks and prevent the release of billions of tons of $CO_2$ deposits that have been stored for millennia.

Hence, with the goal to enhance waste utilization, resource recovery and reutilization, we demonstrate an approach to extract calcium from slag,[56,57] and produce $Ca(OH)_2$ via aqueous precipitation by heating (up to 100 °C) the calcium-containing solution. This processing route is in line with the principles of circular economy because it enhances resource recovery from industrial byproducts[58] and it has the potential to reduce the environmental impacts of landfilling slag and quarrying and burning limestone.[9] The process could be implemented in industrial facilities with large availability of waste heat, such as thermal power plants, cement, or steel production plants.

While herein we focus on slag, of course, the broad contours of this process are also applicable to other alkaline industrial wastes such as fly ash from coal combustion. For example, even now the U.S. produces 91 million tons of coal combustion residuals, of which only 58% are beneficially utilized.[59] And, global waste reservoirs host tens of billions of tons of fly ash,[60–62] based on broad estimates. Other suitable calcium sources could be alkaline rock species, which although harder to solubilize unless externally stimulated,[63,64] offer a near-limitless source for alkaline element extraction.

## 1.6. Objectives of the present study

The overall goal of this research is to develop a low-temperature calcination-free $Ca(OH)_2$ production route comprising three basic steps: (1) slag leaching, (2) concentration of leached calcium ions in solution using reverse osmosis (RO), and (3) precipitation of $Ca(OH)_2$ crystals through heating. The specific objectives that will be accomplished to fulfill the main research goal are: (i) to demonstrate the calcination-free production of $Ca(OH)_2$ using precursors such as iron/steel processing wastes on the laboratory scale, (ii) to design and build an optimized integrated pilot process demonstrating the production of 1 kg of $Ca(OH)_2$ per day, and (iii) to evaluate the commercial feasibility of the proposed process using elements of financial, $CO_2$ footprint, and geospatial analysis.

## 1.7. Organization of the document

Chapter 2 introduces and demonstrates the concept of obtaining $Ca(OH)_2$ from alkaline industrial waste at sub-boiling temperatures (<100 °C) by performing bench-scale experiments to test each of the steps ─ *i.e.*, leaching, concentration, and precipitation ─ required to accomplish the process independently and separately. Additionally, a simplified energy analysis is used to compare the energy consumption of the proposed process with that of the traditional $Ca(OH)_2$ production.

Chapter 3 establishes the design and continuous operation of the low-temperature (< 95°C), aqueous-phase pilot-process to produce $Ca(OH)_2$ using calcium extracted from alkaline industrial wastes. The mass and energy balances were quantified to reveal that increasing the calcium concentration of the feed solution and the precipitation temperature, decrease the energy demands of the RO step, thereby reducing the process's overall $CO_2$ footprint. The pilot system was operated continuously in 3 independent tests and achieved an equivalent production rate of nearly 1 kg per day of $Ca(OH)_2$ with a purity greater than 95 wt.%.

Chapter 4 evaluates the economic feasibility and the $CO_2$ footprint of an optimized commercial-scale $Ca(OH)_2$ production facility based on the proposed process by minimizing the overall electricity consumption of the process. Additionally, a geospatial analysis elucidated the locations in the U.S. with better conditions to integrate the technology in existing power plants. The main factors considered in the study were the source and geospatial availability of electricity (*e.g.*, coal, natural gas, wind), waste heat, and slag. Finally, Chapter 5 summarizes the findings of this PhD dissertation, provides recommendations, and expands on topics for future research.

# CHAPTER 2

## Proof-of-Concept Demonstration

This chapter demonstrates a novel aqueous-phase calcination-free process to precipitate $Ca(OH)_2$ from saturated solutions at sub-boiling temperatures in three steps. First, calcium was extracted from an archetypal alkaline industrial waste, a steel slag, to produce an alkaline leachate. Second, the leachate was concentrated using reverse osmosis (RO) processing. This elevated the Ca-abundance in the leachate to a level approaching $Ca(OH)_2$ saturation at ambient temperature. Thereafter, $Ca(OH)_2$ was precipitated from the concentrated leachate by forcing a temperature excursion in excess of 65°C while exploiting the retrograde solubility of $Ca(OH)_2$.

### 2.1. Background

Figure 2.1. shows a process flow diagram (PFD) of a low-temperature, calcination-free route for $Ca(OH)_2$ synthesis including leaching, concentration, and precipitation steps. The conceptual basis of the new process involves the leaching/dissolution of Ca-bearing wastes to mobilize Ca-species in solution. This results in an aqueous Ca-abundance that is typically substantively lower than the saturation concentration of $Ca(OH)_2$ (~21.2 mmol/L at pH=12.475 and T=25 °C[65]).[39,56,57] Therefore, it is necessary to concentrate the leachate by a factor of 2 or more times depending on the initial Ca-content of the leachate. Such concentration is achieved by reverse osmosis (RO) based ion- separations wherein by means of size and/or charge exclusion;[66] divalent cations (e.g., $Ca^{2+}$, $Mg^{2+}$) can be enriched in the retentate stream. The retentate is then subjected to a temperature swing, e.g., using low-grade waste heat (≤100°C) as derived from the flue gas of a power plant or another heavy industry operation, wherein the retrograde solubility of $Ca(OH)_2$[67] ensures its precipitation to an increasing extent with increasing temperature.

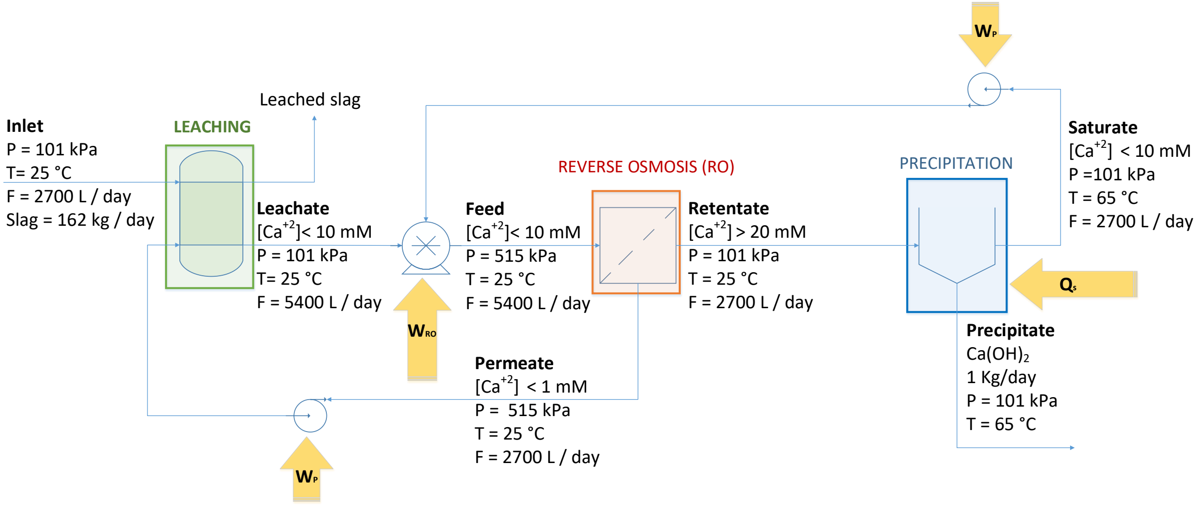

Figure 2.1. A process flow diagram (PFD) of a low-temperature, calcination-free route for Ca(OH)2 synthesis including leaching, concentration, and precipitation steps. Additionally, saturate and permeate recirculation is included to minimize water consumption. Yello Yellow arrows indicate energy inputs required to drive the process. Temperature T, pressure P, water flow rate F, and slag input are indicated in each of the streams. Flow rates were calculated based on a production throughput of 1 kg per day of $Ca(OH)_2$.

The advantage of such a low-temperature approach is straightforward: it obviates the need for limestone's decarbonation and eliminates the associated $CO_2$ emissions. Moreover, the precipitation step can be accomplished at ambient pressure and at sub-boiling temperatures. These general characteristics facilitate Process Intensification (PI) by renewable electrification and/or renewable heat (solar thermal) integration. Towards this end, we establish the feasibility of the low-temperature process, assess its limitations, and finally compare its energy and $CO_2$ intensity to incumbent methods.

## 2.2. Materials and Experimental Methods

### 2.2.1. Slag leaching

Slag leachates were prepared by contacting 1, 3, 5, and 10 g of a basic oxygen furnace (BOF) slag (i.e., a crystalline slag[i]) with 100 mL DI water to achieve solid to liquid mass fractions (s/l) of 0.01, 0.03, 0.05, and 0.1, respectively. To prepare the slag for leaching, slag fines (<9.5 mm) were dried at 70 °C for 24 h, ground for 1 hour in a planetary ball mill (MSK-SFM-1), and manually sieved to retain particles with a size lower than 106 µm. Batch leaching was conducted in 200 mL plastic bottles under either unstirred or stirred conditions at room temperature. Stirring was controlled using a Corning LSE orbital shaker (6780 NP) at 200 rpm. Solution aliquots of 2 mL were extracted after 0, 5, 10, 30, 60, 180, 360 and 720 minutes for analysis of total dissolved calcium, silicon, sodium, aluminum, and magnesium analysis using a Perkin Elmer Avio 200 inductively coupled plasma – optical emission spectrometer (ICP-OES). Prior to elemental analysis, the samples were filtered through 0.2 µm syringe filters and then diluted in 5 vol.% $HNO_3$. The ICP-OES was calibrated using standard solutions containing the elements of interest in concentrations of 0, 0.1, 1, 10, 25, 50, and 100 ppm which were prepared using analytical (1000 ppm) standards purchased from Inorganic Ventures.

The chemical composition (in mass %) of the simple oxide constituents of the slag was measured using X-ray fluorescence (XRF). The BOF slag was dominantly composed of CaO (38; wt.%), followed by $Fe_2O_3$ (31%), $SiO_2$ (13%), MgO (6%), and $Al_2O_3$ (4%). This information was used to

---

[i] Crystalline slags, unlike their amorphous counterparts (e.g., of which, the latter find use as cement replacement agents, that is, as supplementary cementitious materials: SCMs) – on account of their unreactive nature – are considered to be a low-value waste that is difficult to valorize, and that is often associated with a waste disposal (tipping) fee. For this reason, and in view of their Ca-based alkalinity which is equivalent to amorphous slags, we intentionally sought to use these less-reactive materials as a feedstock in our low-temperature process.

quantify calcium extraction ($X_{Ca}$) according to: $X_{Ca} = \frac{n_{Ca,sln}(t)}{n_{Ca,slag}}$, where $n_{Ca,sln}(t)$ are the moles of calcium in the solution at time t, and $n_{Ca,slag}$ are the moles of calcium in the solid slag as measured by XRF. The calcium leaching rate $\dot{n}_{Ca}$ (in mmol Ca / h) at time $t$ was defined as: $\dot{n}_{Ca} = \frac{[Ca](t,S/L)}{t} V_b$, where $V_b$ is the solution volume and t is the leaching time. The leaching rate affects the production rate ("yield") of $Ca(OH)_2$, and the efficiency of slag valorization because, from stoichiometry, one mole of Ca-leached from the slag should produce one mole of $Ca(OH)_2$ as per the reaction: $Ca^{2+} + 2OH^- \leftrightarrow Ca(OH)_2$.

### 2.2.2. Reverse Osmosis Concentration

RO concentration was carried out using two calcium-rich alkaline solutions, namely a reagent grade $Ca(OH)_2$ solution and a slag leachate solution. Reagent grade $Ca(OH)_2$ was added to 1 L deionized (DI) water (resistivity ≥ 18.2 MΩ·cm) to produce 5- and 10- mmol/L (mM) reagent grade $Ca(OH)_2$ solutions. On the other hand, the slag leachate was prepared by leaching, over time, 150 g of as-received basic oxygen furnace (BOF) slag into 3 L of DI water (s/l = 0.05) at 25 °C. The concentration of total dissolved calcium [Ca] in the solution after leaching was ~14 mM, whereas sodium, potassium, silicon, and aluminum impurities were present in concentrations lower than 0.1 mM, as measured by ICP-OES. The concentration of [Ca] in the leachate was adjusted to 5 mM and 10 mM by dilution with DI water to obtain 1 L of solution. Thereafter, the solutions were concentrated using a cross-flow flat-sheet membrane cell (CF042 Sterlitech Corp) fitted with thin film composite (TFC) polyamide RO membranes sourced from Dow Filmtec® (BW30XFR) with an active area of 42 $cm^2$. Prior to each experiment, the membranes were pre-treated by soaking them in DI water for at least 24 hours. A new membrane was used for each experiment to ensure reproducibility. Additionally, a gear pump (GJ Series Micropump®) was used to pressurize the Ca-containing solutions through the membrane. Furthermore, 99% pure $N_{2(g)}$ at atmospheric pressure was continuously bubbled into the feed tank at a flowrate of 0.02 L/min to minimize the presence of atmospheric $CO_2$ and to avoid the carbonation of the alkaline Ca-rich solution, and the resulting (undesirable) formation of $CaCO_3$.

The feed stream, with an initial Ca-concentration $[\mathrm{Ca}]_\mathrm{i}$ of 5 or 10 mM, was pressurized through the RO membrane at constant flow rate of 120 mL/min and gauge pressure of 413 kPa. A by-pass line was used to maintain a constant feed pressure throughout the duration of the experiment. The retentate was recirculated back to the feed tank for further concentration while the solution that permeated through the membrane was collected in the permeate tank. The concentration of calcium as a function of time was measured by taking 5 mL aliquots from both the feed $[\mathrm{Ca}]_\mathrm{f}$ and the permeate $[\mathrm{Ca}]_\mathrm{p}$ tanks every hour. Additionally, the permeate mass flow rate was monitored using an analytical balance (mass resolution: 1 mg) and a timer. A schematic of the RO experimental setup is shown in Figure 2.2.

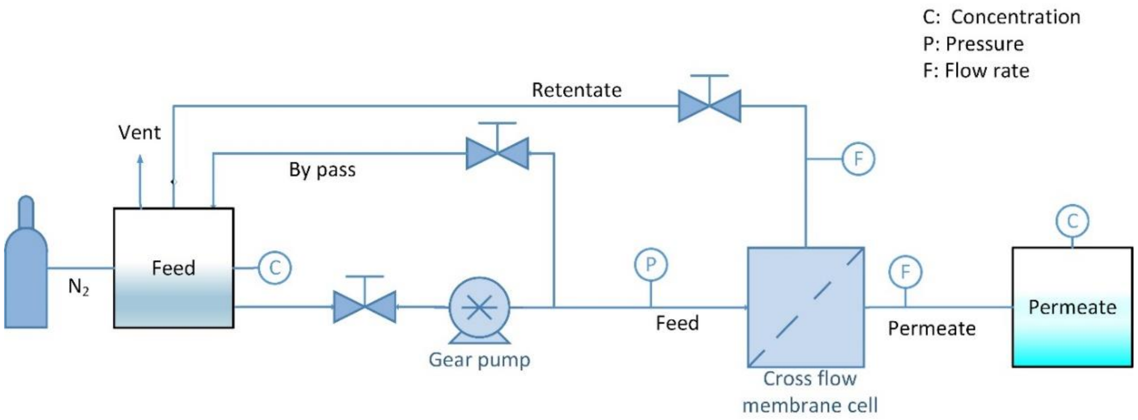

Figure 2.2. A schematic of the batch RO concentration setup showing cross flow membrane cell, feed, and permeate tanks, gear pump and streams configuration (retentate, permeate, bypass, and nitrogen lines). The circled C, P, and F indicate the location of concentration, pressure, and flow rate measurement sensors, respectively.

The performance of the RO system was assessed based on three typical metrics: (i) the water recovery Y, (ii) the salt rejection R, and (iii) the concentration factor CF. The water recovery Y (in %), represents the ratio of water volume recovered as permeate $V_p$ (in L), to the initial volume of solution $V_i$ (in L), i.e.,[68] $Y = \frac{V_P}{V_i}$. Note that in industrial systems, the water recovery Y ranges typically between 35%–85%.[68–71] In addition, salt rejection R (in %) represents the fraction of dissolved species that did not pass to the permeate side i.e., the percentage of Ca-rejected by the membrane which is expressed as:[72] $R = \left(\frac{[Ca]_F - [Ca]_P}{[Ca]_F}\right)$, where $[Ca]_F$ and $[Ca]_P$ are the Ca-concentration in the feed and permeate solutions, respectively. For reference, NaCl rejection ranges from 95–99% for the membrane used herein. Finally, the retentate concentration factor $CF_R$ and the permeate concentration factor $CF_P$ were respectively defined as the ratio of $[Ca]_F$ and $[Ca]_P$ to the initial calcium concentration in solution $[Ca]_i$.[73]

Following concentration, scaling was observed on the RO membranes. To analyze the mineral scale formed, the membranes were dried for 24 h under vacuum conditions. Thereafter, carbon tape was used to remove the scale and to mount it on a metallic support. The morphology and elemental composition of the dried solids were evaluated using a FEI Nova 230 Scanning Electron Microscope fitted with an energy dispersive (SEM-EDS) X-ray analyzer under high vacuum conditions and at an accelerating voltage of 15 kV.

### 2.2.3. Calcium hydroxide precipitation by temperature swing

$Ca(OH)_2$ precipitation was carried out by adding reagent grade $Ca(OH)_2$ to 100 mL DI water to obtain solutions saturated in $Ca(OH)_2$ at 25 °C (~21 mM), and other solutions that contained 5 mM and 10 mM $Ca(OH)_2$.[67] In addition, the actual slag leachate obtained following RO concentration was also utilized in the precipitation experiments. The experiments were carried out by placing the solutions in a stirred jacketed glass reactor, which was connected to a circulating water bath (Polyscience AD07R-20) that was thermally equilibrated at 25 °C. The reactor was sealed with Parafilm™ to minimize evaporation and $N_{2(g)}$ was bubbled through the solution to inhibit $CO_2$ dissolution in water and the subsequent carbonation of $Ca(OH)_2$. To exploit the (inverse) solubility dependence of $Ca(OH)_2$ with temperature and to induce precipitation, the solution temperature was increased by circulating hot water through the jacketed reactor. Reagent grade $Ca(OH)_2$ solutions were heated to 85 °C at (actual) heating rates (dT/dt) of 10 °C/h, 27 °C/h, and 54 °C/h. The solution's electrical conductivity $\sigma_{\mathrm{exp}}$, pH, and temperature T were measured continuously using a ThermoScientific Orion Versa Star meter. These measurements were used to determine the onset of $Ca(OH)_2$ precipitation and the [Ca] concentration in solution according to:[74] $\sigma_{\mathrm{exp}} = \sum_{\mathrm{i}} \mathrm{z_i}\, \mathrm{c_i} \lambda_{\mathrm{i}}(\mathrm{T})$, where $\lambda_{\mathrm{i}}$ is the equivalent conductivity, $\mathrm{z_i}$ is the valence, and $\mathrm{c_i}$ is the concentration of each ionic species ($\mathrm{i} = \mathrm{Ca^{2+}, OH^{-}}$). The equivalent conductivity of any ionic species $\lambda_{\mathrm{i}}$ was calculated from the Onsager relations expressed as:[75] $\lambda_{\mathrm{i}}(\mathrm{T}) = \lambda_{\mathrm{i}}^{\mathrm{o}}(\mathrm{T}) - \mathrm{S_i}(\mathrm{T})\Gamma^{1/2}$, where $\lambda_{\mathrm{i}}^{\mathrm{o}}$ is the ionic conductivity of an ionic species at infinite dilution, S is a parameter dependent on the temperature, viscosity, and dielectric constant of the medium, and $\Gamma$ is the ional concentration of the solution (see Appendix A: ionic conductivity calculations).[75] In the case of precipitation using the concentrated slag leachate, the temperature was increased to 70 °C at a fixed rate of 27 °C/h.

To confirm the composition of the precipitates, following precipitation, the solution was vacuum filtered using Whatman filters (3-5 µm pore size) and a heated ceramic funnel to minimize the redissolution of the precipitated $Ca(OH)_2$. The crystals were then dried in an initially $N_{2(g)}$-purged desiccator for 24 h under vacuum at room temperature to remove water and minimize the carbonation of $Ca(OH)_2$. The dried solids were placed on a carbon tape for morphology and elemental analysis using SEM-EDS, as previously discussed. Further, a small amount (~3 mg) of dried $Ca(OH)_2$ crystals were characterized using thermogravimetric analysis (TGA) using a Perkin Elmer STA 6000. To do so, the sample was initially equilibrated at 35 °C for 5 min to establish a mass baseline and then heated gradually from 35 °C-to-900 °C at a rate of 10 °C/min while continuously monitoring the mass. Ultra-high purity $N_{2(g)}$ was circulated through the sample chamber at a flow rate of 20 mL/min. The mass change versus temperature revealed the presence and quantity of $Ca(OH)_2$ and $CaCO_3$ present on account of their characteristic thermal decomposition at temperatures in excess of ~400 °C[76,77] and ~600 °C,[78] respectively.

## 2.3. Results and discussion

### 2.3.1. Slag leaching

Figure 2.3 shows the calcium concentration [Ca] as a function of time (in log scale) for slag particles smaller than 106 µm leached in DI water under (a) unstirred and (b) stirred conditions. It indicates that [Ca] concentration increased, approximately by a factor of 2, from unstirred to stirred conditions during the first hour of reaction. Stirring enhanced the rate of slag dissolution because calcium transport from the solid/liquid interface to the bulk solution was aided by convective mass transfer, as opposed to unstirred conditions wherein dissolution is transport (diffusion) limited.[79] Increasing s/l resulted in larger [Ca] concentrations since adding more slag increased the amount of calcium available for leaching. Figure 2.3(b) indicates that the maximum [Ca] concentration obtained was on the order of 17.3 ± 3.1 mM for s/l = 0.1 after 6 h, under stirred conditions, which is around 75% of the saturation concentration of $Ca(OH)_2$ at 20 °C (22 mM).[65] The decrease in the [Ca] concentration after achieving its peak value is indicative of secondary precipitation that consumed some of the [Ca] in solution. Such secondary precipitation is consistent with the reduction in the [Si] concentration in the leachate at similar times (see Appendix A: Figure A1), suggesting the precipitation of a calcium silicate hydrate (C-S-H) phase.[80] As such, although calcium leaching is enhanced and somewhat accelerated by increasing s/l, the amount of [Ca] that can be sustained in solution is limited by the equilibrium solubility of one or more phases, including $Ca(OH)_2$.[56,81,82] In general, Figure 2.3(a-b) highlights that reducing s/l reduced the amount of Ca-extracted into solution, at shorter and longer reaction times, and independent of the stirring condition. It should be noted, however, that the amount of Ca-leached, depended strongly on the type of slag used (see Figure A2).[46,82–84] The implication: that certain slags may be more suitable than others for Ca-extraction, and that depending on the slag used, multiple (2 or more) concentration cycles may need to be carried out to sufficiently enrich the Ca-concentration in solution with obvious energy intensity implications. This issue while also applicable to fly ashes, is less relevant, since fly ashes, especially the CaO-rich variants rapidly mobilize their Ca-species in solution.[51,85,86] Figures 2.3(c-d) shows the calcium extraction $X_{Ca}$ and the calcium leaching rate $\dot{n}_{Ca}$ as functions of time for different s/l for stirred conditions. Figure 2.3(c) shows that $X_{Ca}$ decreased with increasing s/l; *i.e.*, suggesting reducing efficiency of Ca-extraction from the slag with increasing s/l;[50] albeit offering meaningfully faster Ca-mobilization into solution [see Figure 2.3(d)].

Taken together, the data in Figure 2.3 indicates: a) larger s/l maximizes the amount of [Ca] leached and a smaller s/l maximizes $X_{Ca}$, b) with short duration leaching (in a single cycle), in the best case (s/l = 0.01, 24 hours leaching) no more than 8 mol % of the Ca-content of slag was extracted.[87] Finally and unsurprisingly, with increasing leaching time and a decreasing undersaturation with respect to the dissolving/leaching slag, the Ca-leaching rate decreased ($\dot{n}_{Ca}$) exponentially with time. Thus, practically, the leaching time should be reduced as much as possible[88] (i.e., $\leq$ 6 hours) to achieve a critical (minimal) Ca-content in solution as would be appropriate for the follow-on RO concentration step.

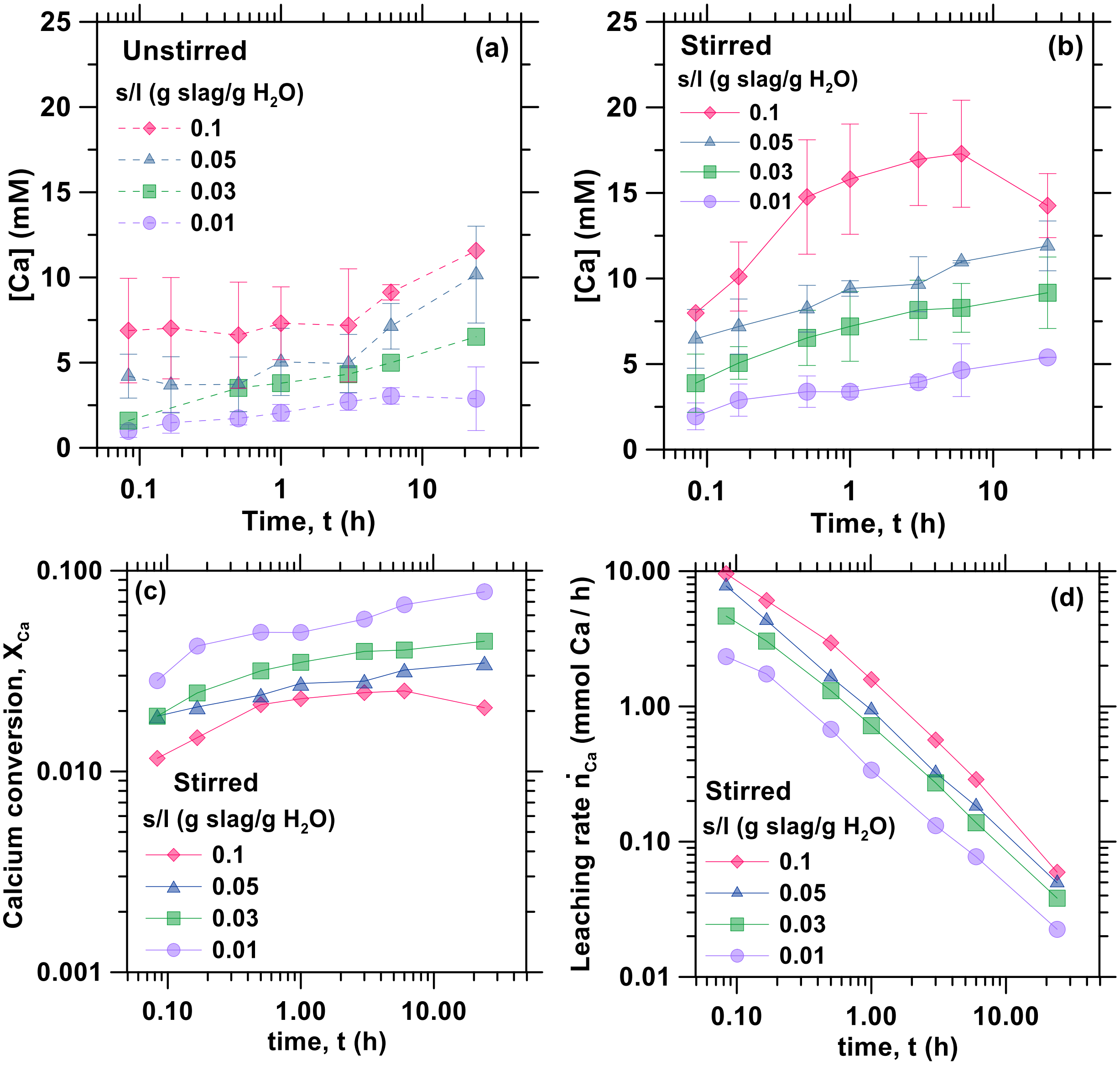

Figure 2.3. The aqueous [Ca]-concentration as a function of time during batch leaching of a BOF slag for s/l = 0.01, 0.03, 0.05, and 0.1 under (a) unstirred, and (b) stirred conditions. In general, increasing the s/l resulted in larger [Ca] concentrations since the enhanced quantity of slag increased the surface area, and amount of Ca-available for leaching in the solid phase. (c) The calculated calcium conversion $X_{Ca}$, i.e., the ratio (fraction) of the amount of Ca-in solution to the Ca-in the slag solids, and (d) The calcium leaching rate as a function of time for different s/l under stirred conditions.

.

### 2.3.2. Batch reverse osmosis concentration

Batch RO concentration was carried out using reagent grade $Ca(OH)_2$ solutions and slag leachate solutions. The processing of 1 L of feed solution took between 8 and 10 h for an average feed flow rate around 120 $cm^3$/min and gauge pressure of 413 kPa. The calcium concentration in the feed tank $[\mathrm{Ca}]_\mathrm{F}$ increased throughout the duration of the experiment while the calcium concentration in the permeate tank $[\mathrm{Ca}]_\mathrm{P}$ remained below 1 mM. The final calcium concentration in the feed tank $[\mathrm{Ca}]_\mathrm{F}$ readily approached the saturation level of $Ca(OH)_2$ (~21 mM at 25°C)[67] in both reagent grade $Ca(OH)_2$ and slag leachate solutions for an initial calcium concentration $[\mathrm{Ca}]_\mathrm{i}$ of 10 mM.

Figure 2.4 shows the permeate concentration factor $\mathrm{CF_P}$ and the retentate concentration factor $\mathrm{CF_R}$ as functions of time for: (a) reagent-grade $Ca(OH)_2$ solutions and (b) slag leachate solutions for initial feed calcium concentrations $[\mathrm{Ca}]_\mathrm{i}$ of 5 mM and 10 mM. It indicates that the retentate concentration factor $\mathrm{CF_R}$ was always smaller for the solutions with larger initial feed concentration $[\mathrm{Ca}]_\mathrm{i}$. This difference is on account of the osmotic pressure π, which is larger for solutions with a larger initial feed concentration $[\mathrm{Ca}]_\mathrm{i}$ according to the Van't-Hoff relation[89]: $\pi = \mathrm{R_U}\,\mathrm{T_F}(\,[\mathrm{Ca}]_\mathrm{F} + [\mathrm{OH}^-]_\mathrm{F})$, where $\mathrm{R_U}$ is the universal gas constant, $\mathrm{T_F}$ is the feed temperature and $[\mathrm{Ca}]_\mathrm{F}$ and $[\mathrm{OH}^-]_\mathrm{F}$ are the calcium and hydroxide concentrations in the feed solution, respectively. Since larger concentration leads to larger osmotic pressure π, the flow rate of permeate solution $\dot{\mathrm{V}}_\mathrm{P}$ crossing the membrane decreased according to[89]: $\dot{\mathrm{V}}_\mathrm{P} = \mathrm{A_m}\mathrm{L_p}(\Delta\mathrm{P}_{mem} - \Delta\pi)$, where $\mathrm{A_m}$ is the membrane area, $\mathrm{L_p}$ is the membrane permeability, $\Delta\mathrm{P}_{mem}$ is the pressure difference and $\Delta\pi$ is the osmotic pressure difference, between the feed and permeate solutions. Since the experiments were performed at a constant feed pressure, $\Delta\mathrm{P}_{mem}$ was constant. On the other hand, increasing the initial calcium concentration $[\mathrm{Ca}]_\mathrm{i}$ from 5 to 10 mM increased $\Delta\pi$, thus reducing the driving force $(\Delta\mathrm{P}_{mem} - \Delta\pi)$

and decreasing the permeate flow rate $\dot{V}_P$. Consequently, the retentate concentration factor $CF_R$ as a function of time was slightly lower for solutions with $[Ca]_i$ of 10 mM compared to 5 mM.

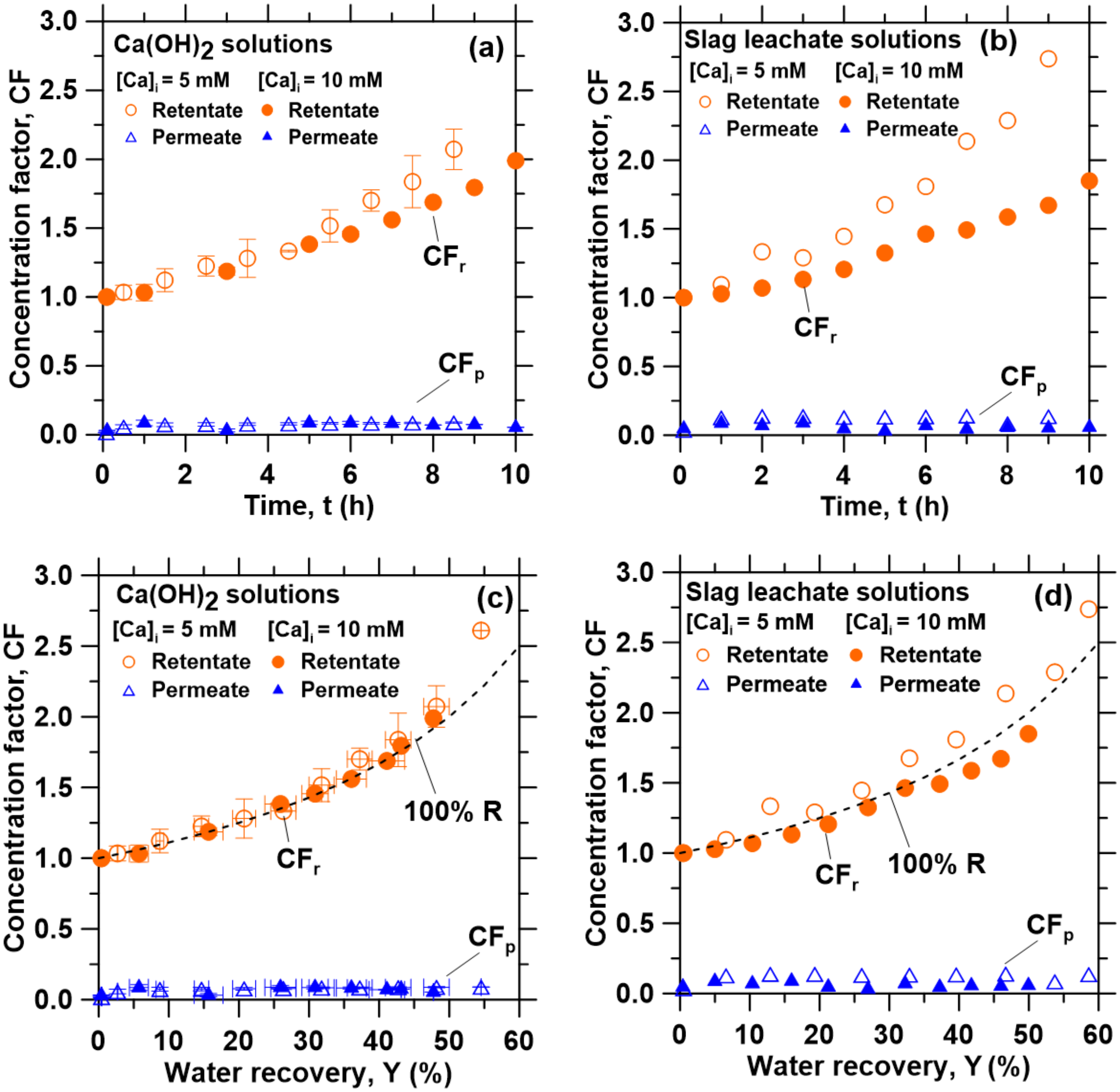

Figure 2.4. The permeate concentration factor $CF_p$ (blue) and retentate concentration factor $CF_r$ (orange) as a function of time for initial calcium concentration $[Ca]_i$ of 5 and 10 mM for: (a) reagent-grade $Ca(OH)_2$ solution, and (b) slag leachate solutions. RO concentration data showing permeate concentration factor $CF_p$ (blue) and retentate concentration factor $CF_r$ (orange) as a function of water recovery $Y$ for: (c) reagent grade $Ca(OH)_2$ solution, and (d) slag leachate solutions. The dashed line corresponds to maximum theoretical $CF_r$ assuming 100% calcium rejection by the RO membrane.

In addition, Figure 2.4 also shows the permeate concentration factor $CF_P$ and the retentate concentration factor $CF_R$ as a function of the water recovery $Y$ for reagent grade $Ca(OH)_2$ solutions and slag leachate solutions. Assuming that all the calcium in the feed solution was rejected by the membrane ($R = 100\ \%, CF_P = 0$), the maximum theoretical value of $CF_R$ can be calculated from a mass balance as [90]: $CF_R = \frac{1}{(1-Y)}$. Figure 2.4 (c-d) indicates that the calculated retentate concentration factor $CF_R$ follows the trend corresponding to 100% rejection for both reagent grade $Ca(OH)_2$ and slag leachate solutions. The slight deviation from the trend might be due to the uncertainties in calculating the permeate volume, which was not measured directly but estimated from permeate flow rate measurements. Moreover, Figure 2.4 reveals that the difference between the retentate concentration factor $CF_R$ calculated for the two initial feed concentrations ($[Ca]_i$ = 5 mM, 10 mM) was somewhat larger for the slag leachate solutions than reagent grade $Ca(OH)_2$ solutions. This observation could be due to either membrane degradation or membrane scaling. For example, membrane degradation may result in a decrease in the calcium rejection $R$ which would increase the Ca-concentration in the permeate $[Ca]_P$.[91] On the other hand, a typical sign of membrane scaling is a decrease in the permeate flow rate $\dot{V}_P$.[92–95] We observed that calcium rejection $R$ remained above 90% for both reagent grade $Ca(OH)_2$ and slag leachate solutions. This implies that $R$ was not affected by the presence of impurities in the slag leachate, and that membrane degradation was not significant (N.B.: This was also confirmed using longer duration testing carried out using a pilot-scale production system). On the other hand, significant differences were observed in the permeate flow rate $\dot{V}_P$. In fact, $\dot{V}_P$ remained constant at 0.9 ± 0.1 mL/min for both 5- and 10-mM reagent grade $Ca(OH)_2$ solutions, whereas it declined when water recovery reached 40% in the case of the 10 mM slag leachate solutions. This decline in $\dot{V}_P$ is attributed to scale formation on the membrane surface, *e.g.*, due to the formation of $Ca(OH)_2$, and/or hydrated calcium phases. Based on the retentate composition at 6 hours, $Ca(OH)_2$ and 11Å Tobermorite have saturation indexes of 0.03 and 2.35, respectively (See Figure A3) – suggesting their precipitation.[96,97] The results of the RO concentration and the equilibrium calculations also highlight that the solubility of portlandite decreased in comparison with reagent grade $Ca(OH)_2$ solutions, *i.e.*, on account of the common-ion effect, because the presence of other alkaline species (e.g., $Na^+$, $K^+$) in solution – extracted during leaching – alkalinizes the solution shifting the equilibrium towards $Ca(OH)_2$ precipitation.

Figure 2.5 shows SEM images of the mineral scale formed on the RO membranes after 10 h of concentration of a slag leachate solution with an initial calcium concentration $[Ca]_i$ of 10 mM. Here (and in the case of $Ca(OH)_2$ solutions), the crystallite size ranged from 100 μm to 300 μm. However, a higher area density of precipitates was observed on the membrane used for concentrating slag leachate solutions compared to that used with reagent grade $Ca(OH)_2$ solution. This suggests that the presence of impurities in the slag leachate enhanced scale formation; once again, on account of the common-ion effect. This also explains why the permeate flow rate decline was stronger with slag leachate solutions than with reagent grade $Ca(OH)_2$ solutions with the same initial calcium concentration. Nevertheless, scaling could be avoided through precautionary measures. For example, stopping RO concentration before reaching $Ca(OH)_2$ saturation, or reversing the feed flow direction periodically to change the saturation index of precipitate phases within the RO cell.[94,98]

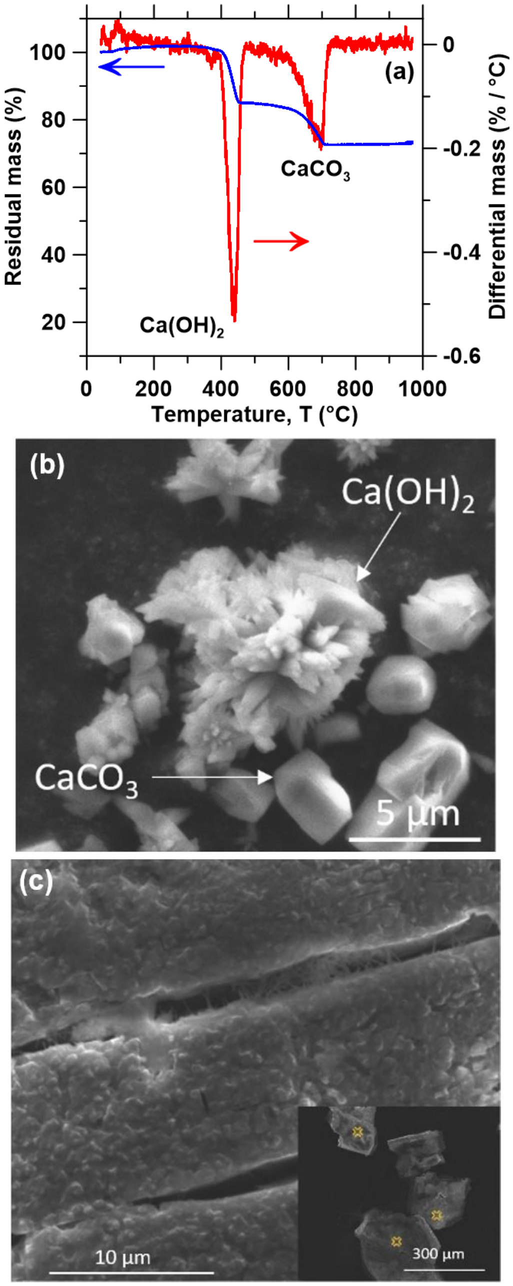

Figure 2.5. The characterization of precipitated $Ca(OH)_2$ crystals obtained from saturated slag leachate solutions using: (a) Thermal analysis showing evidence of $Ca(OH)_2$ and $CaCO_3$, respectively, (b) Micrographs confirming the presence of $Ca(OH)_2$ and $CaCO_3$, the former of which are identified by the hexagonal structure, and the latter by their equiaxed form, and (c) Micrographs of membrane scale obtained from slag leachate solutions. The yellow squares indicate the location of SEM-EDS sampling points

Table 2.1 summarizes EDS elemental analysis (in atom %) of crystallites deposited on the membrane surfaces (the sampling points are shown in the inset of Figure 2.5 c). The O-Ca ratio was noted as being 2 ± 0.3 across all solutions considered (see Table 2.1), whereas carbon, aluminum, and silicon were detected only in small quantities suggesting compositions consisting of mainly $Ca(OH)_2$, and small quantities of $CaCO_3$ and/or low-rank hydrated calcium-silicate compounds.[99]

Table 2.1. The elemental composition of the mineral scale formed on the RO membrane surfaces as analyzed using SEM-EDS.

| **Element (atom %)** | **$Ca(OH)_2$ solution** | **Slag leachate solution** |
|---|---|---|
| **Ca** | 32.55 ± 0.94 | 28.80 ± 2.68 |
| **O** | 60.89 ± 1.99 | 59.48 ± 7.48 |
| **C** | 6.47 ± 1.18 | 11.32 ± 9.74 |
| **Al** | 0.03 ± 0.01 | 0.14 ± 0.03 |
| **Si** | 0.06 ± 0.03 | 0.03 ± 0.02 |

### 2.3.3. Precipitation of calcium hydroxide from concentrated solutions

Following concentration, precipitation experiments were carried out using the reagent grade $Ca(OH)_2$ and slag leachate solutions. Temperature-swing induced precipitation was examined using concentrated slag leachates which featured a [Ca] concentration around ~19 mM (i.e., wherein the starting Ca-concentration was 10 mM). Herein, at 45 °C a change in the solution's appearance occurred (i.e., from transparent to translucent) corresponding to the formation of colloidal-scale and/or hyper-branched precipitates *(e.g.*, of C-S-H) that induced strong Tyndall scattering effects.[100,101] At the end of the temperature ramping process, ~3 mg of precipitates were collected (via filtration) from the saturated slag leachate solution.

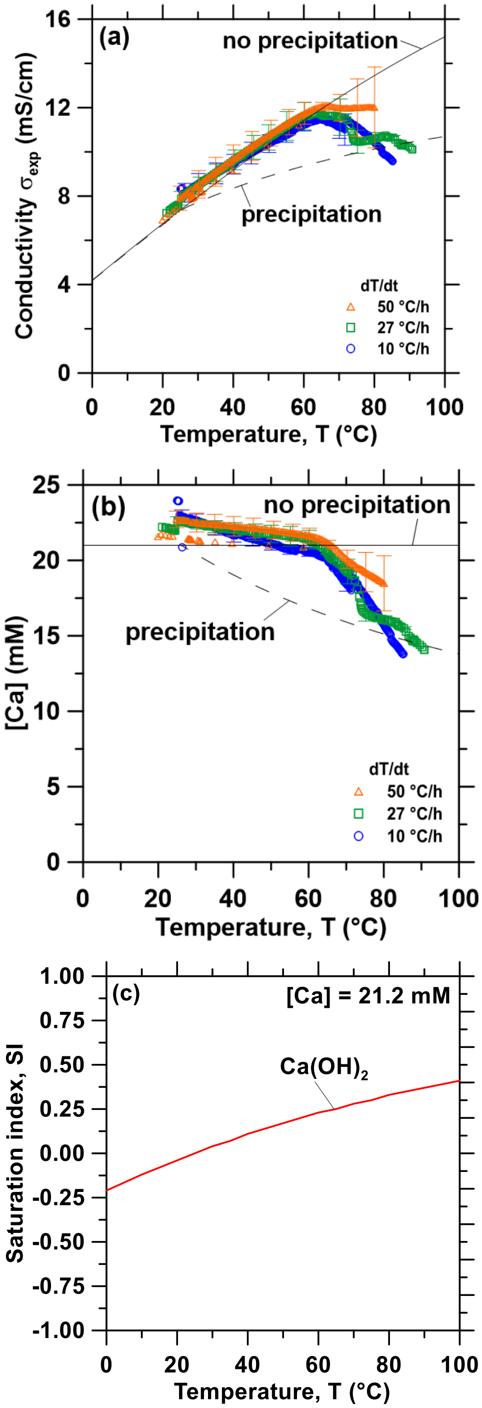

Figure 2.6. The measured: (a) solution's electrical conductivity as a function of temperature, (b) the corresponding [Ca] concentration (calculated from the measured conductivity), and (c) the saturation index (SI) (calculated using PHREEQC with minteq v4 database) as a function of the temperature for a solution with [Ca] = 21.2 mM, added as $Ca(OH)_2$. This data was obtained during the precipitation of reagent-grade $Ca(OH)_2$ solutions at different temperature ramp rates.

Figure 2.5 shows the characterization of precipitates obtained from the slag leachate using (a) TGA and (b) SEM. Herein, TGA [Figure 2.5(a)] shows that 66 mass % of the analyzed precipitates corresponding to $Ca(OH)_2$ started to decompose at 400 °C.[77,102] An additional 15 mass % of the precipitates started to decompose around 600 °C, indicating the presence of impurity $CaCO_3$ that formed due to: a) the presence of dissolved $CO_2$ in the feed water.[78] and/or, b) brief exposure of the wet $Ca(OH)_2$ precipitates to air during drying wherein they readily carbonate on contact with atmospheric $CO_2$.[103] The remaining 19 mass % impurities appear to be composed of slag particulates. As such, although the formation of $Ca(OH)_2$ was confirmed, it is important to control the ambient conditions during precipitation, separation and drying to avoid $Ca(OH)_2$ carbonation. Figure 2.5(b) shows representative SEM images of the precipitates whose particle size ranged between 2 and 10 µm. While it is indeed anticipated that particles smaller than 2 µm were present, they were not collected due to the large pores of the filter used for separation (>3 µm). Moreover, the precipitated crystals featured two differentiated morphologies: (i) small hexagonal platelet aggregates corresponding to $Ca(OH)_2$[104,105] and (ii) individual crystals with rhomb-like structures resembling $CaCO_3$.[106,107]

Finally, Figure 2.6 shows (a) the measured ionic conductivity, (b) the corresponding [Ca] concentration (*i.e.*, calculated using Equations (A1-A10)) as functions of temperature for different heating rates ranging from 10 to 50 °C/h for near-saturated reagent grade $Ca(OH)_2$ solutions, Also shown is the theoretical solution conductivity $\sigma_{\text{calc}}$ and estimated [Ca] concentration for a solution with an initial Ca-concentration of 21.2 mM: (i) in the absence of precipitation and (ii) during ongoing $Ca(OH)_2$ precipitation which acts to remove calcium and hydroxyl species from solution thereby resulting in a reduction of the solution conductivity. It is interesting to note that the onset of precipitation occurred at the same temperature across all heating rates, *i.e.*, as indicated by the reduction of the measured conductivity $\sigma_{\mathrm{exp}}$ vis-à-vis the calculated conductivity $\sigma_{\mathrm{calc}}$ and the [Ca] concentration in solution. Nonetheless, the heating rate may affect the precipitation kinetics[108,109] and final properties of the precipitates as shown, for example, for the aqueous precipitation of $TiO_2$ from $TiOCl_4$ solutions.[110] Overall, across all ramp rates, ~5 millimoles of $Ca(OH)_2$ per liter of solution were precipitated while heating to 85 °C, consistent with the calculated equilibrium precipitation yield based on the (retrograde) solubility of $Ca(OH)_2$.

The calculated saturation index (SI) of $Ca(OH)_2$ as a function of temperature for $[Ca]_{\mathrm{initial}}$ = 21.2 mM is shown in Figure 2.6(c). In qualitative compliance with classical nucleation theory (CNT), Figure 2.6 demonstrates that the rate of nucleation is negligible until a critical supersaturation, here 0.25 corresponding to the SI at T = 65°C, is reached.

### 2.3.4. Energy analysis

Energy and $CO_2$ balances associated with traditional and novel methods of $Ca(OH)_2$ production: The traditional pathway for $Ca(OH)_2$ production involves the thermal decomposition of limestone ($CaCO_3$) to lime (CaO) at 900 °C; following which the lime is slaked (hydrated) to produce $Ca(OH)_2$.[111,112] Here, high-grade heat is sourced from the combustion of fossil fuels. The enthalpic energy consumption $q_T$ to produce 1 kg of $Ca(OH)_2$ can be estimated (i.e., without considering thermal losses, or inefficiency) as $q_T = \frac{1}{M_{Ca(OH)_2}}(\Delta H_{rxn}) = 2.4\ \mathrm{MJ/kg\ Ca(OH)_2}$, where $M_{Ca(OH)_2}$ = 0.0741 kg/mol is the molar mass of $Ca(OH)_2$, $\Delta H_{rxn}$ = 179.2 kJ/mol $CaCO_3$ is the enthalpy of the calcination reaction $CaCO_3 \rightarrow CaO + CO_2$.[49] The thermal efficiency ($\eta = \frac{\Delta H_{rxn} * \dot{m}_{CaCO_3}}{\dot{m}_{fuel} * LHV}$) of a typical vertical shaft kiln – the lime industry standard – is around 60%.[112] Thus, the actual energy consumption of the traditional thermal process is on the order of 4 MJ/kg $Ca(OH)_2$,[113] and can be substantively larger for rotary lime kilns.[14,16,112]

The energy required to produce 1 kg of $Ca(OH)_2$ via the low-temperature precipitation process can be calculated based on mass and energy conservation principles, and the data from the prior sections (see Figure 2.1). For example, the mechanical work $w_{RO}$ necessary to pressurize the water through the RO system with a high-pressure pump was calculated to be 2.23 MJ/ kg $Ca(OH)_2$ according to $w_{RO} = V\Delta P,$ where $V$ = 5.4 $m^3$ is the total volume of solution to produce 1 kg of $Ca(OH)_2$ and $\Delta P$ = 414 kPa is the pressure difference between the pump inlet and outlet for the process conditions summarized in Figure 2.1. Similarly, the mechanical work of the low-pressure pumps $W_P$ can also be calculated as $\Delta P = \frac{8fL\rho\dot{V}^2}{\pi^2 D^5}$, where, $\Delta P$ is the pressure drop due to friction losses in pipes,[114] $D$ is the pipe diameter ($D$ = 0.009 m), $L$ = 1 m is the length of the pipe, $\rho$ = 1000 $kg/m^3$ is the solution density, and $f$ = 0.041 is Darcy's friction factor corresponding to the solution volumetric flow rate necessary to produce 1 kg of $Ca(OH)_2$ per day ($\dot{V}$ = $3.1 \times 10^{-5}$ $m^3/s$). Under these assumptions, $\Delta P$ is equal to 474 Pa. The mechanical work of the low-pressure pumps $W_P$ (is multiplied by 2 to account for the number of pumps) was 5.1 kJ/kg of $Ca(OH)_2$. This number is nearly three orders of magnitude lower than the work of the RO pump $w_{RO}$.

The sensible heat required to induce the temperature-swing, and in turn, portlandite precipitation, $q_p$ was estimated as follows. Previously, it was demonstrated that 5 millimoles of $Ca(OH)_2$ precipitate when heating near-saturated reagent grade $Ca(OH)_2$ solutions from 25 °C to 85 °C ($\Delta T$ = 60 °C). As such, following a simple mass balance, the mass of water to produce 1 kg of $Ca(OH)_2$ is $m$ = 2700 kg $H_2O$/kg $Ca(OH)_2$. Assuming > 90 mass % recovery of water, this translates into a consumable water demand of less than 270 kg $H_2O$/kg $Ca(OH)_2$. Thus, the sensible heat demand was calculated as $q_{s,p} = mc_p\Delta T =$ 677.15 MJ/kg $Ca(OH)_2$, where $c_p$ = 4.18 kJ/kg is the specific heat of water.[115] This indicates that the thermal energy demand for precipitation is two orders of magnitude larger than the mechanical energy consumption of the RO pump because only 0.37 g of $Ca(OH)_2$ is precipitated per liter of water. However, the thermal energy consumption could be reduced by more than 50%, *e.g.,* by implementing heat recovery loops. Furthermore, since the operating temperature for precipitation is below 90 °C, this energy could be sourced simply in the form of low-grade (e.g., flue gas borne) waste heat from industrial facilities such as thermal plants fired by coal, gas or nuclear power, steel processing facilities, and renewable heat sources like geothermal or concentrated solar power. For example, a mid-sized coal-fired power plants produces up to 5,000,000 GJ of low-grade thermal energy per year corresponding to exhaust temperatures up to 128 °C (at the stack).[116]

Table 2.2. A comparison of the energy intensity of traditional calcination and novel calcination-free $Ca(OH)_2$ production processes. Herein, for the "Novel" process, the thermal energy – being in the form of low-grade waste heat – is excluded from the analysis.

| Energy consumption (kJ/kg $Ca(OH)_2$) | | Traditional process | Proposed process |
|---|---|---|---|
| Total thermal energy | $Q_T$ | 4,000 @ 900 °C | 677,150 @ 85°C |
| Total work | $W_T = W_{RO} + W_P$ | --- | 2,241 |
| Total energy | $E_T = Q_T + W_T$ | 4,000 | 679,391 |
| Total high-grade energy | $E_T - Q_{s,alt}$ | 4,000 | 2,241 |

Table 2.2 compares the energy demand to produce 1 kg of $Ca(OH)_2$ via the traditional and a novel low-temperature precipitation process. It is noted that although the low-temperature process features a substantial energy demand – it is still attractive as it allows valorization of low-grade heat; that would, otherwise, be discarded. As such, if we focus on the "practical demand", the energy consumption of the novel process is ~44% lower than that of the traditional process. The main advantage of the alternative process, however, is that it obviates $CO_2$ emissions associated with limestone's decomposition, while allowing alkaline waste utilization. The alternative process requires 2241 kJ (0.62 kWh) of electrical energy per kg of $Ca(OH)_2$. Hence, assuming that 0.43 kg

of $CO_2$ are emitted per kWh of electricity consumed (e.g., corresponding to natural gas combustion, or 0.03 kg of $CO_2$ per kWh for renewable solar power[117,118])[119] and neglecting $CO_2$ emissions associated with low grade waste heat, the $CO_2$ emissions of the alternative process are on the order of ~0.27 kg $CO_2$ per kg of $Ca(OH)_2$. On the other hand, conservatively, 0.74-to-0.86 kg of $CO_2$ are produced per kg of $Ca(OH)_2$ in the traditional production process depending on the type of fuel utilized.[16] This estimate includes $CO_2$ released on account of the thermal decomposition of $CaCO_3$ [0.59 kg $CO_2$/kg of $Ca(OH)_2$] and the $CO_2$ emitted from natural gas combustion [0.15 to 0.27 kg $CO_2$/kg of $Ca(OH)_2$],[16,113] but these numbers could be larger for less efficient kilns.[14] Thus, the $CO_2$ emissions from the alternative process are only a third that of the traditional process. For these reasons, although more work remains, this style of low-temperature precipitation pathway, for portlandite production, is worthy of further work and consideration.

## 2.4. Conclusion

This study has demonstrated a calcination-free pathway to produce $Ca(OH)_2$ using industrial alkaline wastes as a feedstock. The process encompasses discrete unit operations including: leaching, RO concentration, and temperature-swing precipitation. In general, slag leaching in water can produce Ca-concentrations ranging from 2 to 17 mM depending on the slag, s/l, the presence of mixing (or not), and the leaching duration. The Ca-concentration in solution can be systematically enhanced using RO membrane filtration. Finally, the retrograde solubility of portlandite was exploited to precipitate it from near-saturated solutions of itself, by imposing a temperature swing. The quantity of portlandite precipitated in this manner was congruent with estimates from equilibrium thermodynamic calculations. Taken together, this process presents a (high grade) specific energy demand (kJ per kg of $Ca(OH)_2$) that is nearly 44% lower than traditional thermal processes; and importantly obviates the need to decarbonize limestone. As a result, this low temperature process presents a specific $CO_2$ intensity that is 65% smaller than conventional methods. This is significant as $Ca(OH)_2$ produced in this manner can uptake more $CO_2$ than it associated with its own production forming a basis for a truly $CO_2$-negative material.

# CHAPTER 3

## Pilot-scale Process Design and Demonstration

This chapter establishes the design and demonstrates the operation of a continuous, low-temperature (< 100°C), aqueous-phase pilot-process to produce $Ca(OH)_2$ using calcium extracted from alkaline industrial wastes. The three-step process encompasses unit operations including: (i) calcium leaching from basic oxygen furnace (BOF) slag, (ii) leachate concentration by reverse osmosis (RO), and (iii) $Ca(OH)_2$ precipitation. The mass and energy balances were quantified to reveal that increasing the calcium concentration of the feed solution and the precipitation temperature, decrease the energy demands of the RO step, thereby reducing the process's overall $CO_2$ footprint. The pilot system operated continuously and achieved a production rate of nearly 1 kg per day of $Ca(OH)_2$ with a purity greater than 95 wt.%. The average particle size of the precipitates depended on the residence time in the precipitation reactor, suggesting an ability to produce size-controlled particulates. Importantly, the process achieved full water recirculation/reutilization level indicative of a low-consumable water demand. The outcomes offer new insights and understanding relevant to developing and upscaling low-$CO_2$ processes for cement, lime, and portlandite.

### 3.1. Background

The proof-of concept was demonstrated successfully on the laboratory scale, albeit further research is still needed to validate the feasibility of the process. Regarding leaching, the previous chapter showed that when slag and water come in contact, a solution with calcium concentration ([Ca]) ranging from 2 to 17 mmol/L (mM) is obtained.[120] It also demonstrated that achieving large calcium concentrations in solution by increasing the solid to liquid ratio during leaching comes at the expense of calcium extraction efficiency.[120] Additionally, results indicated that the maximum calcium concentration that can be sustained in solution during leaching is lower than the saturation concentration of $Ca(OH)_2$ at room temperature, since the silicon from slag captures the dissolved calcium through the precipitation of calcium silicate hydrate phases which have lower solubility than $Ca(OH)_2$.[121–123] Although the method developed was demonstrated with BOF slag, other types of slag, fly ashes, and alkaline rock species can also release calcium through leaching.[39,53,56,57,85] The leachate was then concentrated through reverse osmosis (RO), wherein a membrane semipermeable to water rejects cations (e.g., $Ca^{2+}$, $Mg^{2+}$) by size and/or charge exclusion mechanisms,[66] producing a permeate stream with low ionic concentration and enriching the retentate stream up to the saturation point of $Ca(OH)_2$ (~21.2 mmol/L at pH = 12.5 and T = 25 °C [65]). In our previous research, batch RO experiments – wherein the concentration of the feed increases as a function of time – indicated that after 6 hours, membrane scaling hindered the concentration process, posing questions on the stability of the concentration step at longer times and larger scale. Finally, we demonstrated the precipitation of $Ca(OH)_2$ from the concentrated slag leachates by harnessing the retrograde solubility of $Ca(OH)_2$[67] when increasing the solution temperature above 65 °C. In total, we retrieved ~ 3 mg of precipitates from 0.5 L of solution with a purity of 66%. Although the quantity and purity of the synthesized $Ca(OH)_2$ crystals were low, achieving precipitation at sub-boiling temperature ($\leq$ 100 °C) demonstrated that the process can be scaled up using underutilized low-grade waste heat from industrial facilities.

In the previous chapter, each step of the proposed process was demonstrated separately but we did not show a continuous integrated process, a key step towards process intensification. In addition, the process could have a large water footprint, requiring 5400 L of water per kg of $Ca(OH)_2$ produced. Thus, water recirculation is essential to demonstrate that this technology is technically viable. Hence, this study aims to scale-up the three-step $Ca(OH)_2$ production method previously developed[120] by demonstrating a continuous pilot system capable of producing up to 1 kg of $Ca(OH)_2$ per day. The process design and the different operating conditions tested were guided by a steady-state model based on mass and energy conservation principles to study the influence of calcium concentration and precipitation temperature on the process energy consumption, production throughput, and properties of the $Ca(OH)_2$ produced.

## 3.2. Materials and methods

### 3.2.1. Materials

***Slag preparation and characterization***

500 kg of BOF slag were obtained from Stein Inc (Ohio, U.S) and milled in 5 batches for 2 hours by U.S.Stoneware (Ohio, U.S.) using a 27-gallon ball mill. The slag was then separated into different size fractions using a ro-tap ® Model B (W.S. Tyler Incorporated). Figure 3.1 shows (a) the particle size distribution and (b) the mineralogical composition of the BOF slag. The particle size distribution was measured using a Beckman Coulter LS 13-320 static light scattering analyzer by suspending the particles in DI water. The particle size distribution was used to calculate the geometric surface area (GSA) in $cm^2/g$ of the samples as[124]

$$GSA = \sum_{i}^{n} \frac{SA_i \varphi_i}{V_i \rho_{slag}} \tag{3.1}$$

where $\varphi_i$ is the volume fraction of particles with diameters between "$i$" and "$i+1$", $SA_i$ (in $cm^2$) and $V_i$ (in $cm^3$) are the surface area and volume of the sphere. The density of the slag $\rho_{slag}$ was assumed to be 3.46 $g/cm^3$.[125]

The mineralogical composition of the BOF slag was determined prior to and after 30 minutes of dissolution using X-ray diffraction (XRD). XRD analysis was performed using a PANalytical X'Pertpro diffractometer (θ-θ configuration, CuKα radiation, k = 1.54 Å). Scans were acquired between 5° and 70° with a step scan of 0.02° using a scientific X'Celerator 2 detector on powder samples. The following crystalline phases were detected in the slag before dissolution: portlandite – $Ca(OH)_2$ (PDF #04-010-3117), quartz – $SiO_2$ (PDF #04-012-0490), calcite – $CaCO_3$ (PDF #04-008-0788), larnite – $Ca_2SiO_4$ (AMCSD #0020214), brownmillerite – $Ca_2(Fe,Al)_2O_5$ (AMCSD # 0003434), Wüstite – FeO (AMCSD #0002758), Periclase – MgO (PDF #04-010-4039), Magnetite – $Fe_3O_4$ (PDF #04-005-4319), and Hematite – $Fe_2O_3$ (PDF #04-003-2900). All these crystalline phases are commonly found in BOF slag.[43,126] A broad peak at 2θ = 35° also indicated the presence of a significant fraction of amorphous content in the slag. Finally, the chemical composition (in mass %) of the BOF slag was measured using X-ray fluorescence (XRF). The slag was dominantly composed of $Fe_2O_3$ (65.9 %), followed by CaO (19.3 %), $SiO_2$ (7.1%), MgO (4.7%), and $Al_2O_3$ (1.71%).

### ***$Ca(OH)_2$ characterization***

The total mass of $Ca(OH)_2$ precipitated experimentally $m_{Ca(OH)_2,e}$ was determined as the sum of $Ca(OH)_2$ recovered in the filter bags and the $Ca(OH)_2$ precipitated on the surface of the reactor heaters. At the end of the experiment, the precipitated $Ca(OH)_2$ was collected, weighed, and stored under vacuum conditions at room temperature for one week for subsequent analysis. The mass of $Ca(OH)_2$ remaining on the filters was determined by drying the filters at 60 °C for 24 hours and calculating the difference in the dry filter mass before and after the tests. The mass production rate $\dot{m}_{Ca(OH)_2,e}$ of $Ca(OH)_2$ was estimated as the mass of $Ca(OH)_2$ measured experimentally divided by the duration of the experiment.

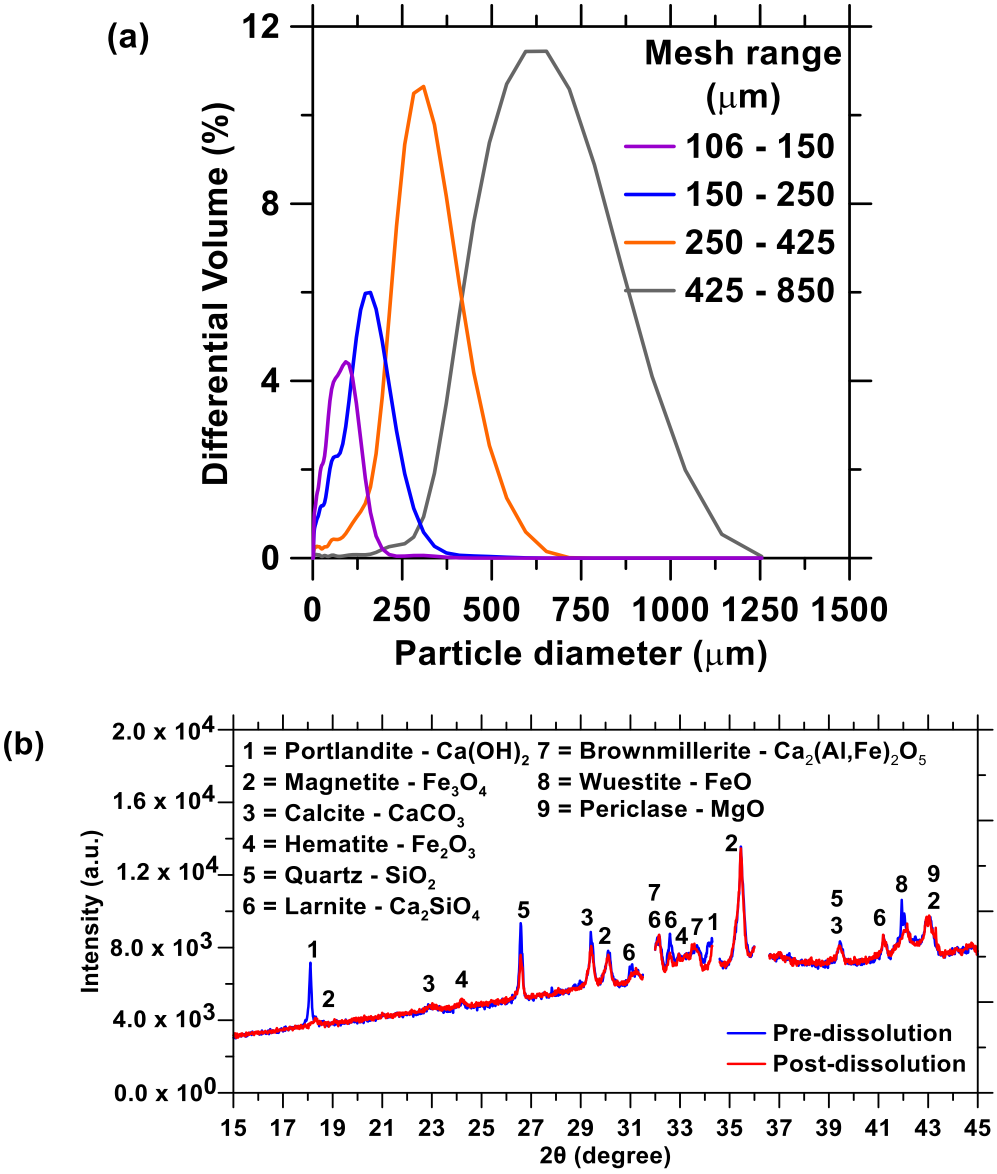

Figure 3.1. (a) particle size distribution of the slag and (b) XRD diffractogram of the slag before and after 30 minutes of dissolution in DI water. The results indicate that $Ca(OH)_2$ dissolution was predominant over any other phases present in the slag. Note that zincite (ZnO, 99.999%) was used as an internal standard for XRD analysis. Its peaks at 31.7º, 34.4º, and 36.2º 2θ are not shown here for clarity.

The $Ca(OH)_2$ crystals were characterized using thermogravimetric analysis (TGA), X-ray diffraction (XRD), and Scanning Electron Microscope (SEM). TGA was performed using a Perkin

Elmer STA 6000. To do so, the sample was initially equilibrated at 35 °C for 5 min to establish a mass baseline and then heated gradually from 35 °C to 900 °C at a rate of 10 °C/min while continuously monitoring the mass. Ultra-high purity $N_2$ gas was circulated through the sample chamber at a flow rate of 20 mL/min. The mass change versus temperature revealed the presence and quantity of $H_2O$, $Ca(OH)_2$ and $CaCO_3$ present on account of their characteristic thermal decomposition at temperatures in excess of ~100 °C, ~400 °C [76,77] and ~600 °C,[78] respectively. XRD analysis was performed as previously detailed for the slag characterization. Here, portlandite PDF #04-010-3117 was used as a reference. Finally, the morphology of the vacuum-dried crystals was evaluated using a G2 Phenom Scanning Electron Microscope fitted with an energy dispersive (SEM-EDS) X-ray analyzer under high vacuum conditions at an accelerating voltage of 15 kV.

### 3.2.2. Pilot system

#### ***Equipment***

Figure 3.2 shows (a) a schematic rendering and (b) a photograph of the experimental pilot system built to produce $Ca(OH)_2$. A video of the operation of the pilot system is presented in supplementary information. The main unit operations were leaching (batch operation), reverse osmosis (continuous operation), and precipitation (continuous operation). Leaching was carried out in a stirred leaching reactor comprised of a polyethylene cone tank (150 L) stirred by a Dayton drum mixer operating at 1700 rpm. Thereafter, two separation steps were used to remove the solids from the leachate. First, a trap for solid particulates (Gleco trap HV18 L capacity) was placed at the exit of the leaching reactor to separate the coarser grains of slag from the leachate. Second, a cartridge filter was placed at the exit of the leachate buffer tank to prevent particles larger than 5 µm from entering the feed reservoir. Each leachate batch was discharged to the leachate buffer tank (160 L) using a centrifugal pump (Iwaki NRD series) with 900 L/h capacity. A gear pump (micropump GJ series) was used to maintain a constant flow rate of solution from the leachate buffer to the feed reservoir and enabled the coupling of the batch leaching step with the continuous concentration and precipitation steps of the process.

Reverse osmosis concentration was performed by pressurizing the feed – with a Goulds pump (1SV30FF4C60) connected to an Aquavar intelligent pump controller – through two pressure vessels operating in series equipped with BW30-2540 Filmtec spiral wound membranes (5.2 $m^2$ total active membrane area). To minimize the water consumption, the permeate stream was recycled for leaching. Using the permeate buffer tank (160 L), the permeate stream was collected until the tank was full. Subsequent leaching batches were carried out using the permeate solution collected in the mentioned buffer tank by quickly transferring the permeate to the leaching tank using a submersible pump. Thus, the water was fully recirculated, and the process was sustained using only the water required to startup the system. The retentate stream was directed to a thermally insulated stainless-steel precipitation reactor (190 L) operating at a constant temperature of 95 ± 5 °C thanks to two Tempco electric heaters (6 kW each). Mixing in the precipitation reactor was achieved by using an electric mixer operating at 1750 rpm. After precipitation, the $Ca(OH)_2$ crystals were collected by pumping the saturated solution through a filter bag (pore size: 5 μm) with stainless steel housing. Thereafter, the filtered saturated solution was recycled back to the feed reservoir and mixed with the leachate stream. A copper coil placed inside the feed reservoir (1.3 $m^2$ heat exchange area) was used for cooling the feed stream by circulating 450 L/h of water at 18 °C.

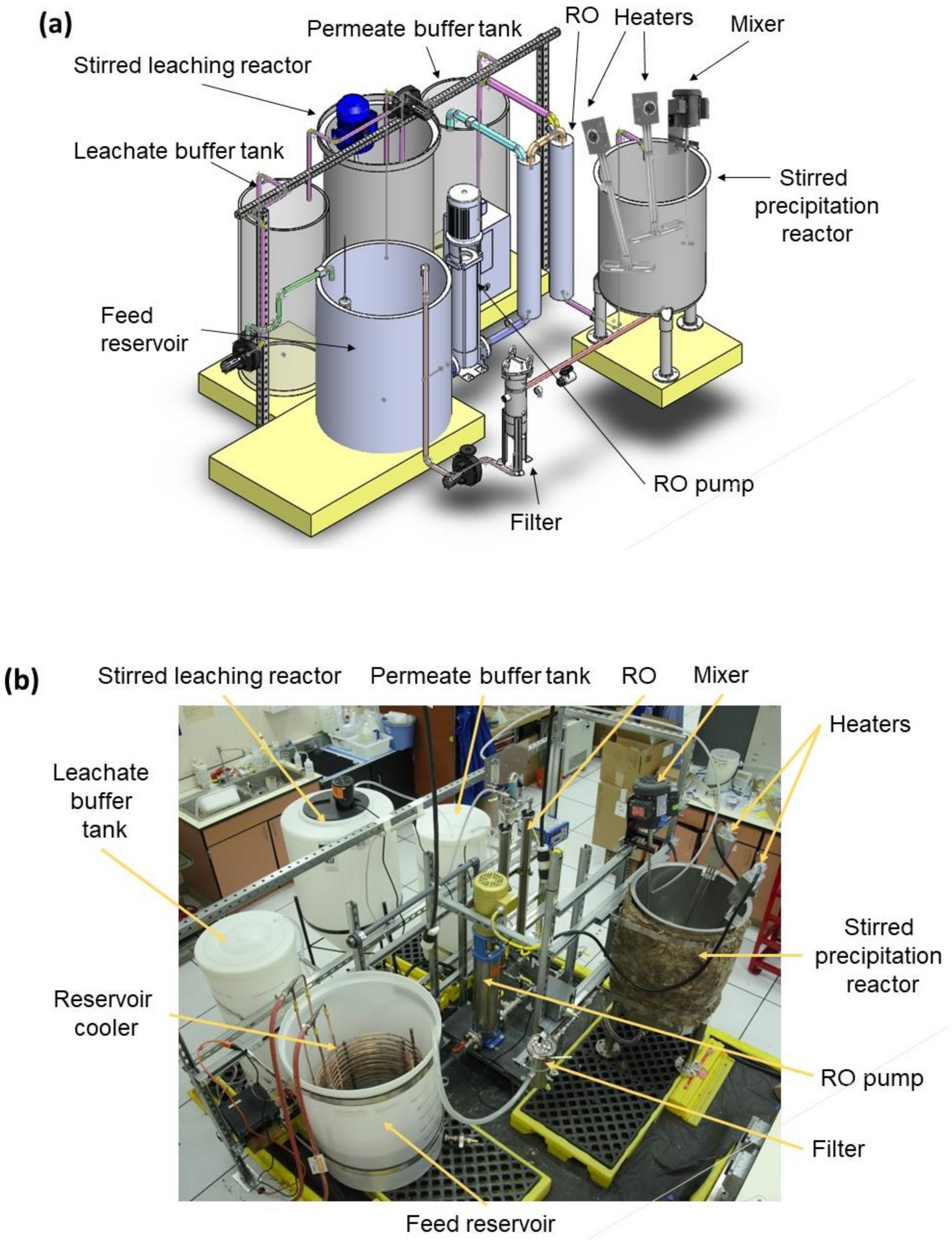

Figure 3.2. (a) A rendering of the pilot system at UCLA, and (b) a photograph of the experimental pilot system built to produce $Ca(OH)_2$.

### *Instrumentation and sampling*

The temperatures in the feed reservoir and in the precipitation reactor were continuously monitored using two Type-T thermocouples connected to a data acquisition card (NI-9213 connected to a NI USB-9162) and recorded using Labview V14. The pressure in the retentate stream and the conductivity in the feed reservoir were continuously measured using a data acquisition card Iotech DAQ 3000 Series using Dasylab V10 connected to a Balluf pressure and a conductivity meter (Omega CDTX-2853), respectively. The conductivity measurements were used to estimate the calcium concentration of the feed stream using a calibration curve relating conductivity to the total calcium concentration [Ca] (Figure B1). During continuous operation, the flow rates in the permeate, retentate, saturate, and leachate streams were recorded every hour using analog King flowmeters. In addition, 20 mL samples were taken every hour in each stream to test for concentration of dissolved species. Additionally, solution aliquots of 20 mL were extracted after 0, 5, 10, 20, and 30 minutes for every leaching batch. All samples were immediately filtered through 0.2 μm syringe filters to remove particulates and to avoid concentration changes in the sample. Analysis of total dissolved calcium concentration [Ca] was performed using a Perkin Elmer Avio 200 inductively coupled plasma – optical emission spectrometer (ICP-OES). Prior to elemental analysis, the samples were diluted in 5 vol. % $HNO_3$. The ICP-OES was calibrated using standard solutions containing calcium in concentrations of 0, 0.1, 1, 10, 25, 50, and 100 ppm prepared using analytical (1000 ppm) standards from Inorganic Ventures.

### *Startup procedure and operating conditions*

During the startup, 7.5 kg of basic oxygen furnace (BOF) slag were mixed with 150 L of water for 30 minutes to achieve a solid to liquid mass fraction (s/l) of 0.05 and [Ca] concentration of ~11 mM. Four leaching batches were used to fill the feed reservoir (300 L) and the leachate buffer tank with the leachate solution. Subsequently, the precipitation reactor was filled with concentrated leachate solution and heated to 95 °C. After the concentrated leachate achieved the desired temperature, the pumps feeding and draining the feed reservoir were turned on for continuous operation. Additionally, during continuous operation, the s/l ratio for leaching was switched from 0.05 to 0.03 to maintain a constant feed concentration $[Ca]_F$ of 10 mM and to minimize slag consumption.

Table 3.1. Operating conditions used to test the system during the pilot tests.

| **Pilot tests** | **1** | **2** | **3** |
|---|---|---|---|
| Average feed flow rate $\dot{\boldsymbol{V}}_{\boldsymbol{F}}$ (L/h) | 254 | 185 | 90 |
| Average saturate flow rate $\dot{\boldsymbol{V}}_{\boldsymbol{S}}$ (L/h) | 134 | 90 | 44 |
| Average leachate flow rate $\dot{\boldsymbol{V}}_{\boldsymbol{L}}$ (L/h) | 120 | 95 | 46 |
| Hours of continuous operation (h) | 8 | 12 | 24 |
| Average precipitation temperature $\boldsymbol{T}_{\boldsymbol{S}}$ (°C) | 87 | 95 | 95 |

The pilot was tested in continuous operation in 8- 12- and 24-hour trials, herein referred to as pilot test 1, 2 and 3, respectively. Table 3.1 shows the operating conditions of the three pilot tests. Different feed pressure and flow rates were tested to evaluate changes in the process efficiency or characteristics of the final product.

### 3.2.3. Energy balance

To perform a detailed energy balance of the process, we calculated the energy of grinding and mixing as well as the energy consumed for heating and pumping.

***Grinding energy consumption***

The specific energy consumption of grinding slag $w_{g,slag}$ (in kWh/ton slag) was given by [127]

$$w_{g,slag} = W_b\left(\frac{10}{\sqrt{d_f}} - \frac{10}{\sqrt{d_i}}\right) \tag{3.2}$$

where $W_b$ = 18.3 kWh/ton slag is the Bond work index of slag,[128] $d_i$ = 9500 μm is the initial particle size and $d_f$ = 100 μm is the desired final particle size. The energy associated with grinding for pilot tests 1, 2, and 3 was given by $W_g = w_{g,slag} m_{slag}$ where the total mass of slag $m_{slag}$ used was 48 kg, 50.5 kg, and 59.5 kg, respectively. The specific grinding energy consumption (per unit mass of $Ca(OH)_2$) was calculated by dividing the grinding energy by the total mass of $Ca(OH)_2$ produced: $w_g = W_g / m_{Ca(OH)_2,e}$.

***Mixing energy consumption***

The power consumption of the mixers $\dot{W}_m$ (in W) was computed according to[129]

$$\dot{W}_m = N_p \rho \omega^3 D_I^5 \tag{3.3}$$

where $N_p$ = 0.35 is the power number, $\rho$ = 1000 kg/m$^3$ is the density of the fluid, $\omega$ = 29 s$^{-1}$ is the rotation frequency (corresponding to a standard 1750 rpm electric motor), and $D_I$ = 0.095 m is the impeller diameter.[129] Each leaching batch was stirred for 30 minutes. Thus, the energy consumed by the mixer during leaching $W_{m,L}$ (in J) was expressed as

$$W_{m,L} = 1800 b \dot{W}_m \tag{3.4}$$

where b stands for the total number of leaching batches carried out during the experiments. Pilot tests 1, 2, and 3 consumed $b$ = 7, 9, and 11 leaching batches, respectively. The factor 1800 corresponds to the duration (in s) of each leaching batch. The mixer used in the stirred precipitation reactor was continuously active during the entire process. Thus, the mixing energy consumption of the continuously stirred precipitation reactor was given by

$$W_{m,P} = t \dot{W}_m \tag{3.5}$$

where $t$ is the duration of the continuous process (in s) and corresponds to 8, 12, and 24 hours for pilot tests 1, 2, and 3 respectively. The total energy consumed by the mixers in the entire process $W_m$ (in J) was expressed as

$$W_m = W_{m,L} + W_{m,P} \tag{3.6}$$

The specific mixing energy consumption (per unit mass of $Ca(OH)_2$) was computed by dividing the mixing energy by the total mass of $Ca(OH)_2$ produced: $w_m = W_m/m_{Ca(OH)_2,e}$.

## 3.3. Analysis

### 3.3.1. Assumptions

To design the pilot system, a steady-state model of the process was developed based on mass and energy conservation principles and validated using Aspen Plus v10 (Figure B2).[130] Figure 3.3 shows the process flow diagram of the model and the variables considered in each stream. The leaching process was not simulated because the rate and magnitude of calcium release from slag could be influenced by many factors such as the type of slag, the particle size, the solid to liquid mass fraction (s/l), and the type of leaching reactor, *e.g.*, batch, plug flow, continuously stirred reactor [56,57,88]. Instead, the leachate concentration $[Ca]_L$ was imposed to generalize the process to any type of alkaline leachate.

The model was based on the following assumptions: (i) The process operated at steady state. (ii) The fluid was incompressible. (iii) The solution density was independent of temperature and can be approximated as that of water. (iv) The leachate entered the feed reservoir with a leachate calcium concentration $[Ca]_L$ at flow rate $\dot{V}_L$. (v) The water was fully recirculated (i.e., $\dot{V}_L = \dot{V}_P$). (vi) The temperature, pressure, and concentration were uniform inside each unit operation. (vii)

The complexation of calcium ions in solution was not considered and calcium was present either as an ions $Ca^{2+}$ (hereafter referred to as [Ca]) or as solid $Ca(OH)_2$.

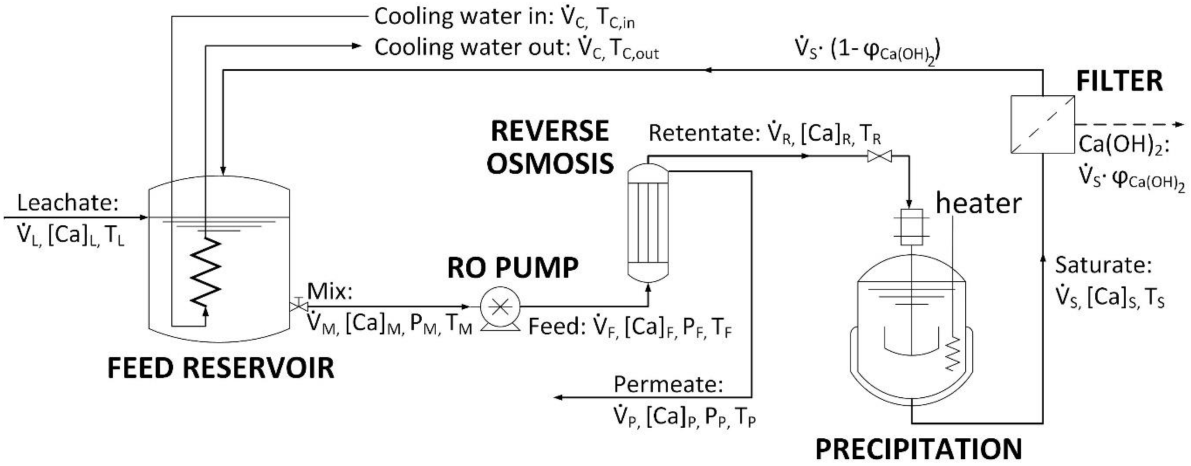

Figure 3.3. Process flow diagram of the steady-state model to produce $Ca(OH)_2$ from alkaline calcium-containing leachates. The streams and variables considered in the model include: the volumetric flow rate $\dot{V}$, the calcium concentration [Ca], the pressure P, and the temperature T.

### 3.3.2. Model governing equations

***Reverse osmosis (RO)***

The power delivered by the RO pump $\dot{W}_p$ to increase the pressure of the solution from atmospheric pressure ($P_M$ = 101325 Pa) in the feed reservoir to the desired feed stream pressure $P_F$ entering the RO unit was defined as[114]

$$\dot{W}_p = \frac{\dot{V}_F \, (P_F - P_M)}{\eta_p} \tag{3.7}$$

where $\dot{V}_F$ is the volumetric flow rate of the feed solution and $\eta_p$ = 0.8 is the hydraulic efficiency of the pump. Here also, the specific pumping energy $w_p$ (in J/kg of $Ca(OH)_2$) was calculated by dividing the pumping power by the $Ca(OH)_2$ production rate, i.e., $w_p = \dot{W}_p / \dot{m}_{Ca(OH)_2}$.

To model the RO membrane separation step, mass conservation equations for the solution and the calcium were expressed as

$$\dot{V}_F = \dot{V}_P + \dot{V}_R \tag{3.8}$$

$$\dot{V}_F\,[Ca]_F = \dot{V}_P[Ca]_P + \dot{V}_R[Ca]_R \tag{3.9}$$

where $\dot{V}_F$, $\dot{V}_P$, and $\dot{V}_R$ are the volumetric flow rates (in $m^3/s$) of the feed, permeate, and retentate streams, respectively. Similarly, $[Ca]_F$, $[Ca]_P$, and $[Ca]_R$ (in $mol/m^3$) are the calcium concentrations of the feed, permeate, and retentate streams, respectively. The volumetric flow rate of the permeate stream was given by[131]

$$\dot{V}_P = A_m L_p(\Delta P_{mem} - \Delta\pi) \tag{3.10}$$

where $A_m$ = 5.2 $m^2$ is the membrane area, $L_p$ = 8.64 x $10^{-12}$ $m^3/(s\ m^2\ Pa)$ is the membrane permeability estimated from experimental data[120] and reported in literature.[132–134] $\Delta P_{mem}$ is the transmembrane pressure difference defined as the difference between the feed $P_F$ and the permeate $P_P$ pressures, i.e., $\Delta P_{mem} = P_F - P_P$. The permeate stream was assumed to be at atmospheric pressure ($P_P$ = 101325 Pa). The osmotic pressure difference between the feed and the permeate solutions was computed according to[131,135]

$$\Delta\pi = R_U T_F[([Ca]_F + [OH^-]_F) - ([Ca]_P + [OH^-]_P)] \tag{3.11}$$

where $R_U$ = 8.314 J/mol·K is the universal gas constant and $T_F$ = 293 K is the feed solution temperature. The concentration of hydroxide ions $[OH^-]$ in the entire process was calculated based on the electroneutrality principle such that $2[OH^-] = [Ca]$. The permeate calcium concentration $[Ca]_P$ was calculated based on the membrane rejection coefficient $R = 0.99$ according to the membrane manufacturer so that

$$[Ca]_P = [Ca]_F(1 - R) \tag{3.12}$$

***Precipitation***

Following concentration in the RO unit, the retentate solution entered a continuously stirred precipitation reactor. The solution in this unit was assumed to be in equilibrium with the solid portlandite, i.e., $Ca^{2+} + 2OH^{-} \leftrightarrow Ca(OH)_{2\,(s)}$. The saturation concentration $[Ca]_s$ was calculated based on the solubility of portlandite as a function of temperature $[Ca]_s = f(T_s)$, plotted in Figure 3.4. The volume flow rate of solid $Ca(OH)_2$ exiting the crystallizer $\dot{V}_{Ca(OH)_2}$ was expressed as

$$\dot{V}_{Ca(OH)_2} = \dot{V}_s \varphi_{Ca(OH)_2} = \dot{V}_s \frac{M_{Ca(OH)_2}}{\rho_{Ca(OH)_2}}([Ca]_R - [Ca]_s) \tag{3.13}$$

where $\dot{V}_s$ is the saturate flow rate and $\varphi_{Ca(OH)_2} = \dot{V}_{Ca(OH)_2}/\dot{V}_s$ is the volume fraction of $Ca(OH)_2$ in the saturated solution. $\rho_{Ca(OH)_2}$ = 2.2 kg/m$^3$ is the density of $Ca(OH)_2$, $M_{Ca(OH)_2}$= 0.074 kg/mol is the molar mass of $Ca(OH)_2$ and $[Ca]_R$ and $[Ca]_s$ are the retentate and saturate total calcium concentrations, respectively. The mass flow rate of $Ca(OH)_2$ was calculated as $\dot{m}_{Ca(OH)_2} = \dot{V}_{Ca(OH)_2}\rho_{Ca(OH)_2}$. Since the volume fraction of $Ca(OH)_2$ is very small $\varphi_{Ca(OH)_2}$ ~ 2.6x10$^{-4}$ the volumetric flow rate of the retentate and saturated stream were assumed to be equal so that $\dot{V}_R = \dot{V}_s$. Now, the thermal power (in W) required for $Ca(OH)_2$ precipitation was written as

$$\dot{Q}_{heat} = \rho c_p \dot{V}_R (T_S - T_R) \tag{3.14}$$

where $\rho$ = 1000 kg/m$^3$ and $c_p$ = 4184 J/kg·K are respectively the density and heat capacity of the solution while $T_S$ and $T_R$ are saturate and retentate temperatures, respectively. The retentate temperature $T_R$ was assumed to be constant at 20 °C. The precipitation temperature $T_S$ was treated as an independent variable. The specific thermal energy $q_{heat}$ consumed during the precipitation process was calculated by dividing the heating power $\dot{Q}_{heat}$ by the $Ca(OH)_2$ mass production rate

$q_{heat} = \dot{Q}_{heat}/\dot{m}_{Ca(OH)_2}$. Due to the low solubility of $Ca(OH)_2$ in water, the saturate calcium concentration $[Ca]_S$ is expected to be on the order of 14 – 16 mM. Thus, to maximize the conversion efficiency of aqueous calcium into solid $Ca(OH)_2$, the saturated solution was recirculated back to the feed reservoir.

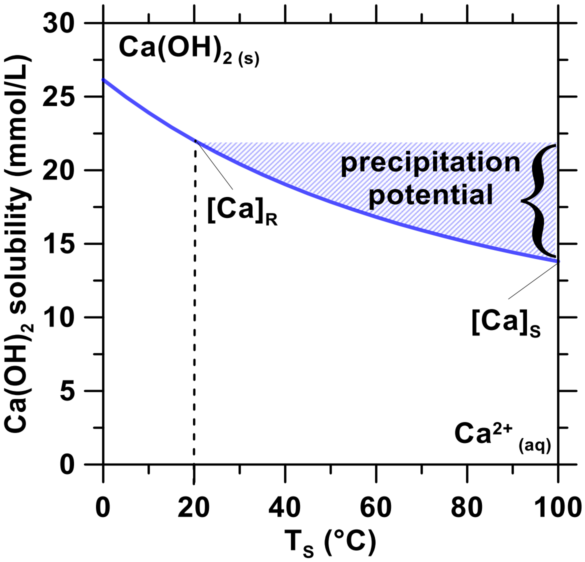

Figure 3.4. $Ca(OH)_2$ solubility as a function of temperature.[65]

***Feed reservoir***

To model the calcium concentration and volumetric flow rate at the exit of the feed reservoir, the mass conservation equations for the solution and calcium in the feed reservoir can be written as

$$\dot{V}_M = \dot{V}_L + \dot{V}_S(1 - \varphi_{Ca(OH)_2}) \tag{3.15}$$

$$\dot{V}_M\,[Ca]_M = \dot{V}_L[Ca]_L + \dot{V}_S(1 - \varphi_{Ca(OH)_2})[Ca]_S \tag{3.16}$$

where $\dot{V}_M$, $\dot{V}_L$, and $\dot{V}_S$ are the volumetric flow rates of the mixed, leachate, and saturate streams, respectively. And $[Ca]_M$, $[Ca]_L$, and $[Ca]_S$ are the calcium concentrations of the mixed, leachate, and saturate streams, respectively. The energy required to have a mix stream temperature $T_M$ of 20 °C can be expressed as [115]

$$\dot{Q}_{cool} = \rho c_p \dot{V}_M \left( T_M - \frac{\dot{V}_L T_L + \dot{V}_S (1 - \varphi_{Ca(OH)_2}) T_S}{\dot{V}_L + \dot{V}_S (1 - \varphi_{Ca(OH)_2})} \right) = \rho c_p \dot{V}_C \left( T_{C,out} - T_{C,in} \right) \qquad (3.17)$$

### 3.3.3. Method of solution

Figure 3.5 shows a block diagram of the solution method used to calculate the power consumption and the heating and cooling requirements to produce 1 kg of $Ca(OH)_2$ per day with the proposed three-step process. The model was initialized and solved by simple substitution based on the design constraints of the pilot system and validated using Aspen Plus V10.

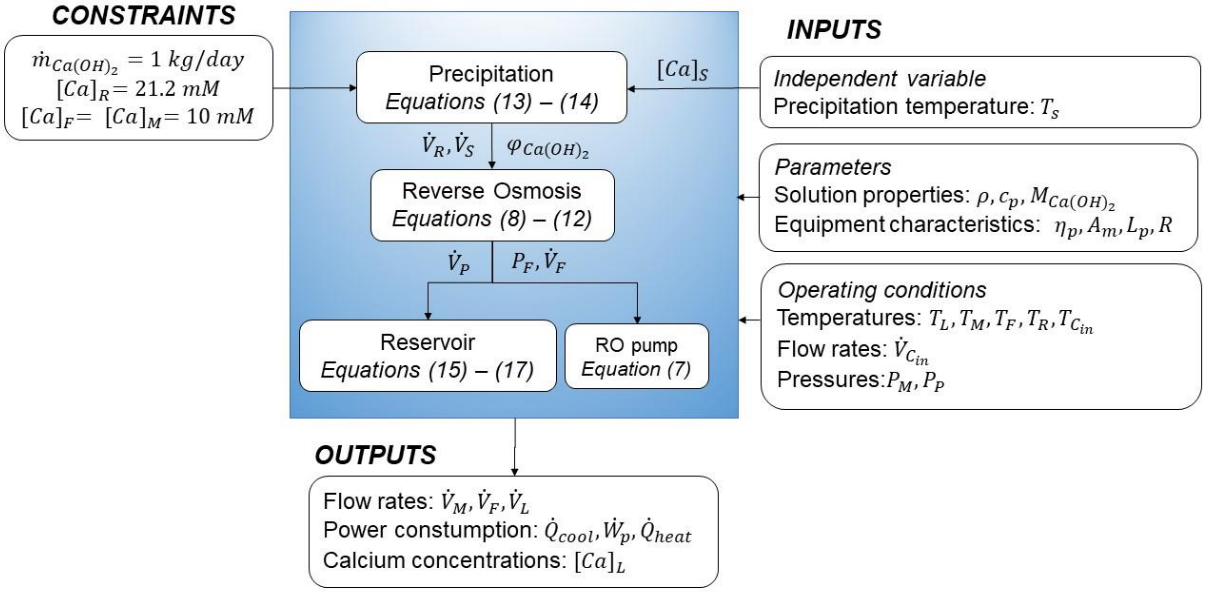

Figure 3.5. Block diagram of the solution method to predict the heat and power consumption of the $Ca(OH)_2$ production process for a rate of 1 kg per day.

The constraints used to initialize the model were (i) a $Ca(OH)_2$ production rate $\dot{m}_{Ca(OH)_2}$ of 1 kg per day, (ii) a retentate concentration $[Ca]_R$ of 21.2 mM, and (iii) a feed concentration $[Ca]_F$ of 10 mM. Then, the model was used to identify the influence of precipitation temperature and feed calcium concentration on the water consumption, and heating and pumping requirements of the process. The operating conditions of the experimental pilot process were optimized to minimize the pumping power of the RO-driven concentration, since the electricity consumption of this step drives the operating cost of the process. The overall energy consumption as a function of precipitation temperate was also evaluated, but the results were not used to guide the operation of the pilot system since the waste heat required for precipitation should be available from thermal power plants at low- or no cost.

## 3.4. Results and discussions

### 3.4.1. Modelling the effect of different operating conditions on power consumption

Figure 3.6 shows the model predictions for (a) the specific pumping power consumption $w_p$, (b) the feed flow rate $\dot{V}_F$ and pressure $P_F$, (c) the specific heat consumption $q_{heat}$, and (d) the total specific energy consumption $q_{heat} + w_p$ as functions of the precipitation temperature $T_S$ to achieve a retentate concentration $[Ca]_R$ of 21.2 mM and a mass production rate $\dot{m}_{Ca(OH)_2}$ of 1 kg of $Ca(OH)_2$ per day. Figure 3.6(a) indicates that the specific pumping energy consumption to drive the RO unit decreased exponentially with increasing precipitation temperature $T_S$. Because of the decreasing solubility of $Ca(OH)_2$ with increasing temperature, lower feed solution $\dot{V}_F$ and pressure $P_F$ were needed as the precipitation temperature increased [Figure 3.6(b)]. In addition, increasing the feed concentration $[Ca]_F$ to 15 mM further reduced the pumping power since a smaller degree of concentration was necessary to achieve the saturation point of portlandite in the retentate ($[Ca]_R$ = 21 mM) thereby decreasing the feed pressure $P_F$. However, this scenario might not be realistic considering that slag typically yields leachate calcium concentration $[Ca]_L$ below 10 mM. Nevertheless, it could be relevant when leaching other alkaline wastes or minerals.

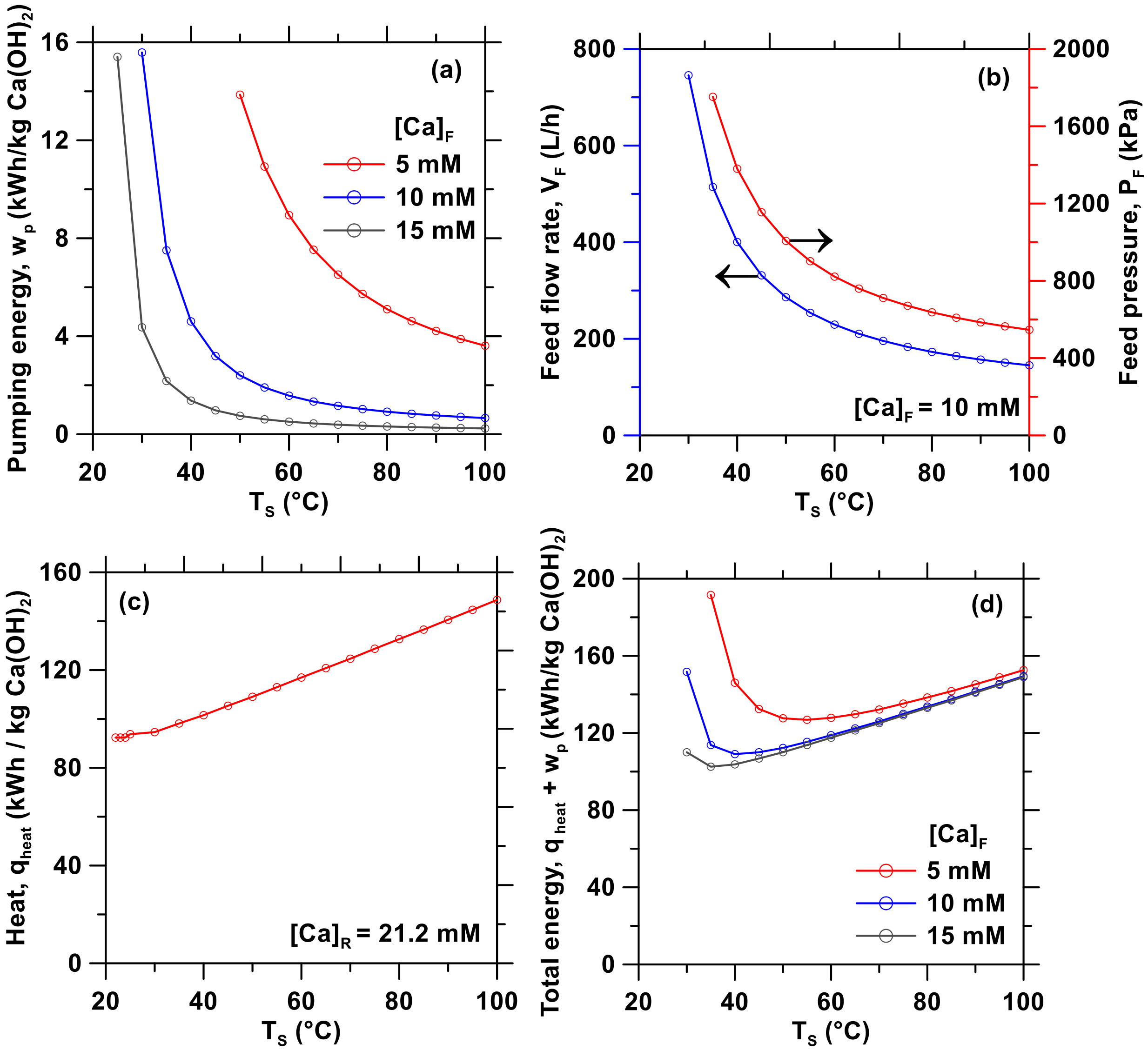

Figure 3.6. Predicted (a) specific pumping power consumption, (b) feed flow rate $\dot{V}_F$ and pressure $P_F$ for a fixed feed $[Ca]_F$ concentration of 10 mM, (c) specific heat consumption $q_{heat}$, and (d) total specific energy consumption $q_{heat} + w_p$ as functions of precipitation temperature assuming retentate $[Ca]_R$ concentration of 21.2 mM so as to produce 1 kg of $Ca(OH)_2$ per day.

As expected, Figure 3.6(c) shows that the thermal energy $q_{heat}$ required per kg of $Ca(OH)_2$ precipitate increased as the precipitation temperature increased. Finally, Figure 6(d) shows the total specific energy consumption is minimum when operating the precipitation reactor in the range of 40 °C to 55 °C, depending on the feed concentration. Below 40 °C, pumping requirements superseded thermal energy input. After 55 °C, the decrease in pumping energy consumption was marginal, and the heat consumption dominated. For upscaling purposes, although operating around 40 °C to 55 °C yields less $Ca(OH)_2$ per liter of solution, this temperature range is desirable as a large fraction of the waste heat in thermal power plants comes from condensers and is typically below 50 °C [116]. Moreover, the yield of $Ca(OH)_2$ precipitated per liter of solution and the specific RO pumping energy could be enhanced by operating the feed and retentate streams at ~5 or 10 °C to achieve larger concentration difference between the retentate $[Ca]_R$ and saturate $[Ca]_S$ streams. However, to demonstrate the continuous pilot process, we chose to operate the precipitation step at temperature $T_S$ = 95 °C to minimize electricity consumption for the RO pump and to maximize $Ca(OH)_2$ production throughput.

### 3.4.2. Slag leaching

***Insights on the dissolution of BOF slag in DI water***

Figure 3.1(b) shows the XRD patterns of BOF slag before and after dissolution. It indicates a complete dissolution of the slag portlandite content, whereas the other crystalline phases present in the slag were nearly undissolved after 30 minutes of leaching. Moreover, the broad amorphous peak intensity in XRD did not present significant differences before and after dissolution, indicating that the amorphous content of the slag was nearly insoluble. Thus, the results indicated that $Ca(OH)_2$ was the main source of calcium dissolved from slag. This was further confirmed by elemental analysis of the leachates showing that the concentrations of silicon, aluminum, sodium, and iron were at least one order of magnitude lower than the final concentration of calcium (see Figure B3 in supplementary material). This observation was consistent with the lower solubility and/or kinetic rate constant of the other phases present in slag compared to portlandite.[57] Typically, BOF slag is underutilized in the construction industry compared to other types of slag because its high free lime content may generate cracking in concrete.[136,137] This high free lime content was ideal for the present application, since larger calcium concentrations were leached from BOF slag than from other types of slag in DI water.[120]

### Effect of particle size distribution on leachate calcium concentration

Figure 3.7 shows the leachate concentration $[Ca]_L$ achieved experimentally as a function of time for a solid to liquid (s/l) ratio of (a) 0.03 and (b) 0.05. It also plots the initial ($t$ = 0 min) and final ($t$ = 30 min) leachate calcium concentration $[Ca]_L$ as a function of geometric surface area for a s/l ratio of (c) 0.03, and (d) 0.05. Figures 3.7(a) and 3.7(b) indicate that calcium leaching was fast initially, followed by a slower release after 10 minutes. The monotonic increase of $[Ca]_L$ for all s/l ratios and particle sizes considered indicated that little to no hydrated phases precipitated during slag dissolution. If other calcium phases had precipitated, the dissolved calcium in solution would have decreased eventually.[120] Figures 3.7(c) and 3.7(d) show that as the geometric surface area increased, the initial leachate concentration $[Ca]_L$ (at 0 min) approached a similar value (~8 mM) for both s/l ratios studied. Additionally, Figures 3.7(c) and 3.7(d) show that increasing the geometric surface area increased the dissolution rate,[138] since the leachate concentration $[Ca]_L$ difference between 0 and 30 minutes increased with increasing geometric surface area. To maximize the calcium conversion during leaching, decreasing the particle size and the leaching time seems more desirable than increasing the s/l ratio since the later results in larger raw material consumption. A potential drawback is that decreasing the particle size may increase other species dissolution and more specifically the Si-containing amorphous fraction.[138,139] This could lead to an increase of Si content in solution which could result in the formation of C-S-H phases instead of $Ca(OH)_2$. Thus, further experiments with smaller slag particle size should be evaluated to find the optimum leaching conditions where portlandite dissolution is maximized and is dominant over the dissolution of other phases in the slag. Moreover, when increasing the leaching time to maximize calcium dissolution, the stirring energy required for the leaching process should be minimized.

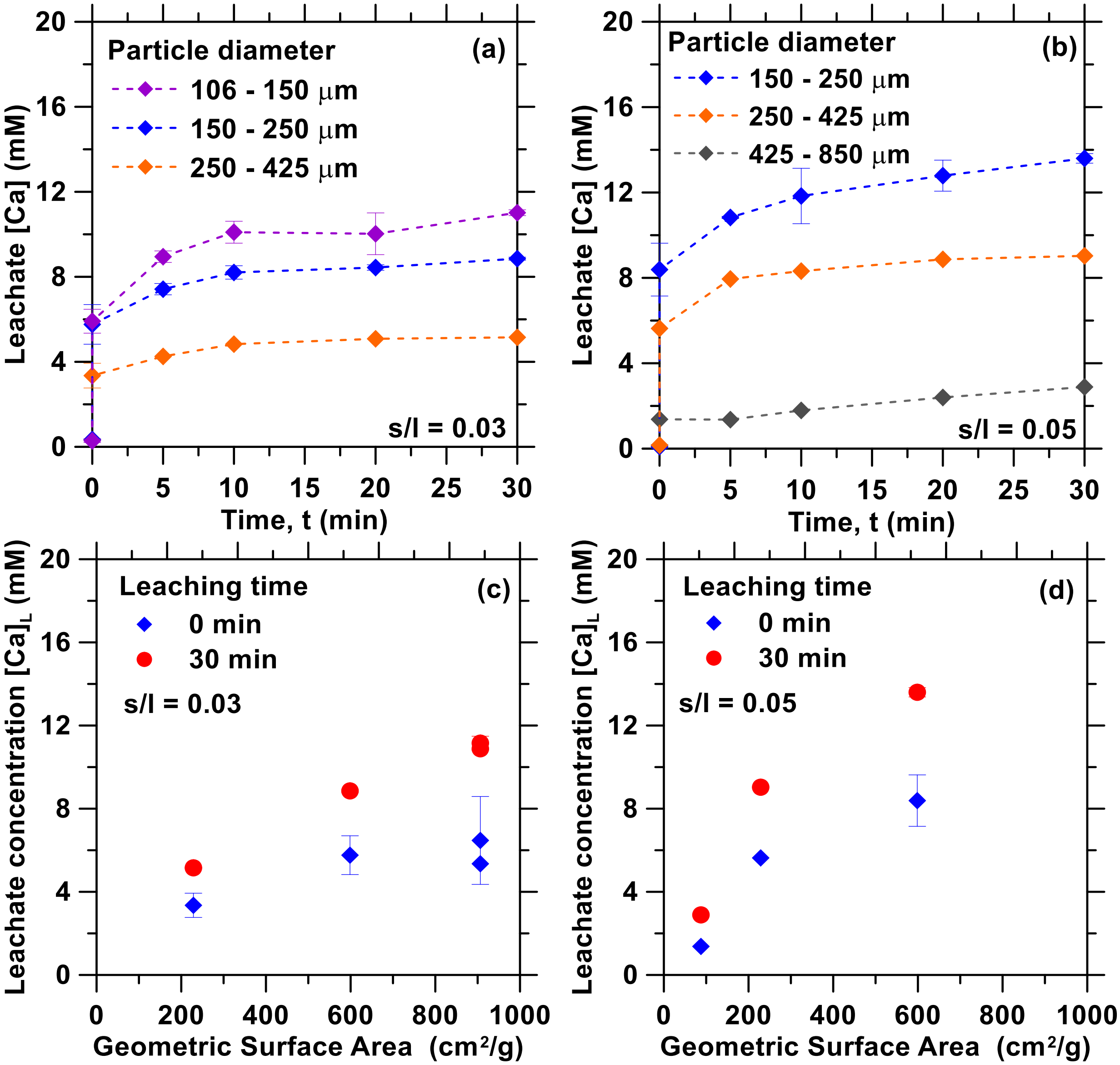

Figure 3.7. Leachate concentration $[Ca]_L$ as a function of time and particle size fraction for a solid to liquid ratio of (a) 0.03 and (b) 0.05. Initial ($t$ = 0 min) and final ($t$ = 30 min) leachate calcium concentration $[Ca]_L$ as a function of geometric surface area for a s/l ratio of (c) 0.03, and (d) 0.05.

### 3.4.3. Short-term stability of reverse osmosis concentration

The slag leachate solutions were concentrated continuously through the RO unit at a constant water recovery ratio of 0.52 to achieve similar concentration factors in all tests. Figure 3.8 shows the measured (a) feed temperature, (b) retentate pressure, (c) the total calcium concentrations in the feed $[Ca]_F$, retentate $[Ca]_R$ and permeate $[Ca]_P$ streams, as well as (d) membrane permeability $L_p$ and concentration factor ($CF = [Ca]_R/[Ca]_F$) as functions of time. Figure 3.8(a) indicates that the feed temperature ranged from 20 °C to 30 °C in all the experiments, indicating that the cooling system functioned properly. Figure 3.8(b) shows that the pressure drop ($P_F - P_R$) a cross the RO system between the feed and retentate was 15 kPa for pilot tests 1 and 2. Pilot test 3 operated at a slightly lower pressure drop of 12 kPa due to the lower feed flow rate. Figure 3.8(c) indicates that the feed concentration $[Ca]_F$ was constant around 10 ± 2 mM, as expected from the process design. The permeate concentration $[Ca]_P$ remained below 1 mM suggesting negligible membrane degradation. This was confirmed by the calcium rejection, which averaged 99.3%, 99.1% and 98.7% in pilot tests 1, 2, and 3, respectively.

Figure 3.8(d) indicates that the concentration factor $CF$ was around 2 for all tests performed and operated at the same water recovery ratio of 0.52. Additionally, it shows that membrane permeability [Equation (3.4)] decreased as a function of time, probably due to fouling or scaling. The decrease in membrane permeability $L_p$ was more prominent during the first 8 hours of continuous operation. This could be due to membrane compaction and system equilibration [140]. Additionally, the decrease in membrane permeability $L_p$ was larger at higher feed pressure namely 43% at 895 kPa in pilot test 2, compared to 10% at 482 kPa in pilot test 3. This observation can be attributed to the stronger convective force of the permeate passing through the membrane at larger pressures resulting in membrane fouling.[141] After each test, the membrane was cleaned with a diluted nitric acid solution (pH ~ 3) for 1 hour. The cleaning procedure improved the permeability, demonstrating that fouling can be reversed. Although the BW30-2540 membranes used in the pilot test are not designed to operate at pH larger than 11, the membranes remained stable while operating at a pH of 12.4 in the three tests performed. Nevertheless, a membrane durability study should be performed on different commercially available options before upscaling the technology to select the most suitable membrane.

Figures 3.8(c) and 3.8(d) show the calcium concentration $[Ca]_R$ and the concentration factor CF in the retentate as functions of time, respectively. Since $[Ca]_R$ was always above 15 mM, the solution entering the precipitation reactor was always supersaturated with $Ca(OH)_2$ when heated at 90 °C. On average, $[Ca]_R$ was 21.6, 20.7 and 22.2 mM for pilot tests 1, 2 and 3, respectively. Figures 3.8(c) and 3.8(d) indicate that the membranes tolerated calcium containing solutions concentrated above the saturation point of $Ca(OH)_2$ since the membrane permeability was very similar in all cases. Nevertheless, Figure 3.8(d) shows that a decrease in concentration factor coincided with an improvement in membrane permeability (for example at normalized t of 0.45 and 0.7 in pilot test 3), indicating that the permeability decline could be due to scale formation. However, it could be reversed when the retentate concentration $[Ca]_R$ decreased.

We hypothesized that supersaturation was possible without causing substantial membrane degradation because calcium concentration occurs instantaneously in the RO system at elevated flow rates. Whereas the kinetics of $Ca(OH)_2$ precipitation from a saturated solution at room temperature is very slow,[142] particularly at low supersaturation index (SI marginally larger than 0) when the nucleation rate is very small.[143] Since operating near portlandite saturation increased scaling on the RO membranes by the formation of $Ca(OH)_2$ or $CaCO_3$ precipitates, periodical flow reversal could improve the membrane's lifetime.[94] Additionally, anti-scaling coatings of polyethylene glycol (PEG) have been shown to reduce precipitate formation in BW30 Filmtec® membranes, also used in this study.[144]

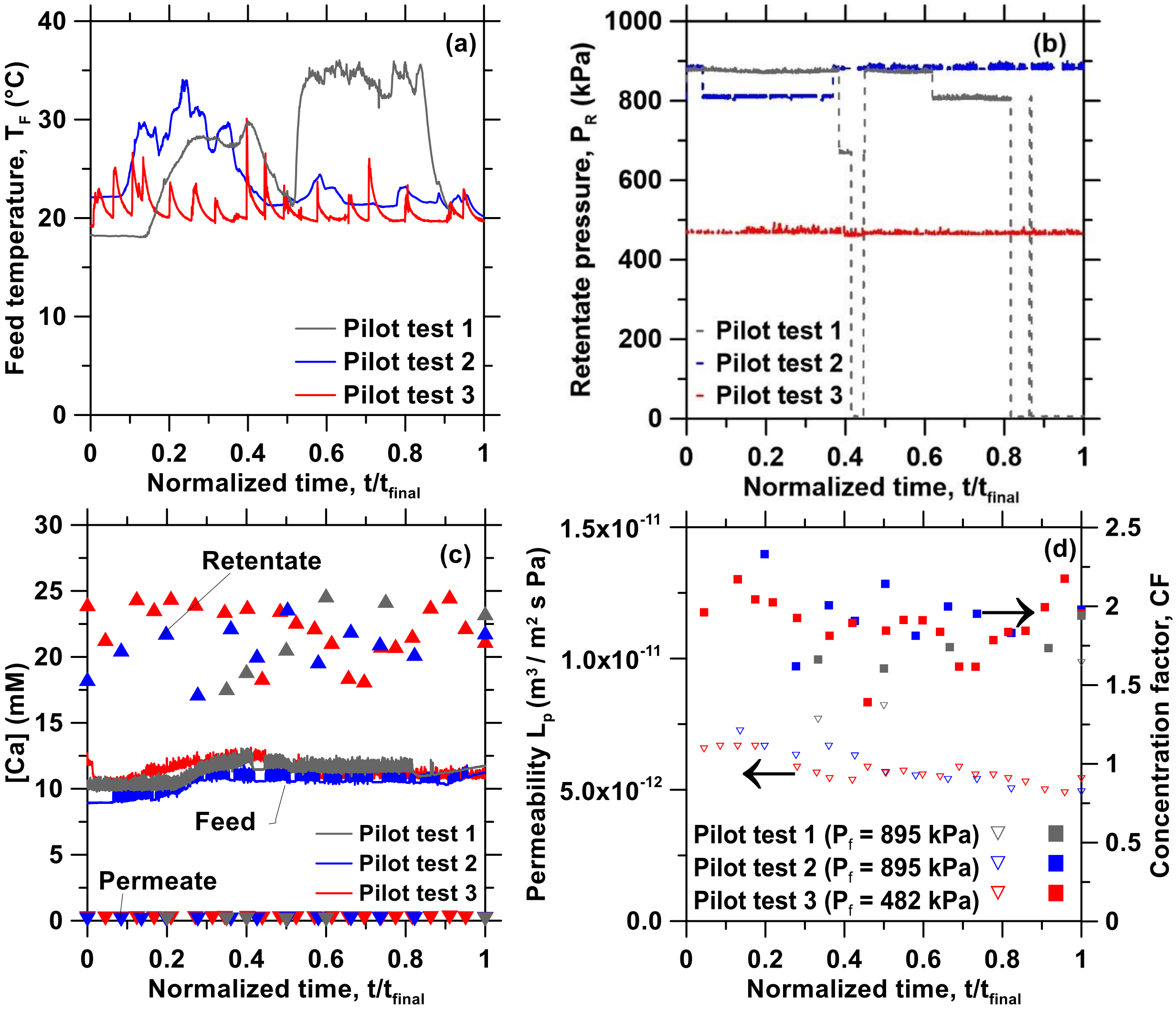

Figure 3.8. (a) Feed temperature, (b) Retentate pressure, (c) [Ca] concentration in the feed, retentate and permeate streams, and (d) Membrane permeability and concentration factor as functions of time.

### 3.4.4. Precipitation and $Ca(OH)_2$ characterization

Following the concentration step, $Ca(OH)_2$ precipitated in a continuously stirred reactor maintained at a constant temperature of 95 ± 5 °C. Figure 3.9 shows (a) the concentration of the recycled saturate stream $[Ca]_S$ – after filtering out the solid $Ca(OH)_2$ – as a function of time, (b) the XRD pattern, and (c) the TGA-DTG spectrum of the solid precipitates for all three pilot tests performed. Figure 3.9(a) shows that the saturate concentration was strongly dependent on the precipitation temperature. For example, at the beginning of pilot tests 1 and 2 when the precipitation temperature was below 90 °C, the calcium concentrations in solution $[Ca]_S$ increased, indicating a reduction in $Ca(OH)_2$ precipitation. On the other hand, the precipitation step was not affected by the retentate concentration $[Ca]_R$, which varied between around 20 mM ± 5 mM [Figure 3.8(c)]. Figure 3.9(b) establishes that portlandite was the only phase detected in the solids recovered from the pilot tests. Note that, while XRD was performed on carefully crushed powders to reduce the potential for preferential orientation of the crystals, the XRD pattern were acquired in static conditions (*i.e.*, using a non-rotating sample holder). Consequently, similar peak positions were observed but the peak intensities varied between pilot tests 1 and 2. The results were further confirmed by TGA-DTG, indicating that the water content represents 23 to 34 wt.% of the solids [Figure 9(c)]. The $Ca(OH)_2$ content, calculated from its decomposition around 500 °C,[77,102] made up 63 to 72 wt.% of the analyzed precipitates. An additional 2 wt.% of the precipitates decomposed around 700 °C, corresponding to the presence of $CaCO_3$, undetected by XRD due to its low content. The latter may have formed because of the presence of dissolved $CO_2$ in the feed water[78] and/or, the brief contact of the wet $Ca(OH)_2$ precipitate with air during drying when it carbonated when exposed to atmospheric $CO_2$.[103] The remaining 2 wt.% impurities appear to be composed of slag particulates.

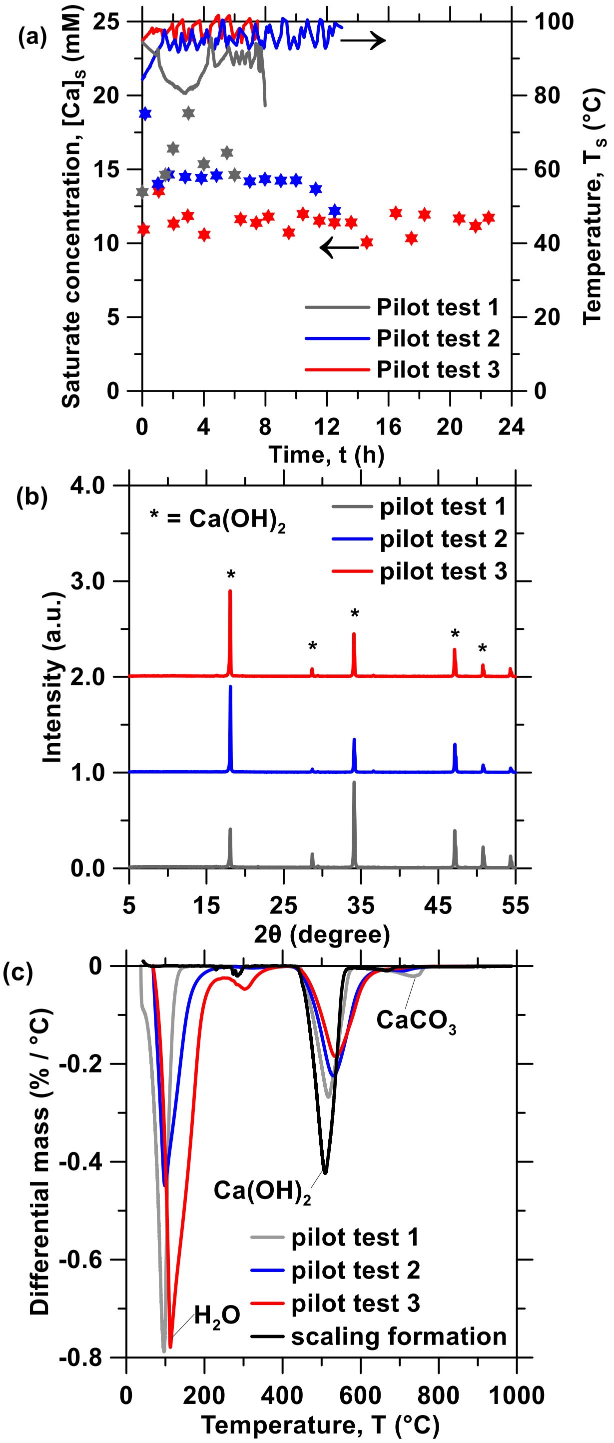

Figure 3.9. (a) [Ca] concentration in the saturate stream as a function of time, (b) XRD, and (c) TGA-DTG spectrum of the solid $Ca(OH)_2$ recovered from the pilot tests.

Table 3.2 summarizes the conditions as well as the amount and purity of the $Ca(OH)_2$ precipitated for each test performed. A $Ca(OH)_2$ production rate of 41 g/h (equivalent to 1 kg per day) was obtained in pilot test 1, demonstrating the technical feasibility of the process at the pilot scale. Additionally, the precipitation efficiency – comparing the theoretical versus the experimental production rate ($\dot{m}_{Ca(OH)_2}/\dot{m}_{Ca(OH)_2,e}$) – was highest during pilot test 3. This was coincident with a lower saturate calcium concentration $[Ca]_S$ measured during pilot test 3, indicating and improvement in the precipitation yield. The purity of all the $Ca(OH)_2$ samples solids exceeded 93.9%. Compared to our small-scale experiments[120] the amount of $CaCO_3$ impurities was drastically reduced because the volume of solution utilized was much larger than the surface of the solution in contact with air, demonstrating that the purity of $Ca(OH)_2$ obtained with this pilot system paralleled that of commercial-grade hydrated lime.[145]

Table 3.2. Operating conditions and experimental results of $Ca(OH)_2$ precipitation in the three pilot tests performed.

| | **Pilot test 1** | **Pilot test 2** | **Pilot test 3** |
|---|---|---|---|
| Average precipitation temperature $\boldsymbol{T_S}$ | 88 °C | 95 °C | 98 °C |
| Pilot test duration | 8 h | 12 h | 24 h |
| Average residence time $\boldsymbol{\tau}$ | 0.7 h | 1.0 h | 2.1 h |
| Collected mass of $Ca(OH)_2$ $\boldsymbol{m_{Ca(OH)_2,e}}$ | 328.3 g | 343.6 g | 452.7 g |
| Production rate $\boldsymbol{\dot{m}_{Ca(OH)_2,e}}$ | 41 g/h | 28.6 g/h | 18.8 g/h |
| Precipitation efficiency | 62.6% | 60.1% | 79.2% |
| Purity of $Ca(OH)_2$ | 93.9 % | 95.9 % | 96.9 % |
| Average saturate concentration $\boldsymbol{[Ca]_S}$ | 15.6 mM | 14.5 mM | 11.4 mM |
| $Ca(OH)_2$ solubility at $\boldsymbol{T_S}$* | 14.6 mM | 14.1 mM | 13.9 mM |

*Calculated with PHREEQC using the minteqV4 database.

Table 3.2 shows that the average saturate concentration $[Ca]_S$ measured experimentally was larger than the theoretical saturation concentration at precipitation temperature $T_S$ in pilot tests 1 and 2, as expected. However, in pilot test 3, the saturate concentration $[Ca]_S$ was lower than the theoretical solubility limit. Indeed, variations in $Ca(OH)_2$ solubility across different databases consulted may be as much as 5 mM.[65,130] In fact, $Ca(OH)_2$ solubility was found to be dependent on crystal size, the source material (e.g., $Ca(OH)_2$ obtained from the hydration of CaO produced from the calcination of calcium nitrate or marble) as well as the solid dosage.[67,146–148] In our case, differences in theoretical and experimental solubilities could be due to the presence of other cations in solution dissolved from slag which increase the pH of the solution[57] (compared to pure $Ca(OH)_2$ solutions) and shift the equilibrium towards the formation of solid $Ca(OH)_2$.[149] Moreover, the different saturate concentrations $[Ca]_S$ at similar temperature (pilot tests 2 and 3) could be due to the different residence times in the reactor, since it is well known that kinetics plays an important role in precipitation reactions.

Figure 3.10 shows SEM images of the crystals recovered from pilot (a) test 1, (b) test 2 ,(c) test 3 and (d) scaling formations on the surface of the heaters during pilot test 1. All the precipitated crystals had hexagonal structures typical of $Ca(OH)_2$.[103,104] Figure 3.10(c) indicates that pilot test 3 produced larger $Ca(OH)_2$ crystals, consistent with the larger residence time of ~ 2 hours in the precipitation reactor compared with ~ 1 hour in pilot tests 1 and 2.[143] The smaller crystal size obtained during pilot tests 1 and 2 can explain the lower calcium concentrations observed in solution, since smaller crystals ( $< 1$ μm) may have not been filtered out of the saturated solution and/or may have redissolved during the sampling procedure. Moreover, coarser crystals display lower solubility than smaller crystals.[146] Thus, larger residence time in the precipitation reactor is more desirable as it results in larger crystal size and precipitation yield.

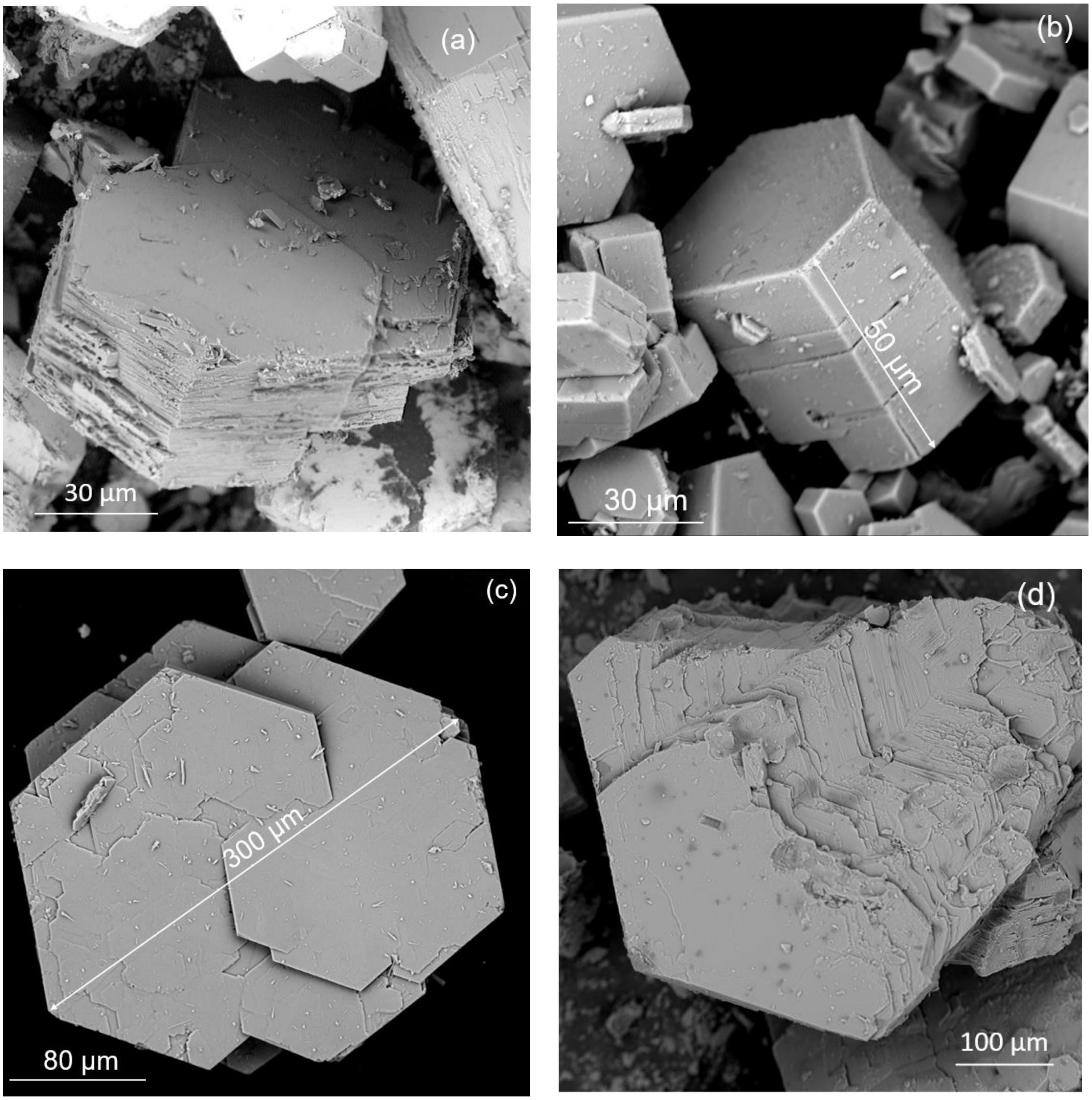

Figure 3.10. SEM images of representative crystals filtered after precipitation in pilot (a) test 1, (b) test 2, (c) test 3, and (d) scaling formations on the surface of the heaters from pilot test 1.

Moreover, a large fraction of the $Ca(OH)_2$ crystals formed through heterogeneous precipitation at the surface of the heaters where the temperature was the largest. The scaling layer of $Ca(OH)_2$ crystals was approximately 1 mm thick and brittle which facilitated its recovery. As opposed to the $Ca(OH)_2$ crystals obtained from the filters, the crystals extracted from the surface of the heaters were larger (100 to 200 µm) and more disordered [Figure 3.10(d)] and did not contain any water [Figure 3.9(c)]. Nevertheless, they showed the same degree of purity as the crystals obtained from homogeneous precipitation [Figure 3.9(c)]. Finally, $Ca(OH)_2$ had also a strong tendency to form scaling on the walls of the precipitation reactor and downstream pipes. However, the mass of such scaling formation was not quantified. Scaling could be avoided by using scraped surface crystallizers and by minimizing the distance between the precipitation reactor and the solid/liquid separation system.

### 3.4.5. Energy consumption

A detailed energy balance analysis of the process was performed using Equations (3.2)-(3.7) and (3.14). Table 3.3 summarizes the mass and energy balance of each pilot tests. It indicates that the specific pumping power consumption decreased when operating at lower pressures. The pumping electricity consumption calculated theoretically  was 0.798 kWh/kg $Ca(OH)_2$. Table 3.3 shows that the grinding and mixing energy was as important as the energy required for pumping. The mixing energy consumption could be minimized with a careful design of the leaching and precipitation reactors and particularly by optimizing reactor volume, impeller diameter and rotation frequency. Additionally, since $Ca(OH)_2$ crystals growth has been shown to be independent of the stirring rate,[147] the mixing energy could decrease substantially. Although the grinding energy per kg of slag was low (0.016 kWh/kg slag), the low efficiency of calcium extraction during leaching (below 10%) caused a large grinding specific energy consumption (2.1 – 2.4 kWh/kg $Ca(OH)_2$), underscoring the importance of improving the calcium extraction efficiency from slag to decrease the energy consumption and $CO_2$ footprint of the process. Finally, the heating energy consumption was two orders of magnitude larger than the electricity consumption, as predicted by the model (Figure 3.6). Nevertheless, at least 50% of this energy could be recovered using a heat exchanger to preheat the retentate solution entering the precipitation reactor based on process integration principles.[150,151]

Table 3.3. Energy and specific energy consumption of the unit operations of the process for the pilot tests performed

| | **Pilot test 1 (8 h)** | | **Pilot test 2 (12 h)** | | **Pilot test 3 (24 h)** | |
|---|---|---|---|---|---|---|
| | **Energy (kWh)** | **SEC (kWh / kg $Ca(OH)_2$)** | **Energy (kWh)** | **SEC (kWh / kg $Ca(OH)_2$)** | **Energy (kWh)** | **SEC (kWh / kg $Ca(OH)_2$)** |
| Grinding | 0.787 | 2.397 | 0.828 | 2.410 | 0.975 | 2.154 |
| Mixing | 0.759 | 2.312 | 1.090 | 3.172 | 1.940 | 4.280 |
| Heating | 87.130 | 265.397 | 89.731 | 261.149 | 85.829 | 189.590 |
| RO pump | 0.631 | 1.920 | 0.690 | 2.008 | 0.362 | 0.798 |

## 3.5. Conclusion

This study demonstrated the design and continuous operation of a pilot system to produce $Ca(OH)_2$ from industrial alkaline wastes as a feedstock. The process encompasses an integrated set of three unit operations including leaching, RO concentration, and temperature-swing precipitation. Additionally, the water was fully recirculated, making the water consumption of the process virtually zero. Decreasing the slag particle size during leaching improved the calcium concentration of the leachate, thereby increasing the calcium extraction efficiency from slag without the need to increase slag consumption. We also demonstrated the stability and reliability of the continuous process by completing three continuous tests of 8, 12, and 24 hours using the same RO membranes. Fouling and/or scaling was reversed with standard membrane cleaning procedures. The low energy demand, and the reversibility of fouling and scaling demonstrated that RO was a robust technology to concentrate the slag leachates and indicated good upscaling technology potential. Finally, larger residence times in the precipitation reactor increased the crystal particle size and decreased the calcium concentration of the saturated solution $[Ca]_s$, indicating an increase in the quantity of $Ca(OH)_2$ precipitated per unit volume of solution. An equivalent production rate of 1 kg per day was demonstrated during pilot test 1 whereas a continuous 24-hour operation was demonstrated during pilot test 3. In all cases, the purity of the $Ca(OH)_2$ exceeded 94%. The experimental measurements agreed with the process flow model and thermodynamic calculations. Overall, the results substantiated the feasibility of the continuous process and the full recirculation of water on a pilot scale and enabled a detailed accounting of the energy consumption of the process. The outcomes provided insights on process limitations and specific design requirements for the unit operations and on important steps towards upscaling the technology to produce $Ca(OH)_2$ from industrial wastes at low temperatures.

# CHAPTER 4

## Up-Scale Potential: Geospatial, Financial and $CO_2$ Footprint Analysis

This study evaluates the techno-economic feasibility and the $CO_2$ footprint of a novel process integration scheme with thermal power plants to produce portlandite from alkaline industrial wastes via leaching, reverse osmosis concentration, and low-temperature aqueous precipitation. We evaluated such process installed in the U.S. for an optimized base case scenario minimizing electricity consumption. The conditions for feasibility were evaluated considering the source and geospatial availability of electricity (*e.g.*, coal, natural gas, solar thermal), waste heat, and slag. The production cost of upcycled portlandite for the base case scenario was two to three times higher than the wholesale price of traditional portlandite. The main driver of the operating cost was the RO step, due to electricity and membrane replacement costs. Moreover, the sensitivity analysis showed that a competitive operating cost could be achieved by increasing membrane lifetime and decreasing the electricity consumption. The upcycled portlandite featured a $CO_2$ footprint 40% to 80% lower than the benchmark product when the electricity is sourced from natural gas and wind power, respectively. Finally, a geospatial analysis elucidated the areas in the U.S. with potential to implement an industrial-scale facility due to the proximity between feedstocks and waste heat sources.

### 4.1. Background

To reduce the $CO_2$ footprint of $Ca(OH)_2$, we have previously demonstrated a low-temperature (≤ 100 °C) calcination-free route to produce $Ca(OH)_2$ from steel slag in the laboratory- and pilot-scale.[120,152] Our pilot scale study demonstrated the continuous production of high purity (>95%)

$Ca(OH)_2$, and elucidated strategies to improve the efficiency and decrease the electricity consumption of the process such as decreasing the slag particle size for leaching and increasing the precipitation temperature, respectively. This processing route is in line with the principles of circular economy because it enhances resource recovery from industrial byproducts[58] and it has the potential to reduce not only the $CO_2$ footprint of industrial lime production,[153] but also the environmental impacts of quarrying limestone,[9] and landfilling slag. The solution could be implemented in industrial facilities with large availability of waste heat, such as thermal power plants or steel production plants. Nevertheless, the electricity consumption, the availability of waste heat and slag, and the proximity between these two resources could be a barrier to upscaling this process. Thus, this study explores the upscale potential of low-temperature calcination-free $Ca(OH)_2$ production from steel slag using the method previously described and compares it to traditional $Ca(OH)_2$ production.

## 4.2. Methodology

### 4.2.1. Process description and modelling

The conceptual design of the proposed $Ca(OH)_2$ production system was modeled using Aspen Plus V10. The operating parameters of the simulation were based on previous laboratory- and pilot-scale simulations and experiments Figure 4.1 shows the process flow diagram to model the steady state production of $Ca(OH)_2$. A base case scenario with a production capacity of 52 tons of $Ca(OH)_2$ per day was selected based on the output of a conventional lime production plant.[153]

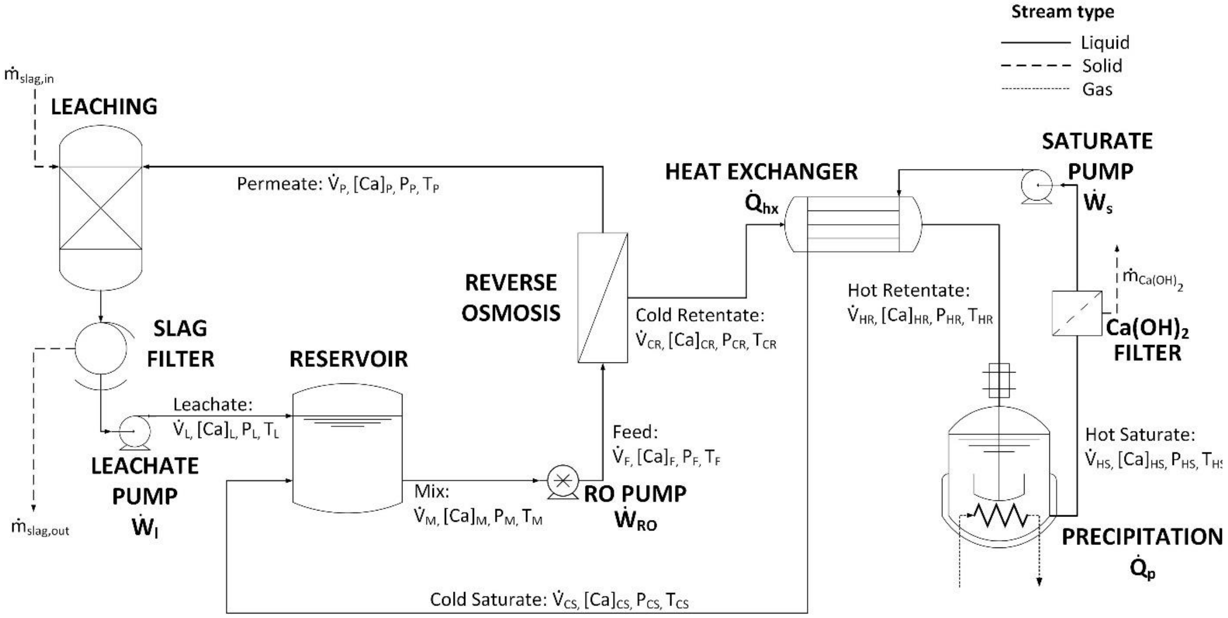

Figure 4.1. System boundaries of the proposed $Ca(OH)_2$ production

### *Leaching*

The process starts with leaching slag with deionized water in the leaching reactor. The water required for leaching was assumed to be sourced from recirculated permeate solution, as demonstrated experimentally on previous pilot-scale experiments. The leaching process was not simulated based on phenomenological equations because the rate and magnitude of calcium release from slag is influenced by many factors such as the type of slag, the particle size, the solid to liquid (s/l) mass fraction, and the type of leaching reactor (e.g., stirred tanks, fixed bed). [56,57,88] Instead, the s/l mass fraction and the leachate concentration $[Ca]_L$ in the reactor were imposed to 0.01 and 8.1 mmol/L (mM), respectively, based on leaching experiments performed with basic oxygen furnace (BOF) slag on the laboratory scale (Figure C1). Slag was simulated as $Ca_2SiO_4$ – one of the most abundant mineral phases of slag[154] – undergoing dissolution in the leaching reactor ($Ca_2SiO_4 + 2H_2O \rightarrow 2Ca^{2+} + 4OH^- + SiO_2$) assuming a $Ca_2SiO_4$ fractional conversion (X = moles reacted / moles fed) of 6.5%, consistent with the typical conversion on laboratory-scale batch leaching experiments.[120] The resulting alkaline leachate is fully separated from the unreacted slag using the slag filter. The energy required for the solid-liquid separation was calculated as the energy required to pump the leachate through the filter using the leachate pump $\dot{W}_L$. In general, the pumping power was calculated as

$$\dot{W}_i = \frac{\dot{V}_j (\Delta P)_i}{\eta_p} \tag{4.1}$$

Where $\eta_p = 0.8$ is the hydraulic pump efficiency. $\dot{V}_j$ is the solution flow rate (in m$^3$/s) of the stream $j$ entering the pump, with $j = L, M, S$ indicating leachate, mix, and saturate streams, respectively. $(\Delta P)_i$ indicates the pressure increase (in Pa) delivered by pump $i$, with $i = l, RO, s$ indicating leachate, RO, and saturate pumps, respectively. The pressure increase delivered by the leachate pump was assumed to be $(\Delta P)_l = 101{,}325\ Pa$

***Reservoir***

The filtered leachate enters the reservoir where it is mixed with the cold saturate stream. The latter is recirculated from the precipitation step to improve the efficiency of the process. The calcium concentration, volumetric flow rate and temperature of the mix stream exiting the reservoir were calculated as

$$\dot{V}_M = \dot{V}_L + \dot{V}_{CS} \tag{4.2}$$

$$\dot{V}_M\, [Ca]_M = \dot{V}_L [Ca]_L + \dot{V}_{CS} [Ca]_{CS} \tag{4.3}$$

$$T_M = \frac{\dot{V}_L T_L + \dot{V}_{CS} T_{CS}}{\dot{V}_L + \dot{V}_{CS}} \tag{4.4}$$

Where $\dot{V}, [Ca],$ and $T$ stand for volumetric flow rate, calcium concentration (in mol/m$^3$), and temperature (in °C), respectively. The subscript *CS* corresponds to the cold saturate stream.

***Reverse Osmosis (RO) concentration***

To drive RO concentration, the mix stream exiting the reservoir is pressurized using the RO pump from atmospheric pressure $P_M = 101{,}325\ Pa$ to a feed pressure of $P_F = 900{,}000\ Pa$. The pumping power was calculated using Equation 4.1 with $(\Delta P)_{RO} = 798{,}675\ Pa$. The selection of the feed pressure was based on a parametric optimization to minimize membrane replacement and electricity costs (Appendix C: RO pressure optimization). To model the RO membrane separation step, a mass balance for the solution and for calcium was performed according to

$$\dot{V}_F = \dot{V}_P + \dot{V}_{CR} \tag{4.5}$$

$$\dot{V}_F\,[Ca]_F = \dot{V}_P[Ca]_P + \dot{V}_{CR}[Ca]_{CR} \tag{4.6}$$

where the subscripts $F, P,$ and $CR$ stand for feed, permeate, and cold retentate streams, respectively. The volumetric flow rate of the permeate stream was calculated as

$$\dot{V}_P = A_{RO}L_p(\Delta P_{mem} - \Delta\pi) \tag{4.7}$$

where $A_{RO}$ is the RO membrane area, $L_p = 8.64 * 10^{-12}\ m^3/(s\ m^2\ Pa)$ is the membrane permeability estimated from experimental data[120] and reported in literature.[132–134] $\Delta P_{mem}$ is the transmembrane pressure difference defined as the difference between the feed pressure $P_F$ and the permeate pressure $P_P = 101{,}325\ Pa$, i.e., $\Delta P_{mem} = P_F - P_P$. The osmotic pressure difference between the feed and the permeate solutions [131] was calculated as [135]

$$\Delta\pi = R_U T_F[([Ca]_F + [OH^-]_F) - ([Ca]_P + [OH^-]_P)] \tag{4.8}$$

where $R_U = 8.314\, J\, mol^{-1} K^{-1}$ is the universal gas constant and $T_F$ is the feed temperature. Since the heat generated by the RO pump is negligible, the temperature of the feed is equal to the mix stream, i.e., $T_F$=$T_M$. The concentration of $[OH^-]$ in all the streams was calculated according to the electroneutrality principle as $2[OH^-] = [Ca]$. The permeate calcium concentration $[Ca]_P$ was calculated based on the membrane rejection coefficient $R = 0.99$ according to membrane manufacturer data so that

$$[Ca]_P = [Ca]_F(1 - R) \tag{4.9}$$

***Retentate preheating and saturate recirculation***

Prior to precipitation, the cold retentate – concentrated with RO to the saturation point of $Ca(OH)_2$ at room temperature – is preheated using the hot saturate stream exiting the precipitation reactor through the heat exchanger. The heat absorbed by the cold retentate stream in the heat exchanger $\dot{Q}_{hx}$ was calculated using the general energy balance equation[115]

$$\dot{Q}_i = \dot{V}_j \rho c_p (\Delta T)_j \tag{4.10}$$

Where $\dot{V}_j$ is the volumetric flow rate of the retentate stream exiting RO, $\rho = 1000\, kg/m^3$ is the density and $c_p = 4184\, J\, kg^{-1} K^{-1}$ is the heat capacity of the solution. $(\Delta T)_j = T_{j,out} - T_{j,in}$ indicates the temperature difference across the heat exchanger between the outlet and inlet streams. In the case of the recycle heat exchanger $T_{j,out}$ and $T_{j,in}$ correspond to the temperature of the hot retentate $T_{HR}$ and the cold retentate $T_{CR}$, respectively. Similarly. The heat delivered by the hot saturate stream was calculated with equation 4.10 with $T_{j,out}$ and $T_{j,in}$ equal to the temperature of the cold saturate $T_{CS}$ and hot saturate $T_{HS}$, respectively. The temperature of the cold saturate $T_{CS}$ was imposed at 30 °C to eliminate further cooling electricity requirements in the reservoir. The recycle heat exchanger surface area was estimated as

$$A_{hx} = \frac{\dot{Q}_{hx}}{U\ LMTD} \tag{4.11}$$

Where $U = 849\ W/m^2K$ is the overall heat transfer coefficient,[115] $A_{hx}$ is the area of the countercurrent heat exchanger and $LMTD$ is the log mean temperature difference calculated as[115]

$$LMTD = \frac{(T_{CS} - T_{CR}) - (T_{HS} - T_{HR})}{\ln[(T_{CS} - T_{CR})/(T_{HS} - T_{HR})]} \tag{4.12}$$

*Precipitation:* The hot retentate stream enters a continuously stirred precipitation reactor. Inside this unit, the solution was assumed to be in equilibrium with portlandite, i.e., $Ca^{2+} + 2OH^{-} \leftrightarrow Ca(OH)_{2\,(s)}$. The concentration of the hot saturate stream $[Ca]_{HS}$ exiting the precipitation reactor was calculated based on the solubility of portlandite as a function of temperature $[Ca]_{hs} = f(T_{hs})$ illustrated in Figure 3.4. The mass flow rate of solid $Ca(OH)_2$ exiting the crystallizer $\dot{m}_{Ca(OH)_2}$ was calculated as

$$\dot{m}_{Ca(OH)_2} = \dot{V}_{HS}\, M_{Ca(OH)_2}([Ca]_{CR} - [Ca]_{HS}) \tag{4.13}$$

where $\dot{V}_{hs}$ is the hot saturate volumetric flow rate, $M_{Ca(OH)_2}$is the molar mass of $Ca(OH)_2$ (in kg/mol) and $[Ca]_{CR}$ and $[Ca]_{HS}$ are the calcium concentration of the cold retentate and hot saturate streams, respectively. Additionally, since the mass of $Ca(OH)_2$ precipitated is negligible compared to the volume of liquid, the retentate and saturate flow rates were assumed to be equivalent so that $\dot{V}_{HR} = \dot{V}_{HS}$. The heat required for precipitation is assumed to come from exit flue gas from a coal fired power plant. The thermal power (in W) required for $Ca(OH)_2$ precipitation $\dot{Q}_p$ was calculated with equation 4.10 with $T_{j,out}$ and $T_{j,in}$ equal to the temperature of the hot saturate $T_{HS}$ and hot retentate $T_{HR}$, respectively. The temperature of the hot saturate $T_{HS}$ was imposed at 83 °C. After filtering out the precipitated $Ca(OH)_2$, the hot saturated solution is recirculated using the saturate pump to the heat exchanger and thereafter to the reservoir, thereby completing the closed-loop process.

### 4.2.2. Solution method

Figure 4.2 shows a block diagram of the solution method to calculate the steady-state pumping power consumption and the precipitation heating requirement to produce 52 tons per day of $Ca(OH)_2$ with the proposed process.

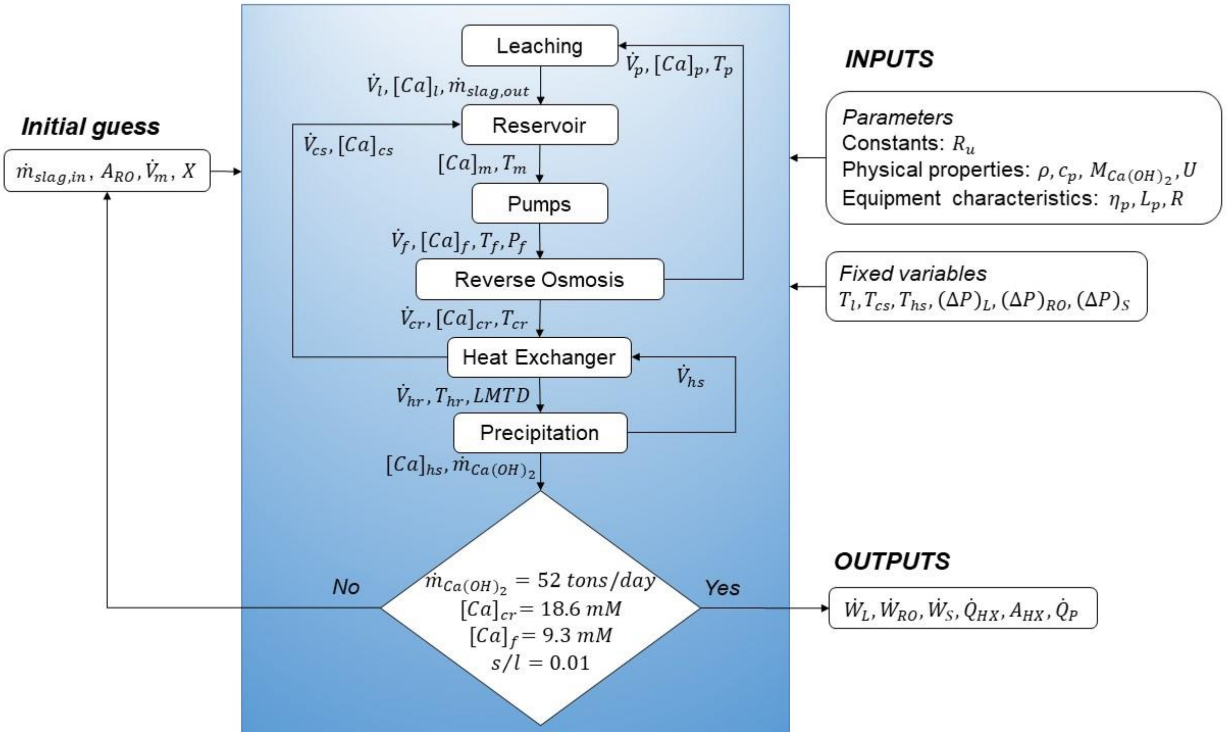

Figure 4.2. Block diagram of the solution method to predict the heat and power consumption of the $Ca(OH)_2$ production process

The variables used to initialize the solution were the inlet slag mass flow rate $\dot{m}_{slag,in}$, the leaching reaction conversion $X$, the RO membrane area $A_{RO}$, and the volumetric flow rate of the mix stream $\dot{V}_M$. After initialization, the software solves the equations simultaneously until converging to a solution that satisfies all the equations. The solution of the model was verified to satisfy the following constraints: (i) a $Ca(OH)_2$ production rate $\dot{m}_{Ca(OH)_2}$ of 52 tons per day, (ii) a cold retentate concentration $[Ca]_{CR}$ of 18.6 mM, (iii) a feed concentration $[Ca]_F$ of 9.3 mM, and (iv) a s/l mass fraction in the leaching reactor of 0.01. The initial guesses were modified iteratively until the solution of the model satisfied all the constraints.

### 4.2.3. Techno-economic analysis

***Capital cost (CapEx) estimation***

To estimate the cost of the RO step, the RO membrane area was recalculated using WAVE®, a specialized software provided by the membrane manufacturer. The simulation assumed single stage concentration using BW30-4040 spiral wound elements. The calcium concentrations and flow rates of the feed, permeate and retentate streams obtained from the Aspen Plus simulations were reproduced in WAVE® to obtain a better estimation of the membrane area considering design constrains of the spiral wound elements such as minimum and maximum permeate and retentate flow rates and maximum pressure drop per element.[155] The membrane area required for the plant was estimated to be 169,232 $m^2$, and the membrane cost was assumed to be \$19/$m^2$.[156–158] The total installed cost of the RO unit – including pressure vessels, pipes, support frame, etc – was estimated from a reference large scale RO plant[70] assuming that the cost fraction of other items compared to the membrane cost remains constant regardless of the scale of the plant (Appendix C, Table C1).

The capital costs of the leaching and precipitation reactors, the filters. the heat exchanger and the pumps were estimated using Aspen Plus capital cost estimator (ACCE ™). The software estimates the dimensions of each unit operation and calculates equipment and installation costs encompassing equipment setting, instrumentation, civil and steel designs, electrical, insulation and paint. Since the price basis of the software is 2016, the price was escalated assuming an average inflation of 2% per year up to 2021.[159] The land cost was not considered because this process would be retrofitted to an existing thermal power plant. Project contingency costs were not considered. Additionally, no discount rates, tax rates or $CO_2$ credits are considered in this analysis. The lifetime of the plant $n$ was assumed to be 20 years. The distributed capital cost was calculated as the total capital expenses $CapEx$, divided by the plant lifetime $n$ and the $Ca(OH)_2$ production rate $\dot{m}_{Ca(OH)_2}$ (in tons/year).

$$distributed\ CapEx = \frac{CapEx}{n\ \dot{m}_{Ca(OH)_2}} \tag{4.14}$$

***Operating cost (OpEx) estimation***

The main operating costs considered were the cost of electricity, slag, slag transport, membrane replacement and labor. The cost of electricity was calculated based on the pumping and slag grinding power requirements, assuming the cost electricity is \$0.07/kWh.[160] The cost of slag was assumed to be \$1 per ton based on the price of the provider for BOF slag (TMS International). The cost of slag transport was assumed to be \$ 0.05 / ton-mile.[161] The base case scenario assumes a replacement frequency of 2 years because the process operates at high pH (> 12), and the long-term stability of the membranes due to membrane fouling, scaling and degradation is unclear. However, RO membranes can last up to 5 years under normal operating conditions.[162] Labor costs were assumed to be 4% of the $CapEx$.[69,70] All the operating costs were divided by the $Ca(OH)_2$ production rate assuming a plant capacity factor of 80%. The cost of waste heat and water were not considered because the former is an industry by-product, and the latter can be fully recirculated inside the process as demonstrated in the pilot-scale experiments.

### 4.2.4. $CO_2$ footprint

The goal of the $CO_2$ footprint analysis was to evaluate material and process aspects of the *alternative portlandite* as compared to *traditional portlandite* production to compare their environmental impact. The $CO_2$ footprint was modeled using openLCA software,[163] with the modified National Energy Technology Laboratory (NETL) CO2U LCI database[164] supplemented with the National Renewable Energy Laboratory (NREL) U.S. Life Cycle Inventory (USLCI) Database.[165] The production, manufacture, and construction of manufacturing capital goods, capital infrastructure production equipment and vehicles, and personnel-related activities are excluded from the present analysis. Figure 4.4 shows the system boundary considered for the cradle-to-gate $CO_2$ footprint analysis of (a) the alternative and (b) the traditional portlandite production processes and describes key material and energy inputs and reference flows.

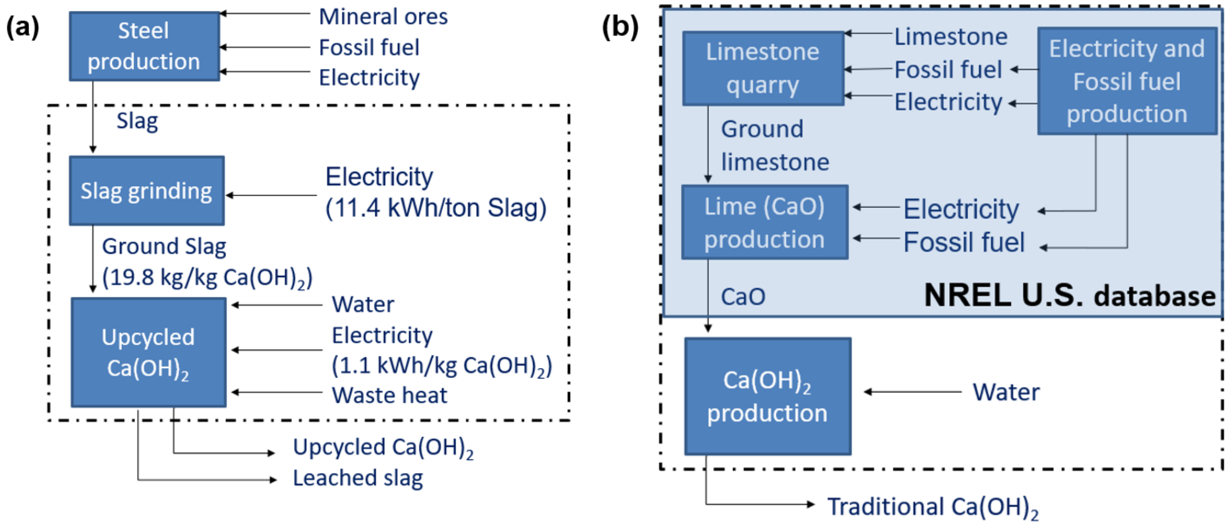

Figure 4.3. Simplified system boundaries for cradle-to-gate LCA of (a) Alternative portlandite production and (b) Traditional portlandite production.

***Alternative portlandite production***

The $CO_2$ footprint of alternative portlandite production was calculated on the basis of 1 ton of $Ca(OH)_2$ produced via slag dissolution, RO concentration, and aqueous precipitation at a temperature of 83 °C. The electricity and material inputs were calculated from the base case scenario simulations. The specific energy consumption of grinding slag was calculated as [127]

$$w_{g,slag}\left(\frac{kWh}{ton\ slag}\right) = W_i\left(\frac{10}{\sqrt{d}} - \frac{10}{\sqrt{d_i}}\right) \tag{4.15}$$

where $W_i = 18.3\ kWh/ton\ slag$ is the Bond work index of slag,[128] $d_i = 9500\ \mu m$ is the initial particle size and $d = 100\ \mu m$ is the final particle size. The environmental impact of slag production was not considered because this material is a by-product from steel production. Under the same argument, no environmental impact was associated to the waste heat required for $Ca(OH)_2$ precipitation. Three different sources of electricity were considered: (I) super critical coal power, (II) natural gas power and (III) solar thermal power.

***Traditional portlandite production***

The $CO_2$ footprint of traditional portlandite production was calculated on the basis of 1 ton of $Ca(OH)_2$ produced via limestone quarrying, calcination, and hydration. The electricity and fossil fuel consumption for limestone quarrying and calcination were taken from the NREL USLCI database.[165] It was assumed that limestone is quarried from open pits by blasting, followed by mechanical crushing and screening. Thereafter, limestone calcination in a rotary kiln – requiring electricity and fossil fuel – produces CaO. Finally, CaO hydration produces $Ca(OH)_2$, but no energy consumption was associated with this hydration step.

### 4.2.5. Slag and waste heat availability in the U.S.

***Estimation of slag and CaO availability from steel production***

The amount of slag produced in the U.S. was estimated from the $CO_2$ emissions of steel production facilities assuming a ratio of $CO_2$ emitted to steel produced of 0.64,[166] and a ratio of slag to steel produced of 0.12.[45] The $CO_2$ emissions from steel plants was obtained from the NATCARB database considering only the Iron and Steel production category.[167] The content of CaO in slag was assumed to be 40%.

***Estimation of waste heat from thermal power plants***

Plant-level data for electricity generation, fuel consumption and cycle type reported in by the Energy Information Administration (EIA) form EIA-923 was used to estimate waste heat generation. The form reports the annual electricity generation $W_{elec}$ and the total heat input from the utilized fuel $Q_{fuel}$. The types of fuel considered in this manuscript were coal, nuclear and natural gas, operating with steam or gas turbines. Equations 4.16 and 4.17 were used to calculate the cycle efficiency and the waste heat for each plant.[116]

$$\eta_{cycle} = \frac{W_{elec}/\eta_{turbine}}{Q_{fuel}} \tag{4.16}$$

$$Q_{waste} = Q_{fuel} - \frac{W_{elec}}{\eta_{conv}} \tag{4.17}$$

Where $\eta_{turbine}$ is the turbine efficiency taken as 86% and 93% for steam and gas turbines, respectively.[116] To validate the results, the cycle efficiency was compared to typical efficiencies of the Brayton and Rankine cycles.

***Relative distance between thermal power plants and slag facilities***

The location of slag facilities was obtained from the National Slag association.[168] The location of the thermal power plants was obtained from form EIA-860. The distance from each power plant to every slag facility in the same state was calculated as [169]

$$D = \sqrt{(K_1\,\Delta\varphi)^2 + (K_2\,\Delta\lambda)^2} \tag{4.18}$$

Where $\Delta\varphi$ is the latitude difference and $\Delta\lambda$ is the longitude difference between the two points. $K_1$ and $K_2$ are constants.[169] A MATLAB script was used to identify the closest slag facility to each power plant. The location data obtained was plotted and visually categorized using QGIS software.

## 4.3. Results and discussion

### 4.3.1. Base case scenario

Table 4.1 summarizes the main results of electricity and heat consumption for the base case scenario. The total electricity consumption of the process was 1,094.7 kWh / ton $Ca(OH)_2$ and it was dominated by the RO pump. The total heat required for precipitation ($\dot{Q}_p + \dot{Q}_{hx}$) was 113,724 kWh / ton $Ca(OH)_2$, two orders of magnitude larger than total electricity consumption. However, at steady state 90% of this heat was supplied through heat recovery on the heat exchanger. Hence, for the production rate considered in this study, the heating rate input required at steady state to produce $Ca(OH)_2$ is 25.79 MW, which is compatible with the residual heat flux found in median-size thermal power plants in the U.S.[116] The results demonstrate that the heat exchanger is essential for the large-scale technical feasibility of process because: first, it reduces by an order of magnitude the thermal plant waste heat input required at steady state by preheating the cold retentate. And it cools down the hot saturate stream down to 30 °C eliminating the need to use electricity for cooling, which would otherwise make the operating costs of the process unfeasibly large.

Table 4.1. Summary of the main results of the Aspen plus simulation of the base case scenario to produce 52 tons of $Ca(OH)_2$ per day.

| **Base case scenario results** | |
|---|---|
| $Ca(OH)_2$ production rate $\dot{m}_{Ca(OH)_2}$ from simulation | 52.4 tons $Ca(OH)_2$ / day |
| $Ca(OH)_2$ production rate $\dot{m}_{Ca(OH)_2}$ (considering capacity factor) | 41.92 tons $Ca(OH)_2$ / day |
| RO pump energy consumption $\dot{w}_{RO}$ | 971.5 kWh / ton $Ca(OH)_2$ |
| RO membrane area $A_{RO}$ | 169,232 $m^2$ |
| Low-pressure pumps energy consumption $\dot{W}_L + \dot{W}_S$ | 123.2 kWh / ton $Ca(OH)_2$ |
| Slag consumption $\dot{m}_{slag,in}$ | 19.8 tons slag per ton $Ca(OH)_2$ |
| Grinding energy consumption $w_{g,slag}$ | 0.25 kWh / ton $Ca(OH)_2$ |
| Precipitation heat $\dot{q}_p$ | 11,818 kWh / ton $Ca(OH)_2$ |
| Heat recovery from heat exchanger $\dot{q}_{hx}$ | 101,906 kWh / ton $Ca(OH)_2$ |
| Heat exchanger area $A_{hx}$ | 52,321 $m^2$ |
| Feed flow rate | 3499.7 $m^3$ / ton $Ca(OH)_2$ |

### 4.3.2. Techno-economic analysis

The total capital expenditures of $Ca(OH)_2$ production were estimated to be $38,063,015. Figure 4.4 shows the breakdown of (a) the capital and (b) the fully loaded $Ca(OH)_2$ production costs at the scale considered in the base case scenario. Figure 4.4(a) shows that the RO unit and the heat exchanger account for 87% of the total upfront investment due to the large membrane and heat exchange areas required for the concentration and heat recovery processes, respectively. Based on the membrane area requirement (Table 4.1) the cost of membranes was estimated as $3,230,406. Thus, capital expenditures for the fully installed RO unit were estimated to be $16,475,069, corresponding to 5.1 times the cost of membranes. The assumptions considered to calculate the capital cost of the RO unit – including membranes, pressure vessels and piping – is presented in Appendix C.

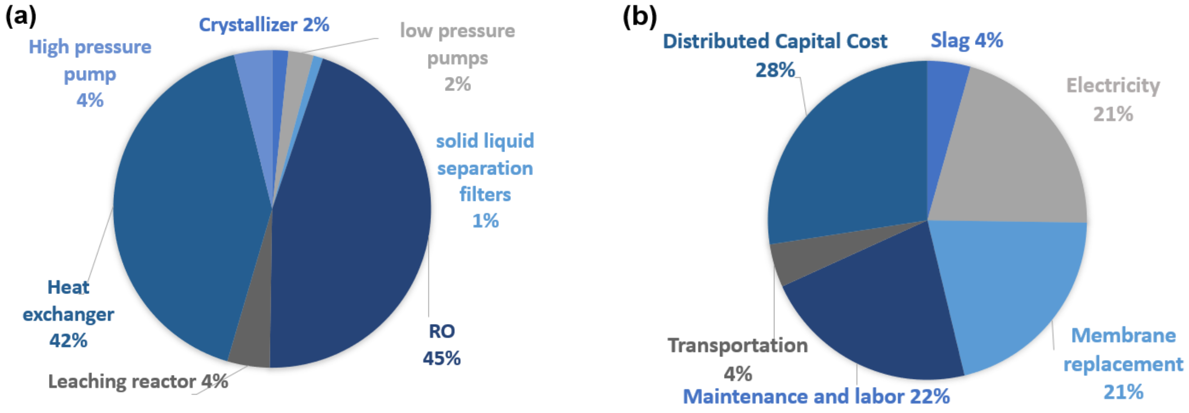

Figure 4.4. Break down of (a) Capital expenses and (b) Fully loaded production cost of a commercial-scale $Ca(OH)_2$ production plant.

Figure 4.4(b) shows that slag cost and transportation are the least expensive operating costs. Moreover, it indicates that the main driver of the operating cost was the RO step, due to electricity and membrane replacement costs.

Table 4.2. Operating cost break down of the base case scenario

| Cost variables | Assumption | Cost ($/ton $Ca(OH)_2$) |
|---|---|---|
| **Direct labor** | 4 % Of capital cost per year | 99.51 |
| **Slag cost** | $1 per ton of slag | 19.82 |
| **Electricity** | $0.07 per kWh | 67.93 (RO pump) |
| | | 8.62 (Low pressure pumps) |
| | | 18.04 (Grinding) |
| **Membrane replacement** | Every 2 years | 95.38 |
| **Slag transport distance** | 20 miles ($0.051 per ton-mile) | 19.82 |
| ***OpEx*** | | 329.12 |
| ***Distributed CapEx*** | 20-year plant lifetime | 124.40 |
| ***Fully loaded OpEx*** | | 453.52 |

Table 4.2. shows the operating cost break down of the base case scenario. The total operating expenses were calculated to be $329 per ton $Ca(OH)_2$. The fully loaded production cost – also known as the break-even point – calculated as the sum of *OpEx* plus *Distributed CapEx* for a plant

producing 52 tons of $Ca(OH)_2$ per day was \$453.5 per ton $Ca(OH)_2$. The distributed capital cost calculated with Eq. 4.14 was \$124.4 per ton $Ca(OH)_2$. Nevertheless, a 30-year plant lifetime – also considered standard in project evaluation – would reduce the distributed capital expenses to \$83/ton $Ca(OH)_2$. This production cost of $Ca(OH)_2$ using the proposed route is 2 to 3 times higher than the wholesale price of $Ca(OH)_2$ –ranging between \$140 to \$160 per t $Ca(OH)_2$ according to manufacturing companies – but could compete in the retail market where the cost varies between \$460 and \$560 per ton $Ca(OH)_2$. Assuming a sale price of \$560/ton $Ca(OH)_2$, the margin would be 22% and the payback period would be 10 years. A sensitivity analysis on the operating cost was performed considering the variables and variation ranges shown in Table 4.3 to evaluate the minimum and maximum operating costs.

Table 4.3. Variations in operating costs considered in the sensitivity analysis of $Ca(OH)_2$ production.

| ***OpEx* Variables** | **Minimum** | **Maximum** | **Units** |
|---|---|---|---|
| **Direct labor** | 2% | 8% | % Of CapEx per year |
| **Slag cost** | \$0 | \$10 | per ton of slag |
| **Electricity** | \$0.06 | \$0.13 | per kWh |
| **Membrane replacement** | 1 year | 5 years | Replacement frequency |
| **Slag transport** | 4 miles | 100 miles | Transport distance |

Figure 4.5 shows the results of the sensitivity analysis. The model is particularly sensitive to the cost of slag because depending on the type of slag the cost can vary between \$0 and \$10 per ton of slag, indicating that the cost of slag could become a major operating cost. A larger calcium extraction efficiency would reduce the sensitivity of the model to the cost of slag, underscoring the importance of improving the leaching efficiency of the process which is currently below 10%.[120] The frequency of membrane replacement is the second variable that more strongly influences the production cost of $Ca(OH)_2$. Finally, the sensitivity of model to the cost of slag

transport highlights that slag providers should be as close as possible to the $Ca(OH)_2$ production plant. The minimum and maximum production costs that could be achieved combining all the variables considered in the sensitivity analysis would be \$132.79 and \$743.24 per ton $Ca(OH)_2$.

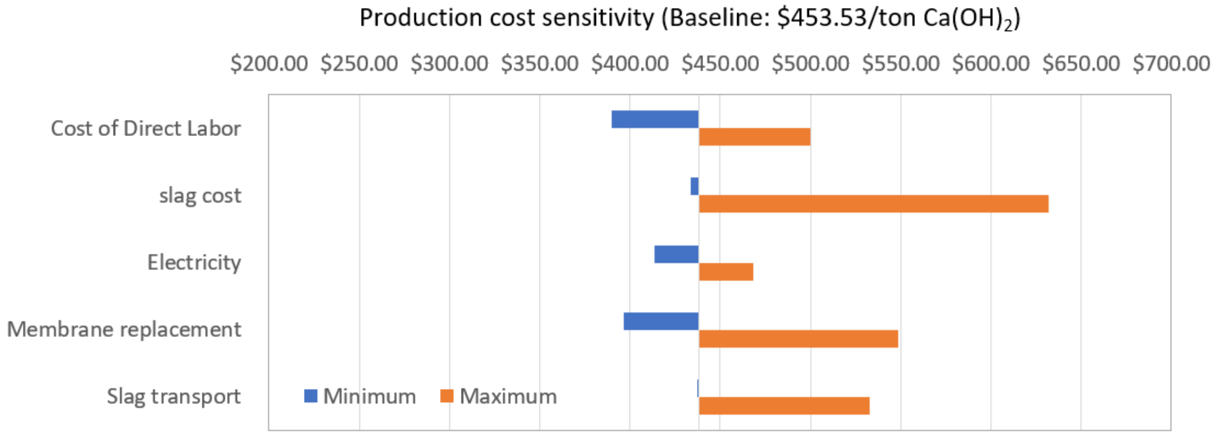

Figure 4.5. Sensitivity analysis of the operating cost (*OpEx*) of $Ca(OH)_2$ to the cost of labor, slag, electricity, transport, and membrane replacement frequency.

### 4.3.3. $CO_2$ footprint analysis

Figure 4.6 shows the 100-year global warming potential (GWP) of traditional and upcycled $Ca(OH)_2$ production assuming 3 different sources of electricity: (I) coal-fired power plant (II) natural gas-fired power plant and (III) solar thermal power plant. The figure shows that the traditional route to produce portlandite generates more $CO_2$ than the upcycled route. The main source of $CO_2$ emissions for the traditional route is limestone calcination, whereas for the proposed route is electricity consumption. Thus, the upcycled portlandite features a $CO_2$ footprint ranging 40% to 80% lower than the benchmark product when the electricity is sourced from natural gas and wind power, respectively. However, when the source of electricity is a coal fired power plant the $CO_2$ emissions of the proposed route could be 20% larger than the traditional route. Since the environmental impact of the proposed portlandite production route decreases when the source of electricity produces less $CO_2$, renewable energies such as solar thermal or geothermal would be beneficial because they could also supply the heat required for the process. The advantage of the proposed route becomes evident from Figure 4.7. Even if fossil fuels were completely replaced by a renewable energy source like hydrogen in the traditional $Ca(OH)_2$ production process, the $CO_2$ emissions from the calcination reaction would still be significant due to the calcination of limestone. Hence Figure 4.6 underscores the benefits of producing $Ca(OH)_2$ using slag (or other non-carbonate sources of calcium) and using renewable energy sources to produce a material that absorbs more $CO_2$ than what is required for its production throughout its life cycle, i.e., a $CO_2$-negative material.

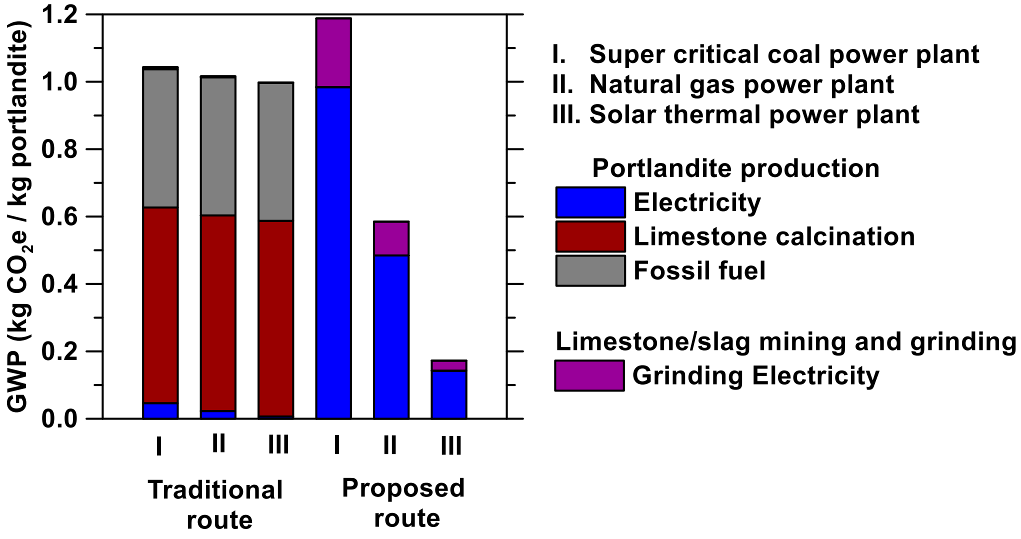

Figure 4.6. 100-year global warming potential (GWP) of traditional and upcycled $Ca(OH)_2$ production assuming three different sources of electricity: (I) Coal fired power plant (II) Natural gas fired power plant and (III) Solar thermal power.

### 4.3.4. Geospatial distribution analysis

The thermal power plants were categorized based on their yearly waste heat generation and their distance to the closest slag facility. Figure 4.7 shows the geospatial availability of slag and waste heat sources. More than 50 % of the total slag produced is in the Midwest region of the U.S. The amount of slag produced per year in the U.S. was calculated to be 10.3 million tons per year, in agreement with literature.[170] Nevertheless, USGS estimates that 14 million tons of slag are produced per year in the U.S,[171] suggesting that the present calculation underestimates domestic slag production. The results also highlight the need for more updated $CO_2$ emissions accounting in the steel industry since the newest database available was from 2015.[167] If 40% of the slag was composed of CaO, the domestic production of CaO from slag would be 4.1 million tons per year, indicating that the production of $Ca(OH)_2$ from slag could replace at most, a quarter of the entire lime market in the U.S. The study also revealed that the use of basic oxygen furnaces in the steel industry is decaying, indicating that in the supply chain of BOF slag will be affected in the near future, and that other types of slag (and other sources of calcium) should be considered for the proposed route.

Figure 4.7 shows the waste heat sources categorized based on the nominal capacity of the power plant (circle size) and by the distance to a slag source (circle color). Hence, large green circles represent the best implementation sites for the technology, whereas small red circles represent the least feasible sites. The figure indicates that there are 19 thermal power plants that generate between 10,000 and 50,000 GWh/y of waste heat located within 20 miles of a slag facility, and 41 thermal power plants with the same waste heat generation capacity located within 20 and 50 miles of a slag facility. Overall, a large upscale potential for upcycled concrete resides in the Northeast, Southeast and Midwest regions of the U.S. Based on the number of slag facilities and thermal power plant generating more than 10,000 GWh/y, the states with more potential for implementing a large-scale project are Pennsylvania, Alabama, Texas, Louisiana, Florida, North and South Carolina. Other states that have many slag facilities are Ohio, Illinois, and Indiana. Individual power plants in these states generate less than 10,000 GWh/y, but collectively they provide enough waste heat to process all the slag generated in these states. This study indicates that there is enough waste heat to produce $Ca(OH)_2$ with the proposed route and that the limiting resource is slag. However, a more detailed feasibility study should include the temperature at which waste heat is available.

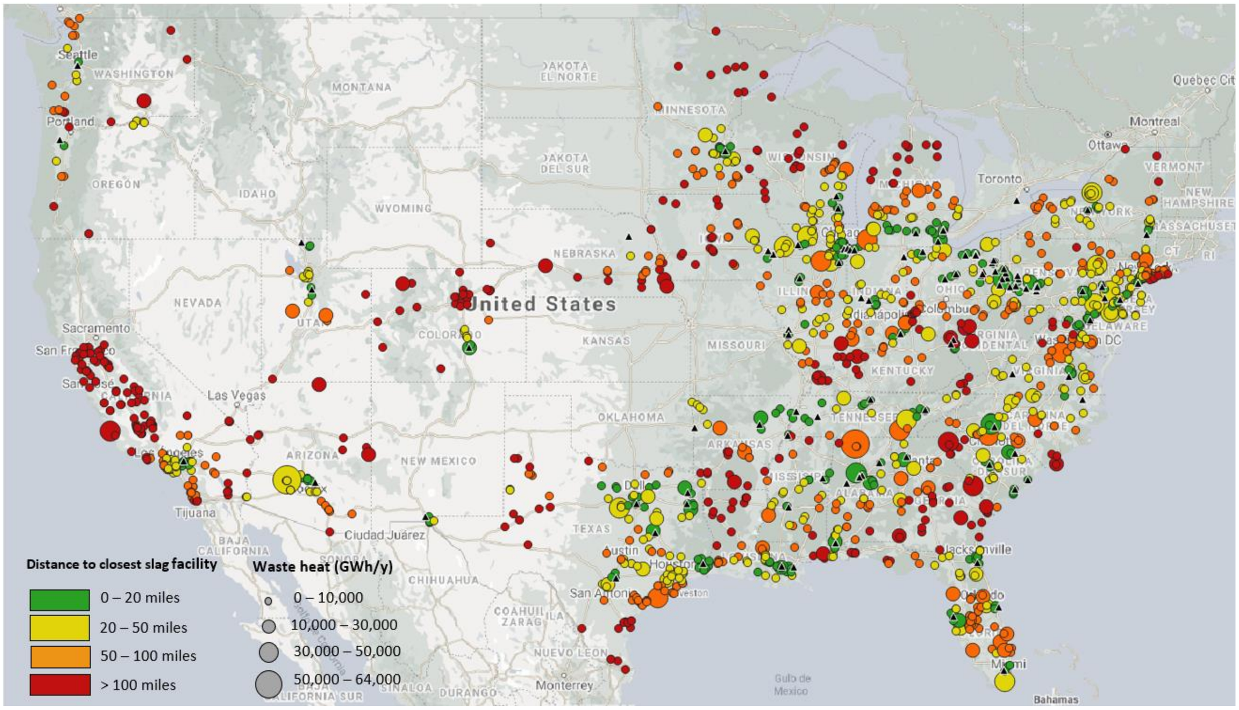

Figure 4.7. Geospatial availability of slag (triangles) and waste heat sources (circles)

## 4.4. Conclusion

This study evaluates the techno-economic feasibility and the environmental impact of a novel process integration scheme with thermal power plants to produce portlandite from alkaline industrial wastes for an optimized up-scaled base case scenario to produce 52 tons per day of $Ca(OH)_2$. The production cost of upcycled portlandite for the base case scenario is two to three times higher than the wholesale price of traditional portlandite. The main driver of the cost is the electricity, membrane replacement, and distributed capital costs. Nevertheless, the sensitivity analysis showed that a competitive operating cost can be achieved by increasing membrane lifetime and decreasing the electricity consumption, which could be achieved using membranes with higher pH resistance and operating at lower pressure. Research and development efforts to decrease the production cost of $Ca(OH)_2$ production should also be focused on improving the efficiency of the leaching step, *e.g.*, by using packed bed reactors, to minimize slag consumption without increasing electricity consumption.

The proposed $Ca(OH)_2$ production route features a $CO_2$ footprint 40% to 80% lower than the benchmark product when the electricity is sourced from natural gas and wind power, respectively. Finally, a geospatial analysis elucidates that, due to the proximity between feedstocks and waste heat sources, there are there are 60 thermal power plants in the U.S. with potential to up-scale the technology and to implement an industrial-scale facility to produce 50 tons of $Ca(OH)_2$ per day with a production cost of $453 per ton of $Ca(OH)_2$.

# CHAPTER 5

## Conclusion and Future Work

### 5.1. Conclusion

The objectives of this dissertation were to (i) demonstrate the calcination-free production of $Ca(OH)_2$ using precursors such as iron/steel processing wastes on the laboratory scale, (ii) to design and build an optimized integrated pilot process demonstrating the production of 1 kg of $Ca(OH)_2$ per day, and (iii) to evaluate the commercial feasibility of the proposed process using elements of financial, $CO_2$ footprint, and geospatial analysis.

The first objective was accomplished in Chapter 2, wherein a calcination-free pathway to produce $Ca(OH)_2$ using industrial alkaline wastes as a feedstock was demonstrated. The proof-of-concept tested on the small scale: (i) calcium leaching from slag, (ii) RO concentration of the alkaline Ca-containing solutions, and (iii) temperature-swing precipitation. Slag leaching in water produced Ca-concentrations ranging from 2 to 17 mM depending on the slag, s/l ratio, the presence of mixing (or not), and the leaching duration. It also demonstrated that achieving large calcium concentrations in solution by increasing the solid to liquid ratio during leaching comes at the expense of calcium extraction efficiency.[120] Additionally, results indicated that the maximum calcium concentration that can be sustained in solution during leaching was lower than the saturation concentration of $Ca(OH)_2$ at room temperature, demonstrating the need for the concentration step. Thereafter, the Ca-concentration in solution was systematically enhanced using RO membrane filtration. Finally, the retrograde solubility of portlandite was harnessed to precipitate $Ca(OH)_2$ from the concentrated solution, by imposing a temperature swing. The quantity of portlandite precipitated in this manner was congruent with estimates from equilibrium thermodynamic calculations.

The second objective was accomplished in Chapter 3 wherein the design and continuous operation of a pilot system to produce $Ca(OH)_2$ from industrial alkaline wastes as a feedstock was demonstrated. The mass and energy balances revealed that increasing the calcium concentration of the feed solution and the precipitation temperature, decrease the energy demands of the RO step. These optimized results outlined the operating conditions of the pilot process. The pilot system was built using commercially available components and integrated batch leaching with continuous RO concentration, and precipitation unit operations. The results enabled a detailed accounting of the energy consumption of the process and provided insights on process limitations and specific design requirements for the unit operations. Decreasing the slag particle size during leaching improved the calcium concentration of the leachate and increased the calcium extraction efficiency without the need to increase slag consumption. Moreover, the low energy demand, the reversibility of fouling and scaling, and the consistency of the results demonstrated that RO was a robust technology to concentrate the slag leachates and indicated good potential for upscaling the process. Finally, larger residence times in the precipitation reactor increased the crystal particle size and decreased the calcium concentration of the saturated solution $[Ca]_s$, indicating an increase in the quantity of $Ca(OH)_2$ precipitated per unit volume of solution.

The stability and reliability of the continuous process was demonstrated by completing three continuous tests of 8, 12, and 24 hours using the same RO membranes. The $Ca(OH)_2$ production rate was a function of the feed solution flow rate and it ranged from 0.45 to 1 kg per day. In all cases, the purity of the $Ca(OH)_2$ exceeded 94%. Additionally, the water was fully recirculated, making the water consumption of the process virtually zero. All the outcomes of the pilot study delivered important steps towards upscaling the process to produce $Ca(OH)_2$ from industrial wastes at low temperatures.

The third objective was accomplished in Chapter 4 wherein the techno-economic feasibility and the environmental impact of the process were evaluated for an up-scaled scenario producing 52 tons per day of $Ca(OH)_2$ from steel slag, assuming an integration scheme with thermal power plants to provide the waste heat for precipitation. The production cost of upcycled portlandite for the base case scenario was two to three times higher than the wholesale price of traditional portlandite. RO concentration was the unit operation that contributed the most to the production cost due to electricity, membrane replacement, and distributed capital expenses. Nevertheless, the sensitivity analysis showed that a competitive operating cost can be achieved by increasing membrane lifetime and decreasing the electricity consumption, which could be achieved using membranes with higher pH resistance and operating at lower pressure.

The proposed $Ca(OH)_2$ production route featured a $CO_2$ footprint 40% to 80% lower than the benchmark product when the electricity was sourced from natural gas and solar thermal power, respectively. Finally, a geospatial analysis on feedstocks and waste heat sources elucidated that there are 60 thermal power plants in the Northeast, Southeast and Midwest regions of the U.S. with potential to up-scale the technology and to implement an industrial-scale facility to produce 52 tons of $Ca(OH)_2$ per day with a production cost of $453 per ton of $Ca(OH)_2$.

## 5.2. Future work

### *Leaching*

In Chapter 1, different iron and steel slags were tested to determine the calcium concentration in solution obtained when they were leached with DI water. While herein we focused on ferrous slag, the calcium content and extraction potential from non-ferrous slag and other underutilized alkaline industrial wastes such as fly ash or bottom ash from coal and municipal waste combustion should be explored. Additionally, other naturally occurring alkaline minerals such as olivine could be considered. From a process perspective, research and development efforts should focus on improving the efficiency of the leaching step by maximizing the extraction of calcium with minimum electricity costs. For example, using other reactor architectures such as packed or fluidized beds, continuously stirred reactors or other semi-continuous processes that maximize calcium extraction with minimum electricity consumption.

### *RO concentration*

In Chapters 2 and 3, the RO concentration step was demonstrated using filmtec ® BW30XFR membranes. Nevertheless, the long-term stability and degradation behavior at high pH of these membranes should be carefully evaluated before up scaling the technology. Moreover, the suitability of other commercially available RO or nanofiltration membranes that have larger permeability (to decrease electricity consumption) and better resistance to high pH (>12) should be evaluated. Furthermore, considering that RO is a widespread technology for water treatment, integrating $Ca(OH)_2$ production as a co-process in the treatment of water streams with similar physical-chemical characteristics as the leachates presented in this study – e.g., slag quenching water from steel plants, or naturally occurring alkaline hard water – could be of interest. Indeed, the treatment of concentrates from NF and RO are major challenges to implementing membrane treatment processes and the precipitation of sparingly soluble salts could be a potential solution. Additionally, utilizing existing infrastructure would reduce the capital expenses associated with RO.

### *Precipitation*

In Chapter 3, operating the precipitation step at 100 °C was found to decrease the electricity requirements of the RO step. However, the overall energy consumption of the process was minimized when operating the precipitation step at 40 °C to 60 °C. This temperature range was also desirable for up-scaling as a large fraction of the waste heat in thermal power plants comes from condensers and is typically below 50 °C.[116] However, the yield of $Ca(OH)_2$ precipitated per liter of solution was minimum at this temperature range. Thus, evaluating the technical feasibility of operating the precipitation step at lower temperatures would be of interest. To increase the yield of $Ca(OH)_2$ precipitated per liter of solution and the specific RO pumping energy, the feed could be maintained at ~5 or 10 °C. Nevertheless, the electricity requirements of cooling would need to be evaluated and suitable (natural or industrial) available cooling streams should be identified.

### *Evaluation of alternative production methods*

In Chapter 4, the financial feasibility and $CO_2$ footprint of the method proposed in this dissertation to produce $Ca(OH)_2$ were compared with the traditional route. Nevertheless, other precipitation methods have been described in literature. For example, calcium hydroxide has been precipitated from aqueous solutions by combining $CaCl_2$ and NaOH,[103,172] or by electrochemical methods.[173,174] Thus, the financial feasibility and $CO_2$ footprint of these alternative production methods should be explored.

# Appendix A

## Supplementary Materials for Chapter 2

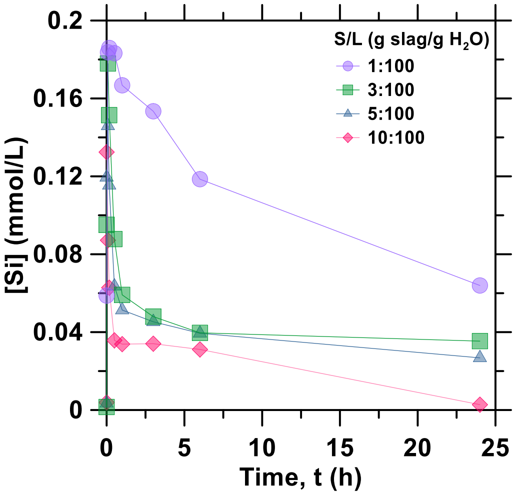

Figure A1. The silicon concentration as a function of time in stirred conditions following leaching of a BOF-slag.

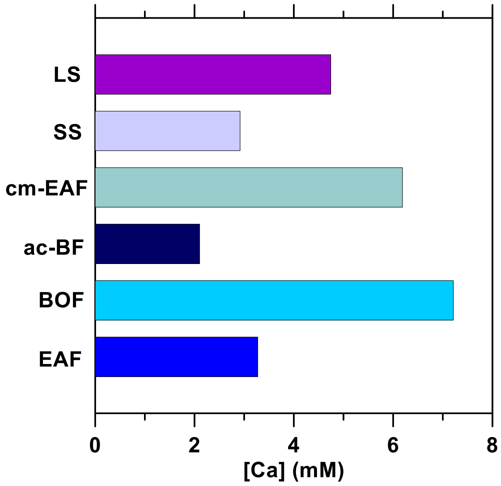

Figure A2. The Ca-concentration after 6 hours during leaching at 25 °C under stirred conditions (s/l = 0.01, particle size: 53 µm) for six different slag types including: ladle slag (LS), stainless steel slag (SS), co-mingled electric arc furnace steel slag (cm-EAF), air-cooled blast furnace slag (ac-BF), basic oxygen furnace slag (BOF), and electric arc furnace steel slag (EAF), respectively.

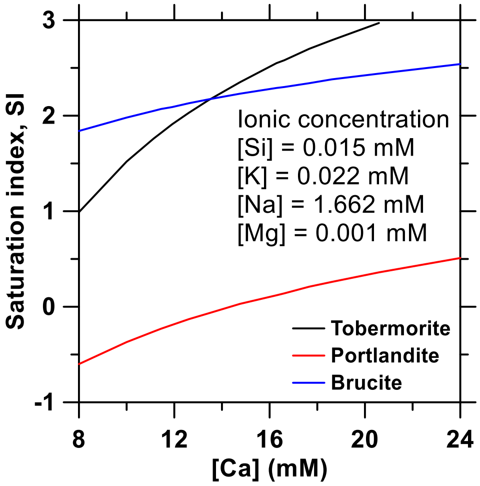

Figure A3. The saturation index of 11Å Tobermorite, Portlandite ($Ca(OH)_2$) and Brucite ($Mg(OH)_2$) as a function of [Ca] and in the presence of other ionic species (see legend) as calculated using PHREEQC. The concentration of the other dissolved elements in solution was measured through ICP-OES for the 10 mM slag leachate solution after 6 h of leaching.

***Ionic conductivity calculations***

The parameters to solve Onsager's equation can be calculated as follows: The ionic conductivity of each species at infinite dilution $\lambda_i^o$ is proportional to temperature in the range of our experiment. Figure S4 shows the reference value of $\lambda_i^o$ at each temperature.[175] Using the linear temperature dependence, $\lambda_i^o$ is calculated as a function of temperature T.

$$\lambda_{Ca}^o(T) = 1.941T + 3.087 \qquad \text{(A1)}$$

$$\lambda_{OH}^o(T) = 3.061T + 126.2 \qquad \text{(A2)}$$

Moreover, $S$ is calculated as

$$S_{Ca}(T) = \frac{1970 \times 10^6}{\{\varepsilon_r(T) \times T\}^{3/2}}\left(\frac{q(T)^*}{1 + \sqrt{q(T)^*}}\right) \times |z_{Ca} z_{OH}| \lambda_{Ca}^o(T) + \frac{28.98 \times |z_{Ca}|}{\eta(T) \times \{\varepsilon_r(T) \times T\}^{1/2}} \qquad \text{(A3)}$$

$$S_{OH}(T) = \frac{1970 \times 10^6}{\{\varepsilon_r(T) \times T\}^{3/2}}\left(\frac{q(T)^*}{1+\sqrt{q(T)^*}}\right) \times |z_{Ca}z_{OH}|\lambda_{OH}^{o}(T) + \frac{28.98 \times |z_{OH}|}{\eta(T) \times \{\varepsilon_r(T) \times T\}^{1/2}} \qquad \text{(A4)}$$

where, T represents temperature, $\eta$ the viscosity, $\varepsilon_r$ the relative permittivity of the medium, and $z_i$ the valence of each ionic species. The parameter q can be calculated as

$$q(T)^* = \frac{2}{3} \times \frac{\left(\lambda_{Ca}^{o}(T) + \lambda_{OH}^{o}(T)\right)}{\left(\lambda_{Ca}^{o}(T) + 2\lambda_{OH}^{o}(T)\right)} \qquad \text{(A5)}$$

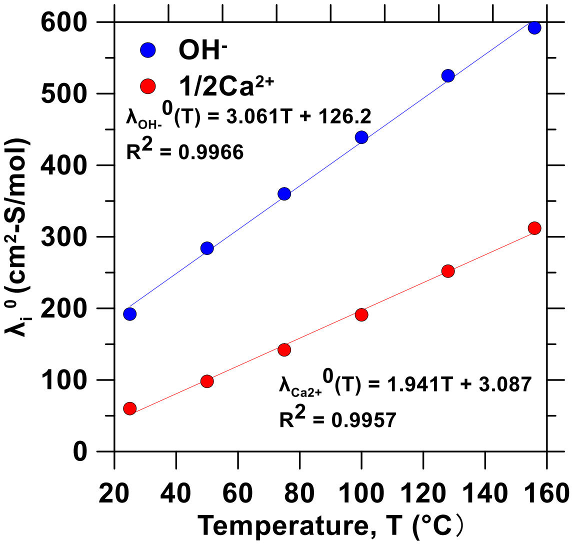

Figure A4. The relationship between temperature and equivalent conductivity at infinite dilution $\lambda_i^o$ of $Ca^{2+}$ and $OH^-$.[175]

Moreover, the relative permittivity $\varepsilon_r$ and the viscosity $\eta$ of the solvent are dependent on temperature T (in °C). Figure A5 shows the reference value of $\varepsilon_r$ at each temperature.[176] The value of $\varepsilon_r$ can be determined by the linear regression expressed as Equation S6 and $\eta$ is calculated by Equation A7.[177]

$$\varepsilon_r(T) = -0.3083T + 85.70 \qquad \text{(A6)}$$

$$\eta(T) = 2.414 \times 10^{-5} \times 10^{247.8/(T-140)} \qquad \text{(A7)}$$

Finally, the ional concentration $\Gamma$ can be calculated according to

$$\Gamma([Ca]_{aq}) = [Ca]_{aq} z_{Ca}{}^2 + [OH^-]_{aq} z_{OH}{}^2 \tag{A8}$$

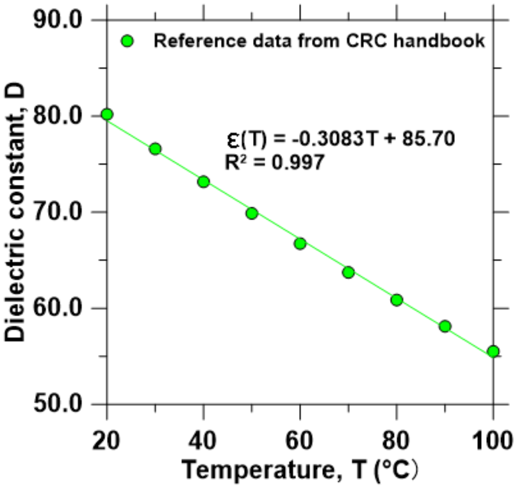

Figure A5. The relationship between temperature and the relative permittivity $\varepsilon_r$ of water.[176]

***Determination of the calcium concentration from the conductivity of the solution***

To determine aqueous calcium concentration $[Ca]_{aq}$ from the measured conductivity, it is necessary to describe the relationship between the hydroxide concentration $[OH^-]_{aq}$, $[Ca]_{aq}$ and temperature because the concentration of hydroxide $[OH^-]_{aq}$ dominantly affects the conductivity. Figure A6 shows the theoretical variation of $[OH^-]_{aq}$ as a function of temperature for different calcium concentrations $[Ca]_{aq}$ calculated using PHREEQC. It indicates that $[OH^-]_{aq}$ decreased linearly with temperature.

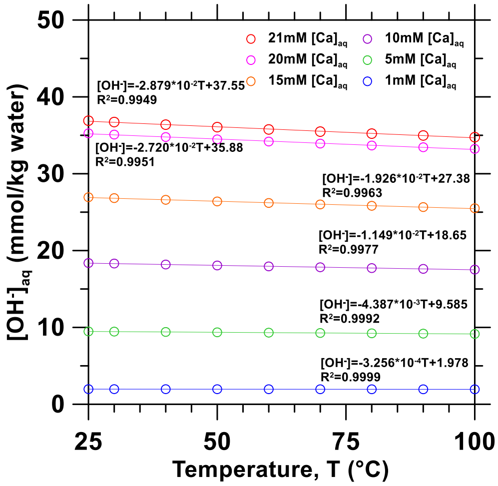

Figure A6. Theoretical variation of $[OH^{-}]_{aq}$ as a function of temperature for different calcium concentrations $[Ca]_{aq}$ calculated using PHREEQC.

The calibration equation was set as $[OH^{-}]_{aq} = \alpha T + \beta$, where $\beta$ is $[OH^{-}]_{aq}$ at 25 °C as a function of $[Ca]_{aq}$ and $\alpha$ describes the change in $[OH^{-}]_{aq}$ with increasing temperature and $[Ca]_{aq}$. Figure A7 shows the linear regression used to calculate $\alpha$ and $\beta$.

Hence, the change in $[OH^{-}]_{aq}$ as a function of temperature and calcium concentration is given by

$$[OH]_{aq} = -1.321 * 10^{-3}[Ca]_{aq}T + 1.806[Ca]_{aq} \tag{A9}$$

Finally, Equation A10 can be used to estimate [Ca] from conductivity measurements.

$$\sigma_{calc}\left([Ca]_{aq}, T\right) = 2[Ca]_{aq}\left\{\lambda_{Ca}^{o}(T) - S_{Ca}(T) \times \Gamma\left([Ca]_{aq}\right)^{1/2}\right\} \tag{A10}$$

$$+ [OH]_{aq}\left([Ca]_{aq}, T\right)\left\{\lambda_{OH}^{o}(T) - S_{OH}(T) \times \Gamma\left([Ca]_{aq}\right)^{1/2}\right\}$$

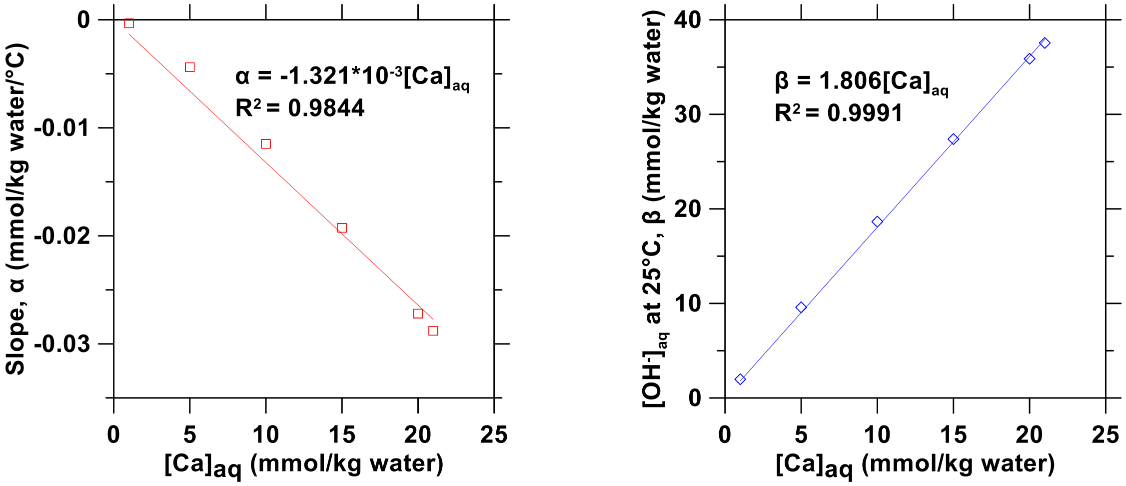

(a)

(b)

Figure A7. The parameters used for determining $[OH^-]_{aq}$ as a function of temperature and Ca-concentration: (a) slope α, and (b) intercept β, corresponding to $[OH^-]_{aq}$ at 25 °C.

***Calculation of energy required to produce $Ca(OH)_2$ using only waste heat***

Concentrating the calcium-rich leachate solution to precipitate 1 kg of $Ca(OH)_2$ using only waste heat would require the evaporation of 2466 L of water. First, the volume of water to be evaporated to bring the solution to the saturation point of $Ca(OH)_2$ (13.8 mM at 100 °C) was calculated as $\Delta V = V_i - V_f$. Where $V_i$ and $V_f$ are the initial and final solution volume before and after evaporation, respectively. Assuming the leachate solution has an initial volume $V_i$ of 5400 L and a [Ca] concentration $c_i$ of 10 mM (Figure S1), the solution volume after evaporation $V_f$ can be calculated according to $V_f = V_i c_i / c_f$, where $c_f = 13.8\,\mathrm{mM}$ corresponds to the saturation concentration of $Ca(OH)_2$ at 100 °C. Thus, 1487 L of water need to be evaporated. Second, precipitating 1 kg of $Ca(OH)_2$ from this saturated solution requires to evaporate 979 L of water, assuming that for every liter of water evaporated from the saturated solution, 13.8 millimoles of $Ca(OH)_2$ will precipitate. Thus, the total waste heat Q required to drive $Ca(OH)_2$ concentration and precipitation using only waste heat is given by

$$Q = V\rho\left(c_p\Delta T + h_{fg}\right) \qquad \text{A11}$$

where $V$ (=2466 L) is the volume of water evaporated, $\rho = 1$ kg/L and $c_p = 4.18$ kJ/(kg K) are the density and heat capacity of water, respectively, $\Delta T = 75$ K is the temperature difference and $h_{fg} = 2257$ kJ/kg is the heat of vaporization of water. Under these assumptions, Q = 6338 MJ would be necessary to precipitate 1 kg of $Ca(OH)_2$. By contrast, the total amount of energy for RO concentration and sub-boiling precipitation is 2.2 MJ of electricity and 677 MJ of waste heat, respectively. It is one order of magnitude lower than what is required to precipitate $Ca(OH)_2$ using waste heat only. Thus, the amount of waste heat of 5,000,000 GJ per year from a 10 $MW_e$ mid-sized power plant would enable the production of 7385 tons of $Ca(OH)_2$ per year when combined with RO concentration. By contrast, the production rate would be only 788 tons of $Ca(OH)_2$ per year if both concentration and precipitation are performed using only waste heat.

# Appendix B

## Supplementary Materials for Chapter 3

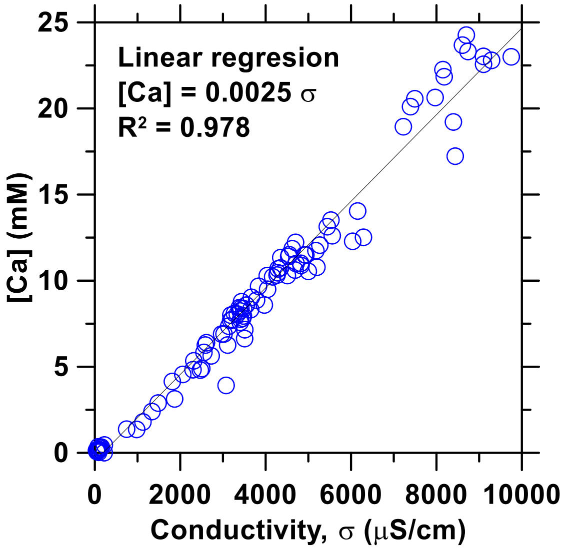

Figure B1. Calibration curve to relate conductivity and [Ca] Concentration in solution

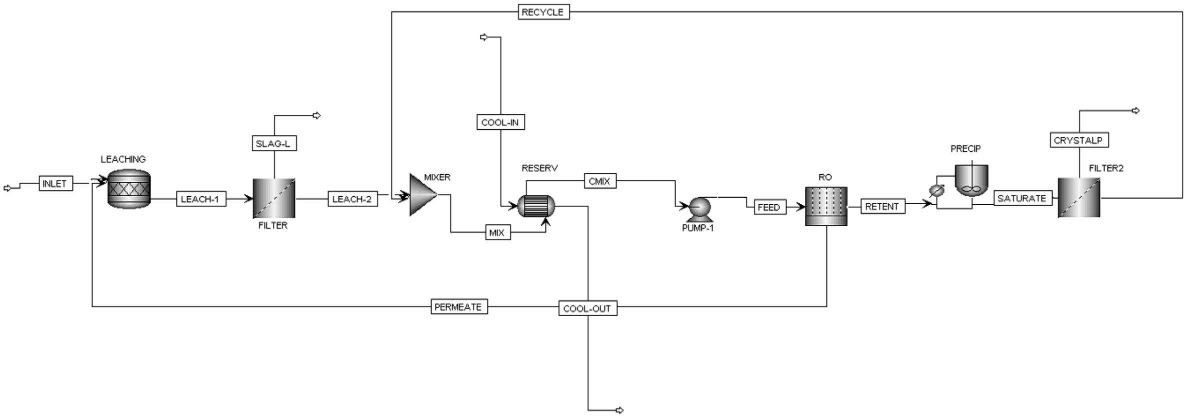

Figure B2. Flow sheet diagram of the Aspen plus V10 model.

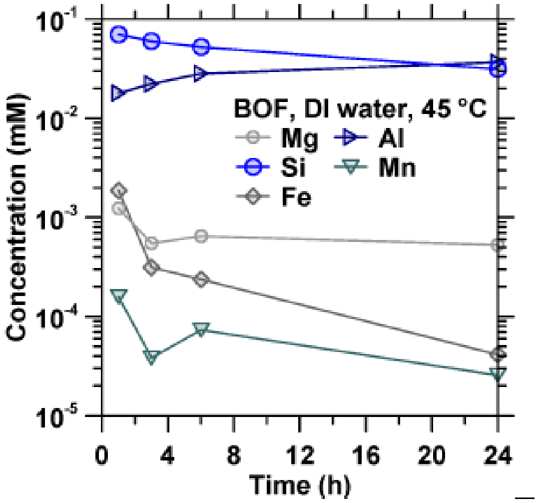

Figure B3. Elemental analysis of BOF slag leachates.

# Appendix C

## Supplementary Materials for Chapter 4

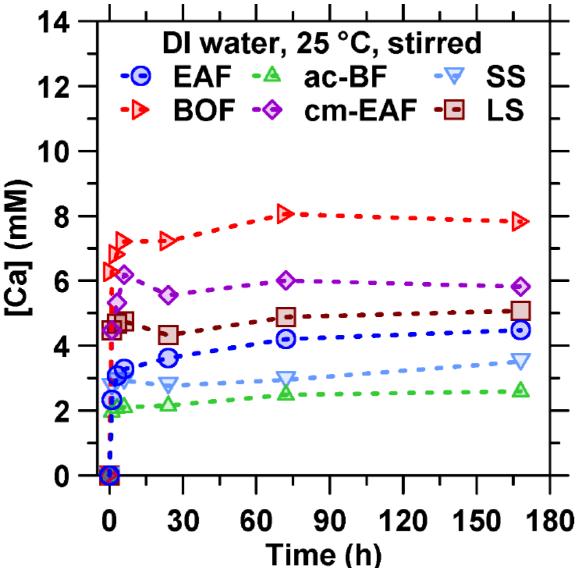

Figure C1. The Ca-concentration as a function of time during leaching at 25 °C under stirred conditions (s/l = 0.01, particle size: 53 μm) for six different slag types including: ladle slag (LS), stainless steel slag (SS), co-mingled electric arc furnace steel slag (cm-EAF), air-cooled blast furnace slag (ac-BF), basic oxygen furnace slag (BOF), and electric arc furnace steel slag (EAF), respectively.

### *RO pressure optimization*

- Reverse Osmosis concentration represents one of the largest operating cost for portlandite production
- RO operating cost is a tradeoff between electricity and membrane cost
- Cost optimization for base case scenario
  - Membrane replacement every 2 years
  - Minimum operating cost when operating at 1200 kPa

    - Membrane area required for the plant was estimated to be 169,232 $m^2$, which corresponds to a cost of $3,230,406
    - Minimum combined cost (membranes + electricity) is $183/ton $Ca(OH)_2$
- Sensitivity analysis of optimum cost as a function of membrane replacement frequency
    - At lower replacement frequency it is more cost effective to operate at a lower pressure
    - If membranes can be replaced every 5 years
        - Operating pressure can be reduced to 650 kPa
        - Combined operating cost would be $116/ton $Ca(OH)_2$

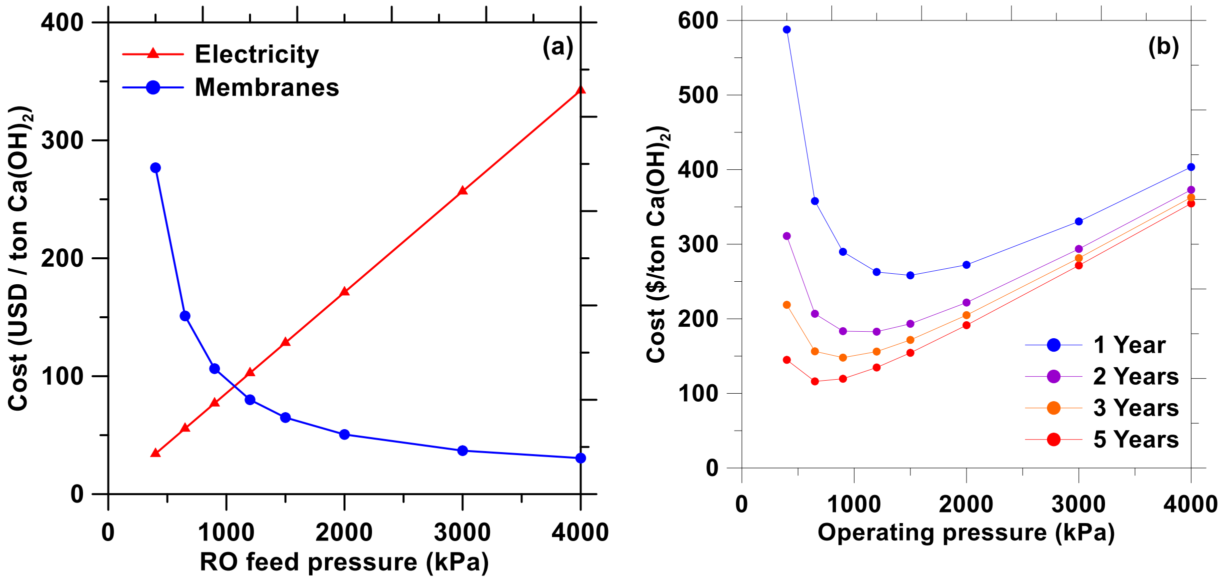

(a) (b)

Figure C2. (a) The cost of electricity and membrane replacement (assuming membranes should be replaced every 2 years) as a function of feed pressure for RO concentration, (b) Sensitivity analysis of optimum cost as a function of membrane replacement frequency

Table C1. Capital cost of major equipment required for RO installation taken from.[70] The Capital cost expenses considered for the RO unit are highlighted in blue.

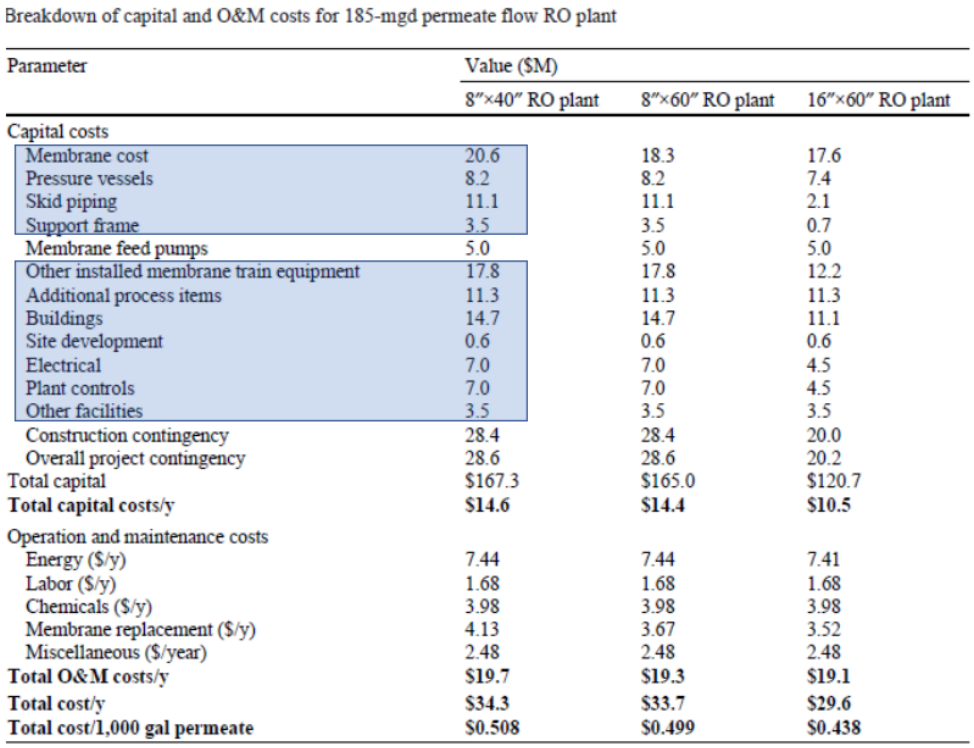

Breakdown of capital and O&M costs for 185-mgd permeate flow RO plant

| Parameter | Value ($M) | | |
|---|---|---|---|
| | 8″×40″ RO plant | 8″×60″ RO plant | 16″×60″ RO plant |
| Capital costs | | | |
| Membrane cost | 20.6 | 18.3 | 17.6 |
| Pressure vessels | 8.2 | 8.2 | 7.4 |
| Skid piping | 11.1 | 11.1 | 2.1 |
| Support frame | 3.5 | 3.5 | 0.7 |
| Membrane feed pumps | 5.0 | 5.0 | 5.0 |
| Other installed membrane train equipment | 17.8 | 17.8 | 12.2 |
| Additional process items | 11.3 | 11.3 | 11.3 |
| Buildings | 14.7 | 14.7 | 11.1 |
| Site development | 0.6 | 0.6 | 0.6 |
| Electrical | 7.0 | 7.0 | 4.5 |
| Plant controls | 7.0 | 7.0 | 4.5 |
| Other facilities | 3.5 | 3.5 | 3.5 |
| Construction contingency | 28.4 | 28.4 | 20.0 |
| Overall project contingency | 28.6 | 28.6 | 20.2 |
| Total capital | $167.3 | $165.0 | $120.7 |
| **Total capital costs/y** | **$14.6** | **$14.4** | **$10.5** |
| Operation and maintenance costs | | | |
| Energy ($/y) | 7.44 | 7.44 | 7.41 |
| Labor ($/y) | 1.68 | 1.68 | 1.68 |
| Chemicals ($/y) | 3.98 | 3.98 | 3.98 |
| Membrane replacement ($/y) | 4.13 | 3.67 | 3.52 |
| Miscellaneous ($/year) | 2.48 | 2.48 | 2.48 |
| **Total O&M costs/y** | **$19.7** | **$19.3** | **$19.1** |
| **Total cost/y** | **$34.3** | **$33.7** | **$29.6** |
| **Total cost/1,000 gal permeate** | **$0.508** | **$0.499** | **$0.438** |

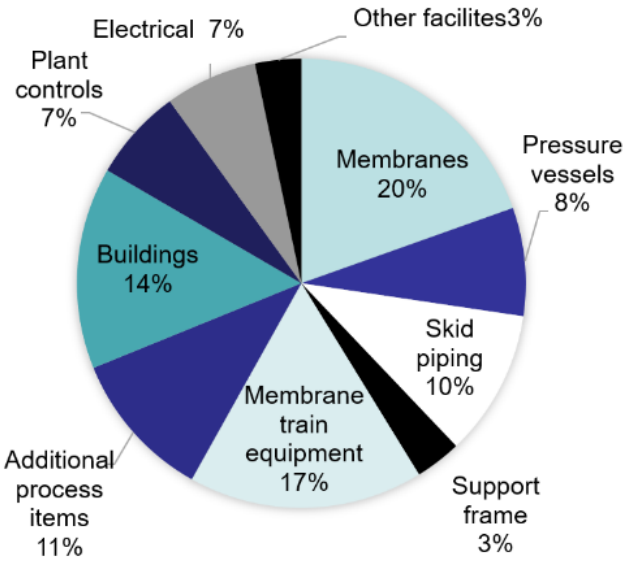

Figure C3. Capital cost expenses break down of RO unit operation

# References

1 W. M. Haynes, *CRC Handbook of Chemistry and Physics*, Taylor & Francis, Boca Raton, FL, U.S., 97th edn., 2017.

2 M. S. Fantle and E. T. Tipper, Calcium isotopes in the global biogeochemical Ca cycle: Implications for development of a Ca isotope proxy, *Earth-Science Reviews*, 2014, **129**, 148–177.

3 J. P. Grotzinger and J. F. Kasting, New Constraints on Precambrian Ocean Composition, *The Journal of Geology*, 1993, **101**, 235–243.

4 N. Korb and J. Jacobsen, in *Nutrient Management. A self-study course from the MSU extension service continuing education series*, Montana State University, 2002, p. 17.

5 J. Emsley, *Nature's Building Blocks: An A-Z Guide to the Elements*, OUP Oxford, 2011.

6 J. W. Mellor, *A Comprehensive Treatise on Inorganic and Theoretical Chemistry*, Longmans, Green and Co., Paternoster row, London, U.K., 2nd edn., 1928, vol. 3.

7 J. C. Willet, *Stone crushed*, U.S. Geological Survey (USGS), 2021.

8 Aigbedion and S. E. Iyayi, Environmental effect of mineral exploitation in Nigeria, *International Journal of Physical Sciences*, 2007, **2**, 33–38.

9 J. Vermeulen and T. Whitten, *Biodiversity and cultural property in the management of limestone resources - lessons from East Asia*, The World Bank, Washington, D.C., U.S., 1999.

10 C. Imboden, A. Komericki and A. Lyons, *LafargeHolcim biodiversity, management plans and Karst Biodiversity Management*, Fauna & Flora International, Cambridge, UK, 2018.

11 J. D. Bliss, T. S. Hayes and G. j Orris, *Limestone – A crucial and versatile industrial mineral commodity*, U.S. Geological Survey (USGS), 2008.

12 L. A. Corathers, *Lime*, U.S. Geological Survey (USGS), 2019.

13 K. C. Curry, *Cement*, U.S. Geological Survey (USGS), 2020.

14 M. Kenny and T. Oates, in *Ullmann's Encyclopedia of Industrial Chemistry*, Wiley-VCH, Weinheim, Germany, 1st edn., 2000.

15 A. Dowling, J. O'Dwyer and C. C. Adley, Lime in the limelight, *Journal of Cleaner Production*, 2015, **92**, 13–22.

16 H. Piringer, Lime shaft kilns, *Energy Procedia*, 2017, **120**, 75–95.

17 J. M. Crow, The concrete conundrum, *Chemistry World*, 2008, 62–66.

18 M. B. Ali, R. Saidur and M. S. Hossain, A review on emission analysis in cement industries, *Renewable and Sustainable Energy Reviews*, 2011, **15**, 2252–2261.

19 J. Timperley, Q&A: why cement emissions matter for climate change, https://www.carbonbrief.org/qa-why-cement-emissions-matter-for-climate-change, (accessed 14 October 2021).

20 C. Shi, A. F. Jiménez and A. Palomo, New cements for the 21st century: The pursuit of an alternative to Portland cement, *Cement and Concrete Research*, 2011, **41**, 750–763.

21 G. Falzone, I. Mehdipour, N. Neithalath, M. Bauchy, D. Simonetti and G. Sant, New insights into the mechanisms of carbon dioxide mineralization by portlandite, *AIChE J*, , DOI:10.1002/aic.17160.

22 S.-J. Han, M. Yoo, D.-W. Kim and J.-H. Wee, Carbon Dioxide Capture Using Calcium Hydroxide Aqueous Solution as the Absorbent, *Energy & Fuels*, 2011, **25**, 3825–3834.

23 K. S. Lackner, C. H. Wendt, D. P. Butt, E. L. Joyce and D. H. Sharp, Carbon dioxide disposal in carbonate minerals, *Energy*, 1995, **20**, 1153–1170.

24 K. Vance, G. Falzone, I. Pignatelli, M. Bauchy, M. Balonis and G. Sant, Direct carbonation of $Ca(OH)_2$ using liquid and supercritical $CO_2$: implications for carbon-neutral cementation, *Industrial and Engineering Chemistry Research*, 2015, **54**, 8908–8918.

25 Z. Wei, B. Wang, G. Falzone, E. C. La Plante, M. U. Okoronkwo, Z. She, T. Oey, M. Balonis, N. Neithalath, L. Pilon and G. Sant, Clinkering-free cementation by fly ash carbonation, *Journal of $CO_2$ Utilization*, 2018, **23**, 117–127.

26 I. Mehdipour, G. Falzone, E. C. La Plante, D. Simonetti, N. Neithalath and G. Sant, How microstructure and pore moisture affect strength gain in portlandite-enriched composites that mineralize $CO_2$, *ACS Sustainable Chemistry & Engineering*, 2019, **7**, 13053–13061.

27 R. S. Boynton, *Chemistry and Technology of Lime and Limestone*, Wiley, New York, NY, 2nd ed., 1980.

28 A. Arrigoni, R. Pelosato, P. Melià, G. Ruggieri, S. Sabbadini and G. Dotelli, Life cycle assessment of natural building materials: the role of carbonation, mixture components and transport in the environmental impacts of hempcrete blocks, *Journal of Cleaner Production*, 2017, **149**, 1051–1061.

29 K.-H. Yang, A.-R. Cho, J.-K. Song and S.-H. Nam, Hydration products and strength development of calcium hydroxide-based alkali-activated slag mortars, *Construction and Building Materials*, 2012, **29**, 410–419.

30 Strand, A, Korotkova, E, Willför, S, Hakala, J, and Lindstedt, E, The use of calcium hydroxide as alkali source in peroxide bleaching of kraft pulp, *Nordic Pulp & Paper Research Journal*, 2017, **32**, 444–451.

31 L. Semerjian and G. M. Ayoub, High-pH–magnesium coagulation–flocculation in wastewater treatment, *Advances in Environmental Research*, 2003, **7**, 389–403.

32 J. Leentvaar and M. Rebhun, Effect of magnesium and calcium precipitation on coagulation-flocculation with lime, *Water Research*, 1982, **16**, 655–662.

33 J. A. H. Oates, *Lime and Limestone: Chemistry and Technology, Production and Uses*, Wiley-VCH, Weinheim, Germany, 1998.

34 C. C. Dean, J. Blamey, N. H. Florin, M. J. Al-Jeboori and P. S. Fennell, The calcium looping cycle for $CO_2$ capture from power generation, cement manufacture and hydrogen production, *Chemical Engineering Research and Design*, 2011, **89**, 836–855.

35 M. Gollsch, S. Afflerbach, M. Drexler and M. Linder, Structural integrity of calcium hydroxide granule bulks for thermochemical energy storage, *Solar Energy*, 2020, **208**, 873–883.

36 S. Funayama, H. Takasu, M. Zamengo, J. Kariya, S. T. Kim and Y. Kato, Performance of thermochemical energy storage of a packed bed of calcium hydroxide pellets, *Energy Storage*, 2019, **1**, e40.

37 M. Stork, W. Meindertsma, M. Overgaag and M. Neils, *A competitive and efficient lime industry*, EuLA – The European Lime Association, Brussels, Belgium, 2014.

38 E. Belhadj, C. Diliberto and A. Lecomte, Characterization and activation of Basic Oxygen Furnace slag, *Cement and Concrete Composites*, 2012, **34**, 34–40.

39 N. M. Piatak, M. B. Parsons and R. R. Seal, Characteristics and environmental aspects of slag: a review, *Applied Geochemistry*, 2015, **57**, 236–266.

40 *World Steel Association Life Cycle Inventory study report*, 2019.

41 H. Wang, J.-J. Wu, X. Zhu, Q. Liao and L. Zhao, Energy–environment–economy evaluations of commercial scale systems for blast furnace slag treatment: Dry slag granulation vs. water quenching, *Applied Energy*, 2016, **171**, 314–324.

42 M. Tossavainen, F. Engstrom, Q. Yang, N. Menad, M. Lidstrom Larsson and B. Bjorkman, Characteristics of steel slag under different cooling conditions, *Waste Management*, 2007, **27**, 1335–1344.

43 Y.-L. Chen and C.-T. Lin, Recycling of basic oxygen furnace slag as a raw material for autoclaved aerated concrete production, *Sustainability*, 2020, **12**, 5896.

44 T.-H. Lu, Y.-L. Chen, P.-H. Shih and J.-E. Chang, Use of basic oxygen furnace slag fines in the production of cementitious mortars and the effects on mortar expansion, *Construction and Building Materials*, 2018, **167**, 768–774.

45 K. C. Curry and USGS, *Iron and steel slag*, 2020.

46 J. K. Stolaroff, G. V. Lowry and D. W. Keith, Using CaO- and MgO-rich industrial waste streams for carbon sequestration, *Energy Conversion and Management*, 2005, **46**, 687–699.

47 S. Chand, B. Paul and M. Kumar, Sustainable Approaches for LD Slag Waste Management in Steel Industries: A Review, *Metallurgist*, 2016, **60**, 116–128.

48 J. A. Ober, *Iron and Steel Slag*, U.S. Geological Survey (USGS), 2021.

49 D. B. Muller, T. Wang, B. Duval and T. E. Graedel, Exploring the engine of anthropogenic iron cycles, *Proceedings of the National Academy of Sciences*, 2006, **103**, 16111–16116.

50 A. Sanna, M. Uibu, G. Caramanna, R. Kuusik and M. M. Maroto-Valer, A review of mineral carbonation technologies to sequester $CO_2$, *Chem. Soc. Rev.*, 2014, **43**, 8049–8080.

51 S.-Y. Pan, E. E. Chang and P.-C. Chiang, $CO_2$ Capture by accelerated carbonation of alkaline wastes: a review on its principles and applications, *Aerosol and Air Quality Research*, 2012, **12**, 770–791.

52 *Analysis of MSW landfill tipping fees*, EREF, 2019.

53 R. S. Iyer and J. A. Scott, Power station fly ash — a review of value-added utilization outside of the construction industry, *Resources, Conservation and Recycling*, 2001, **31**, 217–228.

54 C. L. Carlson and D. C. Adriano, Environmental impacts of coal combustion residues, *Journal of Environmental Quality*, 1993, **22**, 227–247.

55 E. S. Rubin, J. R. Kalagnanam, H. C. Frey and M. B. Berkenpas, Integrated environmental control modeling of coal-fired power systems, *Journal of the Air & Waste Management Association*, 1997, **47**, 1180–1188.

56 M. Loncnar, H. A. van der Sloot, A. Mladenovič, M. Zupančič, L. Kobal and P. Bukovec, Study of the leaching behaviour of ladle slags by means of leaching tests combined with geochemical modelling and mineralogical investigations, *Journal of Hazardous Materials*, 2016, **317**, 147–157.

57 L. De Windt, P. Chaurand and J. Rose, Kinetics of steel slag leaching: batch tests and modeling, *Waste Management*, 2011, **31**, 225–235.

58 W. R. Stahel, The circular economy, *Nature*, 2016, **531**, 435–438.

59 T. H. Adams, *Coal Ash Recycling Rate Declines Amid Shifting Production and Use Patterns*, ACAA, Washington, D.C., U.S., 2019.

60 M. Ahmaruzzaman, A review on the utilization of fly ash, *Progress in Energy and Combustion Science*, 2010, **36**, 327–363.

61 G. Montes-Hernandez, R. Pérez-López, F. Renard, J. M. Nieto and L. Charlet, Mineral sequestration of $CO_2$ by aqueous carbonation of coal combustion fly-ash, *Journal of Hazardous Materials*, 2009, **161**, 1347–1354.

62 A. Ćwik, I. Casanova, K. Rausis, N. Koukouzas and K. Zarębska, Carbonation of high-calcium fly ashes and its potential for carbon dioxide removal in coal fired power plants, *Journal of Cleaner Production*, 2018, **202**, 1026–1034.

63 Y.-H. Hsiao, X. Chen, E. C. La Plante, A. Kumar, M. Bauchy, D. Simonetti, D. Jassby, J. Israelachvili and G. Sant, Mineral dissolution under electric stimulation, *The Journal of Physical Chemistry C*, 2020, **124**, 16515–16523.

64 Z. Wei, Y.-H. Hsiao, X. Chen, E. C. La Plante, I. Mehdipour, D. Simonetti, N. Neithalath, L. Pilon, M. Bauchy, J. Israelachvili and G. Sant, Isothermal stimulation of mineral dissolution processes by acoustic perturbation, *The Journal of Physical Chemistry C*, 2018, **122**, 28665–28673.

65 *PHREEQC , Version 3*, U.S. Geological Survey, 2017.

66 L. Malaeb and G. M. Ayoub, Reverse osmosis technology for water treatment: state of the art review, *Desalination*, 2011, **267**, 1–8.

67 R. G. Bates, V. E. Bower and E. R. Smith, Calcium hydroxide as a highly alkaline pH standard, *Journal of Research of the National Bureau of Standards*, 1956, **56**, 305–312.

68 A. Pérez-González, A. M. Urtiaga, R. Ibáñez and I. Ortiz, State of the art and review on the treatment technologies of water reverse osmosis concentrates, *Water Research*, 2012, **46**, 267–283.

69 Y. Choi, H. Cho, Y. Shin, Y. Jang and S. Lee, Economic evaluation of a hybrid desalination system combining forward and reverse osmosis, *Membranes*, 2015, **6**, 3.

70 T. I. Yun, C. J. Gabelich, M. R. Cox, A. A. Mofidi and R. Lesan, Reducing costs for large-scale desalting plants using large-diameter, reverse osmosis membranes, *Desalination*, 2006, **189**, 141–154.

71 M. Li, Reducing specific energy consumption in Reverse Osmosis (RO) water desalination: An analysis from first principles, *Desalination*, 2011, **276**, 128–135.

72 A. Bódalo-Santoyo, Spiral-wound membrane reverse osmosis and the treatment of industrial effluents, *Desalination*, 2004, **160**, 151–158.

73 Y. Gendel, A. K. E. Rommerskirchen, O. David and M. Wessling, Batch mode and continuous desalination of water using flowing carbon deionization (FCDI) technology, *Electrochemistry Communications*, 2014, **46**, 152–156.

74 J. O. Bockris and A. K. N. Reddy, *Modern electrochemistry*, Plenum, New York, U.S., 1970, vol. 1.

75 H. S. Harned and B. B. Owen, *The Physical Chemistry of Electrolytic Solutions*, Reinhold Publishing Corporation, New York, U.S., 1939.

76 R. Gabrovšek, T. Vuk and V. Kaučič, Evaluation of the hydration of portland cement containing various carbonates by means of thermal analysis, *Acta Chimica Slovenica*, 2006, **53**, 159–165.

77 M. Khachani, A. E. Hamidi, M. Halim and S. Arsalane, Non-isothermal kinetic and thermodynamic studies of the dehydroxylation process of synthetic calcium hydroxide $Ca(OH)_2$, *Journal of Materials and Environmental science*, 2014, **5**, 615–624.

78 M.-A. Popescu, R. Isopescu, C. Matei, G. Fagarasan and V. Plesu, Thermal decomposition of calcium carbonate polymorphs precipitated in the presence of ammonia and alkylamines, *Advanced Powder Technology*, 2014, **25**, 500–507.

79 W. M. Deen, *Analysis of Transport Phenomena*, Oxford University Press, New York, 1998.

80 H. F. W. Taylor, *Cement chemistry*, Thomas Telford, London, 2nd ed., 1997.

81 W. J. J. Huijgen and R. N. J. Comans, Mineral $CO_2$ sequestration by steel slag carbonation, *Environmental Science & Technology*, 2005, **39**, 9676–9682.

82 W. J. J. Huijgen and R. N. J. Comans, Carbonation of steel slag for $CO_2$ sequestration: Leaching products and reaction mechanisms, *Environmental Science & Technology*, 2006, **40**, 2790–2796.

83 N. M. Piatak, Environmental Characteristics and Utilization Potential of Metallurgical Slag, *Environmental Geochemistry: Site Characterization, Data Analysis and Case Histories*, Elsevier, 2018, pp. 487–519.

84 S. Yadav and A. Mehra, Dissolution of steel slags in aqueous media, *Environ Sci Pollut Res*, 2017, **24**, 16305–16315.

85 F. Zhang and H. Itoh, Extraction of metals from municipal solid waste incinerator fly ash by hydrothermal process, *Journal of Hazardous Materials*, 2006, **136**, 663–670.

86 Y. Sun, V. Parikh and L. Zhang, Sequestration of carbon dioxide by indirect mineralization using Victorian brown coal fly ash, *Journal of Hazardous Materials*, 2012, **209–210**, 458–466.

87 S. Eloneva, S. Teir, J. Salminen, C.-J. Fogelholm and R. Zevenhoven, Steel converter slag as a raw material for precipitation of pure calcium carbonate, *Industrial & Engineering Chemistry Research*, 2008, **47**, 7104–7111.

88 S.-Y. Pan, P.-C. Chiang, Y.-H. Chen, C.-D. Chen, H.-Y. Lin and E.-E. Chang, Systematic approach to determination of maximum achievable capture capacity via leaching and carbonation processes for alkaline steelmaking wastes in a rotating packed bed, *Environmental Science & Technology*, 2013, **47**, 13677–13685.

89 M. Mulder, *Basic Principles of Membrane Technology*, Springer Netherlands, Amsterdam, 2nd edn., 1996.

90 B. Ladewig and B. Asquith, Characteristics of membrane concentrate in *Desalination Concentrate Management*, Springer, Berlin, Heidelberg, 2012, pp. 5–15.

91 K. Jane, The Essentials of Reverse Osmosis, *Chemical Engineering Progress*, 2019.

92 J. Gilron and D. Hasson, Calcium sulphate fouling of reverse osmosis membrane - flux decline mechanism, *Chemical Engineering Science*, 1987, **42**, 2351–2360.

93 C. J. Lin, S. Shirazi, P. Rao and S. Agarwal, Effects of operational parameters on cake formation of CaSO4 in nanofiltration, *Water Research*, 2006, **40**, 806–816.

94 M. Uchymiak, A. R. Bartman, N. Daltrophe, M. Weissman, J. Gilron, P. D. Christofides, W. J. Kaiser and Y. Cohen, Brackish water reverse osmosis (BWRO) operation in feed flow reversal mode using an ex situ scale observation detector (EXSOD), *Journal of Membrane Science*, 2009, **341**, 60–66.

95 E. M. Vrijenhoek, S. Hong and M. Elimelech, Influence of membrane surface properties on initial rate of colloidal fouling of reverse osmosis and nanofiltration membranes, *Journal of Membrane Science*, 2001, **188**, 115–128.

96 C. J. Gabelich, A. Rahardianto, C. R. Northrup, T. I. Yun and Y. Cohen, Process evaluation of intermediate chemical demineralization for water recovery enhancement in production-scale brackish water desalting, *Desalination*, 2011, **272**, 36–45.

97 R. Sheikholeslami and J. Bright, Silica and metals removal by pretreatment to prevent fouling of reverse osmosis membranes, *Desalination*, 2002, **143**, 255–267.

98 J. Gilron, M. Waisman, N. Daltrophe, N. Pomerantz, M. Milman, I. Ladizhansky and E. Korin, Prevention of precipitation fouling in NF/RO by reverse flow operation, *Desalination*, 2006, **199**, 29–30.

99 D. Hou, C. Hu and Z. Li, Molecular simulation of the ions ultraconfined in the nanometer-channel of calcium silicate hydrate: Hydration mechanism, dynamic properties, and influence on the cohesive strength, *Inorganic Chemistry*, 2017, **56**, 1881–1896.

100 F. P. Glasser, E. E. Lachowski and D. E. Macphee, Compositional model for calcium silicate hydrate (C-S-H) gels, their solubilities, and free energies of formation, *Journal of the American Ceramic Society*, 1987, **70**, 481–485.

101 S. Goto, M. Daimon, G. Hosaka and R. Kondo, Composition and Morphology of Hydrated Tricalcium Silicate, *Journal of the American Ceramic Society*, 1976, **59**, 281–284.

102 R. Gabrovšek, T. Vuk and V. Kaučič, Evaluation of the hydration of Portland cement containing various carbonates by means of thermal analysis, *Acta Chimica Slovenica*, 2006, **53**, 159–165.

103 E. Ruiz-Agudo, K. Kudłacz, C. V. Putnis, A. Putnis and C. Rodriguez-Navarro, Dissolution and carbonation of portlandite [$Ca(OH)_2$] single crystals, *Environmental Science & Technology*, 2013, **47**, 11342–11349.

104 C. Rodriguez-Navarro, E. Hansen and W. S. Ginell, Calcium hydroxide crystal evolution upon aging of lime putty, *Journal of the American Ceramic Society*, 2005, **81**, 3032–3034.

105 C. Speiser, T. Baumann and R. Niessner, Morphological and chemical characterization of calcium-hydrate phases formed in alteration processes of deposited municipal solid waste incinerator bottom ash, *Environmental Science and Technology*, 2000, **34**, 5030–5037.

106 X. Zhang, F. P. Glasser and K. L. Scrivener, Reaction kinetics of dolomite and portlandite, *Cement and Concrete Research*, 2014, **66**, 11–18.

107 M. Galván-Ruiz, J. Hernández, L. Baños, J. Noriega-Montes and M. E. Rodríguez-García, Characterization of calcium carbonate, calcium oxide, and calcium hydroxide as starting point to the improvement of Lime for their use in construction, *Journal of Materials in Civil Engineering*, 2009, **21**, 694–698.

108 G. Madras and B. J. McCoy, Growth and ripening kinetics of crystalline polymorphs, *Crystal Growth & Design*, 2003, **3**, 981–990.

109 G. Madras and B. J. McCoy, Temperature effects on the transition from nucleation and growth to Ostwald ripening, *Chemical Engineering Science*, 2004, **59**, 2753–2765.

110 S.-J. Kim, S.-D. Park, Y. H. Jeong and S. Park, Homogeneous precipitation of $TiO_2$ ultrafine powders from aqueous $TiOCl_2$ solution, *Journal of the American Ceramic Society*, 1999, **82**, 927–932.

111 F. Zeman, Energy and material balance of $CO_2$ capture from ambient air, *Environmental Science & Technology*, 2007, **41**, 7558–7563.

112 A. Sagastume Gutiérrez, J. B. Cogollos Martínez and C. Vandecasteele, Energy and exergy assessments of a lime shaft kiln, *Applied Thermal Engineering*, 2013, **51**, 273–280.

113 *A Competitive and Efficient Lime Industry*, European Lime Association EuLA, Brussels, Belgium.

114 R. W. Fox, A. T. McDonald and P. J. Pritchard, *Introduction to Fluid Mechanics*, John Wiley & Sons Inc, Hoboken, NJ, 8th edn., 2011.

115 T. L. Bergman, A. S. Lavine, F. P. Incropera and D. P. Dewitt, *Fundamentals of Heat and Mass Transfer*, Wiley, Hoboken, NJ, 7th ed., 2011.

116 D. B. Gingerich and M. S. Mauter, Quantity, quality, and availability of waste heat from United States thermal power generation, *Environmental Science & Technology*, 2015, **49**, 8297–8306.

117 F. Kreith, P. Norton and D. Brown, A comparison of $CO_2$ emissions from fossil and solar power plants in the united states, *Energy*, 1990, **15**, 1181–1198.

118 J. J. Burkhardt, G. Heath and E. Cohen, Life cycle greenhouse gas emissions of trough and tower concentrating solar power electricity generation: Systematic review and harmonization, *Journal of Industrial Ecology*, 2012, **16**, S93–S109.

119 J. A. de Chalendar, J. Taggart and S. M. Benson, Tracking emissions in the US electricity system, *Proceedings of the National Academy of Sciences*, 2019, **116**, 25497–25502.

120 S. Vallejo Castaño, E. Callagon La Plante, S. Shimoda, B. Wang, N. Neithalath, G. Sant and L. Pilon, Calcination-free production of calcium hydroxide at sub-boiling temperatures, *RSC Advances*, 2021, **11**, 1762–1772.

121 J. J. Chen, J. J. Thomas, H. F. W. Taylor and H. M. Jennings, Solubility and structure of calcium silicate hydrate, *Cement and Concrete Research*, 2004, **34**, 1499–1519.

122 H. M. Jennings, Aqueous solubility relationships for two types of calcium silicate hydrate, *Journal of the American Ceramic Society*, 1986, **69**, 614–618.

123 C. S. Walker, S. Sutou, C. Oda, M. Mihara and A. Honda, Calcium silicate hydrate (C-S-H) gel solubility data and a discrete solid phase model at 25 °C based on two binary non-ideal solid solutions, *Cement and Concrete Research*, 2016, **79**, 1–30.

124 Y. Ghasemi, M. Emborg and A. Cwirzen, Estimation of specific surface area of particles based on size distribution curve, *Magazine of Concrete Research*, 2018, **70**, 533–540.

125 C. Thomas, J. Rosales, J. A. Polanco and F. Agrela, in *New Trends in Eco-efficient and Recycled Concrete*, Elsevier, Cambridge, United States, 2019, pp. 169–190.

126 I. Z. Yildirim and M. Prezzi, Chemical, mineralogical, and morphological properties of steel slag, *Advances in Civil Engineering*, 2011, **2011**, 1–13.

127 F. C. Bond, Crushing and grinding calculations, *British Chemical Engineering*, 1961, **6**, 378–385.

128 N. L. Weiss and Society of Mining Engineers of AIME, *SME Mineral Processing Handbook*, Society of Mining Engineers of the American Institute of Mining, Metallurgical, and Petroleum Engineers, New York, NY, 1985.

129 P. M. Doran, *Bioprocess engineering principles*, Elsevier, Oxford, UK, 2nd ed., 2013.

130 *AspenONE (Version 10)*, Aspen Technology, Inc., 2017.

131 M. Mulder, *Basic Principles of Membrane Technology*, Springer, Dordrecht, Netherlands, 1st ed., 1991.

132 E. Dražević, K. Košutić and V. Freger, Permeability and selectivity of reverse osmosis membranes: correlation to swelling revisited, *Water Research*, 2014, **49**, 444–452.

133 H. Dach, Comparison of nanofiltration and reverse osmosis processes for a selective desalination of brackish water feeds, Université d'Angers, 2008.

134 W. Lawler, T. Wijaya, A. Antony, G. Leslie and P. Le-Clech, in *IDA World Congress*, Perth, Western Australia, 2011.

135 Y. S. Oren and P. M. Biesheuvel, Theory of ion and water transport in reverse-osmosis membranes, *Physical Review Applied*, , DOI:10.1103/PhysRevApplied.9.024034.

136 C. Shi and J. Qian, High performance cementing materials from industrial slags — a review, *Resources, Conservation and Recycling*, 2000, **29**, 195–207.

137 E. Belhadj, C. Diliberto and A. Lecomte, Characterization and activation of basic oxygen furnace slag, *Cement and Concrete Composites*, 2012, **34**, 34–40.

138 J.-M. Gautier, E. H. Oelkers and J. Schott, Are quartz dissolution rates proportional to B.E.T. surface areas?, *Geochimica et Cosmochimica Acta*, 2001, **65**, 1059–1070.

139 W. L. Ebert, *The effects of the glass surface area/solution volume ratio on glass corrosion: A critical review*, Argonne National Laboratory, Argonne, Illinois, 1995.

140 E. M. V. Hoek, A. S. Kim and M. Elimelech, Influence of crossflow membrane filter geometry and shear rate on colloidal fouling in reverse osmosis and nanofiltration separations, *Environmental Engineering Science*, 2002, **19**, 357–372.

141 X. Zhu and M. Elimelech, Colloidal fouling of reverse osmosis membranes: measurements and fouling mechanisms, *Environmental Science & Technology*, 1997, **31**, 3654–3662.

142 D. Klein, Homogeneous nucleation of calcium hydroxide, *Talanta*, 1968, **15**, 229–231.

143 H. Furedi-Milhofer, Spontaneous precipitation from electrolytic solutions, *Pure and Applied Chemistry*, 1981, **53**, 2041–2055.

144 J. R. Ray, W. Wong and Y.-S. Jun, Antiscaling efficacy of $CaCO_3$ and $CaSO_4$ on polyethylene glycol (PEG)-modified reverse osmosis membranes in the presence of humic acid: interplay of membrane surface properties and water chemistry, *Physical Chemistry Chemical Physics*, 2017, **19**, 5647–5657.

145 D. Lesueur, J. Petit and H.-J. Ritter, The mechanisms of hydrated lime modification of asphalt mixtures: a state-of-the-art review, *Road Materials and Pavement Design*, 2013, **14**, 1–16.

146 L. B. Miller and J. C. Witt, Solubility of calcium hydroxide, *The Journal of Physical Chemistry*, 1929, **33**, 285–289.

147 M. E. Tadros, J. Skalny and R. S. Kalyoncu, Kinetics of calcium hydroxide crystal growth from solution, *Journal of Colloid and Interface Science*, 1976, **55**, 20–24.

148 K. Johannsen and S. Rademacher, Modelling the kinetics of calcium hydroxide dissolution in water, *Acta hydrochimica et hydrobiologica*, 1999, **27**, 72–78.

149 J. Duchesne and E. J. Reardon, Measurement and prediction of portlandite solubility in alkali solutions, *Cement and Concrete Research*, 1995, **25**, 1043–1053.

150 I. C. Kemp, Reducing dryer energy use by process integration and pinch analysis, *Drying Technology*, 2005, **23**, 2089–2104.

151 J. C. Atuonwu, G. van Straten, H. C. van Deventer and A. J. B. van, Optimizing energy efficiency in low temperature drying by zeolite adsorption and process integration, *Chemical Engineering Transactions*, 2011, **25**, 111–116.

152 G.N. Sant, L.G. Pilon, E.B.C.L. Callagon La Plante, B. Wang, Z. Wei, S. Vallejo Castaño, Facile, low-energy routes for the production of hydrated calcium and magnesium salts from alkaline industrial wastes, US20210024364A1, 2021. https://patents.google.com/patent/US20210024364A1/en (accessed March 28, 2021).

153 A. Sagastume Gutiérrez, J. Van Caneghem, J. B. Cogollos Martínez and C. Vandecasteele, Evaluation of the environmental performance of lime production in Cuba, *Journal of Cleaner Production*, 2012, **31**, 126–136.

154 F. Engström, D. Adolfsson, C. Samuelsson, Å. Sandström and B. Björkman, A study of the solubility of pure slag minerals, *Minerals Engineering*, 2013, **41**, 46–52.

155 WAVE Software for Water Treatment Plant Design, https://www.dupont.com/water/resources/design-software.html, (accessed 16 July 2020).

156 Filmtec BW30-400 High Rejection Brackish Water RO Membrane Element 10500 GPD, https://www.freshwatersystems.com/products/filmtec-bw30-400-high-rejection-brackish-water-ro-membrane-element-10500-gpd, (accessed 9 July 2020).

157 DOW Filmtec BW30-400 RO Membrane 10500 GPD, http://www.filterwater.com/p-741-dow-filmtec-bw30-400-ro-membrane-10500-gpd.aspx, (accessed 9 July 2020).

158 Filmtec BW30-400/34i High Rejection Brackish Water RO Membrane Element With Interlocking End Caps, 10500 GPD, https://www.freshwatersystems.com/products/filmtec-bw30-400-34i-high-rejection-brackish-water-ro-membrane-element-with-interlocking-end-caps-10500-gpd, (accessed 9 July 2020).

159 Historical Inflation Rates, https://www.usinflationcalculator.com/inflation/historical-inflation-rates/, (accessed 8 July 2020).

160 Prices and factors affecting prices - U.S. Energy Information Administration (EIA), https://www.eia.gov/energyexplained/electricity/prices-and-factors-affecting-prices.php, (accessed 9 July 2020).

161 D. Austin, Pricing Freight Transport to Account for External Costs, Congressional Budget Office, 2015.

162 FILMTEC™ Reverse Osmosis Membranes - Technical Manual

163 *openLCA*, GreenDelta, 2006.

164 T. J. Skone, National Energy Technology Laboratory. Carbon Dioxide Utilization – NETL CO2U LCA Guidance Toolkit, https://www.netl.doe.gov/energy-analysis/details, (accessed 29 August 2021).

165 National Renewable Energy Laboratory, U.S. Life Cycle Inventory Database, https://www.nrel.gov/lci/, (accessed 29 August 2021).

166 D. Bonenfant, L. Kharoune, S. Sauve´, R. Hausler, P. Niquette, M. Mimeault and M. Kharoune, CO $_2$ Sequestration Potential of Steel Slags at Ambient Pressure and Temperature, *Ind. Eng. Chem. Res.*, 2008, **47**, 7610–7616.

167 NATCARB CO2 Sources v1501 (Archived) - EDX, https://edx.netl.doe.gov/dataset/natcarb-co2sources-v1501-archived, (accessed 17 June 2021).

168 National Slag Association - Slag availability, http://nationalslag.org/?s=&category=&location=&a=true&count=20&orderby=title&order=ASC, (accessed 30 August 2021).

169 Code of federal regulations (Annual edition). Title 47: Telecommunication.

170 A. Kirchofer, A. Becker, A. Brandt and J. Wilcox, CO $_2$ Mitigation Potential of Mineral Carbonation with Industrial Alkalinity Sources in the United States, *Environ. Sci. Technol.*, 2013, **47**, 7548–7554.

171 *Mineral Commodity Summaries*, U.S. Geological Survey (USGS), 2021.

172 C. Rodriguez-Navarro, A. Burgos-Cara, F. D. Lorenzo, E. Ruiz-Agudo and K. Elert, Nonclassical Crystallization of Calcium Hydroxide via Amorphous Precursors and the Role of Additives, *Crystal Growth & Design*, 2020, **20**, 4418–4432.

173 L. D. Ellis, A. F. Badel, M. L. Chiang, R. J.-Y. Park and Y.-M. Chiang, Toward electrochemical synthesis of cement—An electrolyzer-based process for decarbonating $CaCO_3$ while producing useful gas streams, *Proc Natl Acad Sci USA*, 2020, **117**, 12584–12591.

174 L. Lu, Y. Fang, Z. Huang, Y. Huang and Z. J. Ren, Self-sustaining carbon capture and mineralization via electrolytic carbonation of coal fly ash, *Chemical Engineering Journal*, 2016, **306**, 330–335.

175 J. Johnston, The change of the equivalent conductance of ions with the temperature, *Journal of the American Chemical Society*, 1909, **31**, 1010–1020.

176 D. R. Lide, *CRC Handbook of Chemistry and Physics, 85th Edition*, CRC Press, 2004.

177 T. Al-Shemmeri, *Engineering Fluid Mechanics*, Al-Shemmeri & Ventus Publishing, 2012, 140.